Cooperative optics of low-dimensional clouds of dipolar atoms

Gabriel Bean, MPhys (Hons)

Department of Physics

Lancaster University

A thesis submitted for the degree of

Doctor of Philosophy

January, 2024

Declaration

I declare that the work presented in this thesis is, to the best of my knowledge and belief, original and my own work. The material has not been submitted, either in whole or in part, for a degree at this, or any other university. This thesis does not exceed the maximum permitted word length of 80,000 words including appendices and footnotes, but excluding the bibliography.

Abstract

The emergence and control of collective optics are studied for dense quasi-1D and 2D collections of dipolar atoms. The collective optical response is studied in the regimes of weak and strong magnetic dipole-dipole interactions both at low and high optical density. The introduction of magnetic dipole-dipole interaction changes the availability of collective eigenmodes in the system and how easily they can be occupied. In general, with greater magnetic interactions, there is a reduction in the number of highly super- and subradiant modes with large collective resonances. However, modes that are either uncommon or absent in non-interacting systems can also become available. The introduction of magnetic interactions also makes the occupation of collective modes more selective in terms of beam detuning. This feature allows an enhanced selective excitation of sub-radiant modes in particular compared to a non-interacting system. We study the optical response of these interacting systems and see an increase in resonant scattering at low density. At high density, multiple collective eigenmodes resolve themselves, which is seen as multiple resonant peaks in the scattered intensity. In principle, because the atoms are magnetic dipoles, each atom in the sample should experience a local zeeman shift due to the magnetic fields of its neighbours. We study how this alters the optical response and find this local shift broadens the lineshape. Finally, we study how the introduction of strong magnetic interactions causes the collections of atoms to crystallise spontaneously, both in the 1D and 2D cases. Once crystallised, the atoms' regular spacing dramatically alters the available collective eigenmodes. In weakly interacting systems, the distribution of available eigenmodes in terms of collective resonance and linewidth is largely continuous. In contrast, when crystallised, the distribution localises into a collection of small 'islands'. These modes can be resolved spectrally, allowing for further selective excitation of particular eigenmodes with beam detuning. These modes can also be selected using different beam polarisations and orientations. We can target modes where atoms in the sample are primarily polarised in or out of the plane in the 2D case, or polarised along or normal to the atom chain in the 1D case.

Acknowledgements

This work would have been impossible without the support of many people. Firstly, I am very grateful to my supervisors, Janne Ruostekoski and Neil Drummond, for their guidance, support, enormous knowledge and advice, and endless patience. Thanks to colleagues from the condensed matter theory group in the Physics Department of Lancaster University, especially Bogdan Galilo, Ryan Hunt, Marcin Szyniszewski, David Thomas and Lewis Williamson, for their support and encouragement while I was finding my feet and to Kyle Ballentine and Chris Parmee throughout the end of my time in the department. I also wish to thank Patrick Windpassinger for their early and partial financial support and also discussion with Marvin Proske and Ishan Varma. The Engineering and Physical Sciences Research Council (Grant No. EP/S002952/1) has financially supported this work. Computational facilities have been provided by the Lancaster High-End Computing Cluster (HEC). I would also like to thank Jonathan Gratus, Aneta Stefanovska and Brian Strong, without whom I would not have started this journey. I am grateful to my family, especially Caroline and Danny Strong, for their endless support. Finally, I thank Ellie Riley. This would not have been possible without her and her kindness, support, and love over these years.

Contents

List of Figures

1 Introduction

1.1 Motivation and Background

We often describe the optics of condensed matter systems in bulk using a mean-field approach. Each emitter in the material is assumed to respond to the average influence of the neighbouring emitters in the system [1, 2]. This approach makes simulating many-body systems considerably easier by reducing the number of degrees of freedom being considered [3]. This model is suitable when the emitters are uncorrelated, as seen in systems with weak coupling or strong driving [3], but can fail when correlations become significant. Specifically, mean-field theories can model low-density optical systems well but fail dramatically at high density [4–7] when the separation between emitters is comparable to the wavelength of the interacting light [2]. At high density, the action of recurrent scattering between emitters in the ensemble allows for correlations between the polarisations of the emitters to emerge [8]. Such an optical response is known as collective or cooperative since the atoms are no longer uncorrelated and respond as a group.

Systems exhibiting collective optics not only fail to be modelled by mean-field theories but give rise to interesting phenomena, in particular super- and subradiance [9–11]. When a group of emitters exhibits super-radiance, the system (in response to an incident light field) emits a pulse of light with greater intensity and shorter decay time than would be expected from the single linewidth of the individual emitters [12], as mean-field theory would predict. Sub-radiance then, as the name suggests, is when the excitation of the emitters decays much more slowly than would normally be expected, due to collective response, resulting in the light being re-emitted much more slowly. These two effects are due to the constructive or destructive interference between the emitters in the system, respectively. This coherent response requires the spacing between emitters to be comparable to or smaller than the incident field wavelength. These collective effects have numerous applications, including storage of light [13–17] and enhanced directional emission [18] among others. It is important to note that these collective effects can be washed out by thermal effects [8, 19].

The work aims to investigate how the introduction of static magnetic dipole-dipole interactions between the atoms can modify the collective optical response of cold clouds of atoms. Since

recurrent scattering between atoms causes cooperative behaviour to emerge, the cooperative behaviour of such systems depends sensitively on the arrangement of atoms within the ensemble. The addition of long-range magnetic dipole-dipole interactions modifies the distribution of particles and, as such, potentially modifies the optical response as well. Some recent work has also investigated similar dipolar systems [20, 21].

Recent advancements have achieved the realisation of these kinds of dipolar systems including Cr, [22, 23], Dy [24, 25] and Er [26–28]. Throughout, we will be considering Dysprosium as a model atom because of its sizeable magnetic moment $\mu = 10\mu_b$ [24, 29, 30], and rich level structure [31]; however other species could be used that still have long-range dipole-dipole interactions, for example Chromium, alkali metals such as Rubidium, Rydberg atoms or polar molecules [5, 22, 30, 32–36].

These dipolar systems are observed to spontaneously crystallise or form droplets and supersolids with a regular arrangement [37–47]. The hope is that these kinds of systems will exhibit collective behaviour similar to what is observed in dense arrays of atoms. These regular dipolar systems may display similar collective responses without using an optical lattice to produce the regularity. Using an optical lattice to form the array naturally adds thermal energy to the atoms, whereas this is not the case in a dipolar crystal.

1.2 Outline

In this work, I will investigate the effect of magnetic dipole-dipole interactions between atoms on the optical response and collective eigenmodes in cold clouds of atoms. These atoms are assumed to be held in either a pancake or cigar-shaped trap to achieve a quasi-2D or 1D system, respectively. Such systems are achieved physically using a magneto-optical-trap (MOT) [30, 48–50]. Each atom is also assumed to have identical internal magnetic dipole moments $\boldsymbol{\mu}$ that are aligned in the same direction by an external field. The dipoles are oriented perpendicular to the plane of the trap in the quasi-2D case and perpendicular to the long axis of the trap in the quasi-1D case. These atoms are then subjected to an incident monochromatic Gaussian beam focused on the collection of atoms. The repulsive interaction between the atoms modifies the correlations between them, leading to changes in the collective optical response of the system.

This work studies the optical response at various densities sufficiently high to probe the effects of magnetic interactions on cooperative optics.

The role of magnetic interactions is examined in two regimes: The strongly and weakly interacting regimes. The strongly interacting regime is defined as when magnetic interactions are large enough that crystallisation occurs, and the weakly interacting case is otherwise. We begin by studying the weak interaction regime and the changes in the light scattering from the samples due to these magnetic interactions. The change in optical response is analysed in terms of the overall electric polarisation of the system, as well as the distribution of atom separations and the effect this has on the availability and occupation of collective eigenmodes. We find that the introduction of magnetic dipole interactions, especially at high density, modifies the occupied collective modes in favour of collective modes not easily excited in analogous non-interacting cases. These modes are often super- or subradiant (having linewidths larger or smaller than the single-atom linewidth, respectively) with resonant frequencies far from the single-atom resonance. As density increases, the availability of highly super- and subradiant modes increases. These super- and subradiant modes also tend to have large collective resonances. Introducing magnetic interactions makes the excitation of some of these modes easier, which can, at times, increase the scattering from the sample or broaden the range of frequencies the sample responds to.

We also study the effect of inhomogeneous Zeeman splitting on the optical response of the system. The presence of nearby dipolar atoms in the sample will cause Zeeman shifting of other nearby atoms. This inhomogeneous Zeeman splitting is found to shift the peak resonant frequency and broaden the line shape. Finally, we study the crystallised regime. In the crystallised regime, a range of interesting eigenmodes are made available at high density. We explore what kind of collective eigenmodes become available and how some can be excited by the incident field. We find that a range of super- and subradiant modes can be excited when the collection has crystallised. However, the excitation of these modes is sensitively dependent on the beam orientation, polarisation and frequency.

2 Theory

2.1 Optical Response Theory

This section presents equations for the optical response of a collection of atoms. Firstly, we discuss the atomic polarisation dynamics, followed by coherent and incoherent transmission and reflection, and finally collective eigenmodes. Throughout, phasor notation is used, where positive frequency components are denoted with a '+' superscript.

2.1.1 Incident field and level structure

We assume a low-intensity incident light field $\boldsymbol{\mathcal{E}}_0^+(\mathbf{r},t)$ with frequency ω drives the optical response of the system. All oscillating parameters of interest (e.g., dipole moments) can be written as slowly varying amplitudes once the driving field frequency is factored out, i.e.,

$$\boldsymbol{\mathcal{E}}_0^+ \to e^{-i\omega t}\boldsymbol{\mathcal{E}}_0^+. \tag{1}$$

The incident field frequency ω is assumed to be near the optical transition frequencies of the atoms; specifically, the $J=0\to J=1, m=\pm1,0$ transitions where J is the total angular momentum quantum number and m is the magnetic quantum number. The detuning of the beam from the jth atom's transitions (of N total atoms) can be expressed as a matrix in the circular polarisation basis

$$\hat{\mathbf{e}}_\pm = \mp\frac{1}{\sqrt{2}}(\hat{\mathbf{e}}_x \pm i\hat{\mathbf{e}}_y), \qquad \hat{\mathbf{e}}_0 = \hat{\mathbf{e}}_z, \tag{2}$$

as

$$\underline{\Delta}^{(j)} = \begin{pmatrix} \Delta_{+1}^{(j)} & 0 & 0 \\ 0 & \Delta_{-1}^{(j)} & 0 \\ 0 & 0 & \Delta_0^{(j)}. \end{pmatrix} \tag{3}$$

This basis is a natural choice since circularly polarised light, $\hat{\mathbf{e}}_{\pm,0}$, drives the $J=0\to J=1, m=\pm1,0$ transition, while linearly polarised light generally drives some combination of different transitions. $\underline{\Delta}^{(j)}$ contains the detuning of the incident beam from each transition of the j'th atom, $\Delta_m^{(j)} = \omega - \omega_m^{(j)}$, where the frequency $\omega_m^{(j)}$ is the $J=0\to J=\pm1, m$ sub-level transition frequency. We include the atom index j to incorporate

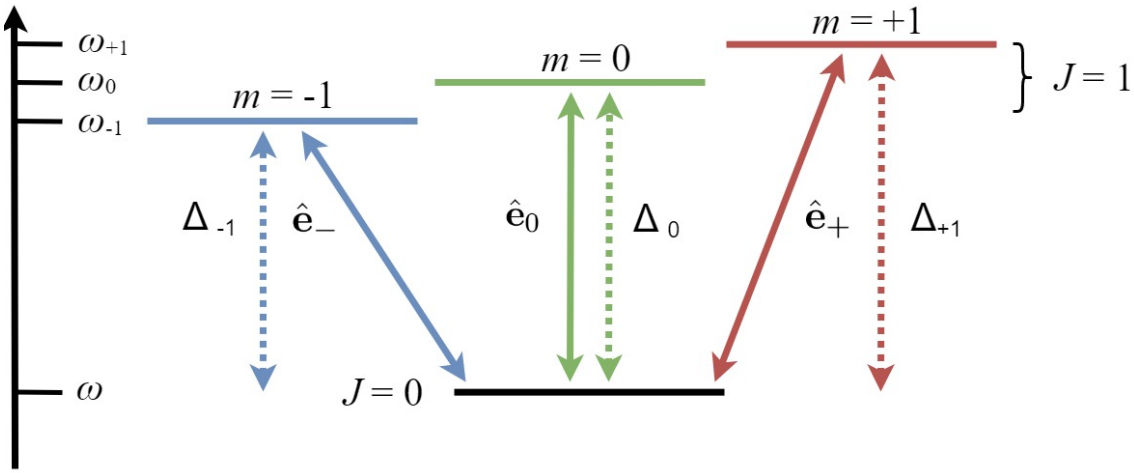

Figure 1: Schematic of the $J = 0 \rightarrow J = 1, m = \pm 1, 0$ transitions of the 4-level atoms with labelled resonant frequencies, resonant beam detunings and driving polarisations for each transition.

inhomogeneous broadening later; it may be dropped when only homogeneous broadening is present. If the system has only homogeneous broadening, then $\Delta_m^{(j)} = \Delta_m, \forall j$. If there is no shift between the $J = 1$ sub-levels and all the atoms have identical transitions, then the detuning of the beam can be denoted simply as Δ.

2.1.2 Classical dipole approximation

It can be assumed that atoms behave like classical linear dipole emitters in the low-light intensity limit, as the excited state population can be neglected [5]. Therefore the scattered field at point $\mathbf{r}$ from the lth atom in the sample, $\mathbf{E}_{\mathrm{S}}^{(l)+}$ can be written as

$$\mathbf{E}_{\mathrm{S}}^{(l)+}(\mathbf{r}) = \frac{1}{\epsilon_0}\mathsf{G}(\mathbf{r} - \mathbf{X}_l)\mathbf{d}_l^+, \tag{4}$$

where $\mathbf{X}_l$ is the position of the lth atom and $\mathsf{G}(\mathbf{r})$ is the monochromatic dipole radiation kernel [1, 51], which gives the radiated field at point $\mathbf{r}$ due to an oscillating dipole at the origin with vector dipole moment $\mathbf{d}$:

$$\mathsf{G}(\mathbf{r})\,\mathbf{d} = \frac{k^3}{4\pi}\left\{(\hat{\mathbf{n}}\times\mathbf{d})\times\hat{\mathbf{n}}\frac{e^{ikr}}{kr} + [3\hat{\mathbf{n}}(\hat{\mathbf{n}}\cdot\mathbf{d}) - \mathbf{d}]\left[\frac{1}{(kr)^3} - \frac{i}{(kr)^2}\right]e^{ikr}\right\} - \frac{\mathbf{d}\delta(\mathbf{r})}{3}, \tag{5}$$

where $\mathbf{k} = k\hat{\mathbf{n}}$ is the wavevector of the radiated field. The first term within the brackets dominates when r is large, giving the long-range scattered field. The second term within the bracket gives the scattered field at short range and is important to include as we consider how scattered fields from atoms within the sample influence each other. The final term, the

contact term, is included so that the radiated field satisfies Maxwell's equations [52]. The dipole moment will be replaced by the polarisation amplitude $\boldsymbol{\mathcal{P}}$ defined as

$$\mathbf{d}_j^+(t) = \mathcal{D}\boldsymbol{\mathcal{P}}^{(j)}(t), \tag{6}$$

where $\mathcal{D}$ is the reduced dipole matrix element [53] for the $J = 0 \to J = 1$ transition. This substitution matches the notation with the literature [51]. All polarisation amplitudes, $\boldsymbol{\mathcal{P}}$, throughout, refer to positive frequency components.

2.1.3 Polarisation dynamics

The total external field at the position of the jth atom is given by the incident field plus the scattered fields from all the other atoms

$$\mathbf{E}_{\text{ext}}^+(\mathbf{r}_j) = \boldsymbol{\mathcal{E}}_0^+(\mathbf{r}_j) + \sum_{l\neq j} \mathbf{E}_S^{(l)+}(\mathbf{r}_j). \tag{7}$$

Thus, the dipole moment of each atom depends on the fields from all other atoms in the system, leading to a set of N coupled equations that must be solved simultaneously to determine the polarisation of each atom. In principle, a hierarchy of coupled equations has to be solved, where n-atom correlations depend on $n+1$-atom correlations, and so on, up to N-atom correlations. However, because of the low light intensity and simple atom-level structure , these higher-order correlations can be neglected [54]. The dynamics of the polarisation amplitudes for each atom can be described by the N coupled equations

$$\frac{d}{dt}\boldsymbol{\mathcal{P}}^{(j)} = (i\underline{\Delta}^{(j)} - \gamma)\boldsymbol{\mathcal{P}}^{(j)} + i\frac{\xi\epsilon_0}{\mathcal{D}}\,\mathbf{E}_{\text{ext}}^+(\mathbf{r}_j) \tag{8}$$

shown in [5], where γ is the single atom natural linewidth

$$\gamma = \frac{\mathcal{D}^2 k^3}{6\pi\hbar\epsilon_0}, \tag{9}$$

and

$$\xi = \frac{6\pi\gamma}{k^3} = \frac{\mathcal{D}^2}{\hbar\epsilon_o}. \tag{10}$$

k is the wavenumber of the incident field, $k = 2\pi/\lambda$. Using Eqs. (4), (6), and (7), we can rewrite the external field in terms of the radiation kernel. Additionally, we can rewrite the equations of motion in terms of individual vector components, resulting in $3N$ simultaneous equations

$$\frac{d}{dt}\mathcal{P}_m^{(j)} = (i\Delta_m^{(j)} - \gamma)\mathcal{P}_m^{(j)} + i\frac{\xi\epsilon_0}{\mathcal{D}}\hat{\mathbf{e}}_m^* \cdot \boldsymbol{\mathcal{E}}_0^+(\mathbf{r}_j) + i\xi\sum_{l\neq j}\sum_n \mathsf{G}_{mn}^{(jl)}\mathcal{P}_n^{(l)}\,, \tag{11}$$

where the subscript $m = \pm 1, 0$ signifies the m'th vector component, and $\hat{\mathbf{e}}_m$ is the m'th circular polarisation unit vector. This choice ensures that the detuning values Δ_m correspond to the polarisation amplitudes $\mathcal{P}_m$, as they should. We have additionally defined the coupling between two atoms j and l as

$$\mathsf{G}_{mn}^{(jl)} = \hat{\mathbf{e}}_m \cdot \mathsf{G}(\mathbf{r}_j - \mathbf{r}_l)\hat{\mathbf{e}}_n, \tag{12}$$

where G is written as a matrix. To determine the steady-state response of the system, we impose that the polarisation amplitudes are also in a steady state, given by

$$\frac{d\mathcal{P}_m^{(l)}}{dt} = 0, \ \forall\, l, m \tag{13}$$

While it is possible to examine the time-dependent behaviour of the system, this work will focus exclusively on the steady-state solution. Finally, the total field outside the sample at some point $\mathbf{r}$ can now be calculated from the sum of the incident light field and scattered fields of each atom

$$\mathbf{E}^{+}(\mathbf{r}) = \boldsymbol{\mathcal{E}}_0^{+}(\mathbf{r}) + \sum_l \mathbf{E}_S^{(l)+}(\mathbf{r}). \tag{14}$$

2.1.4 Matrix equation formulation

The dynamics of the atomic polarisations can be represented in matrix form using the notation adopted in previous works [55, 56]. First, we define $\mathbf{b}$ as the $3N$-dimensional vector that contains all the atomic polarisations $\mathcal{P}_m^{(j)+}$ arranged as

$$b_\alpha = \mathcal{P}_m^{(j)+}: \qquad \alpha = 3j - 1 + m, \tag{15}$$

where m can take values $m = -1, 0, 1$, and $j = 1, 2, 3, ..., N$ is the index of the atom. The elements of the vector $\mathbf{F}$ are related to the driving field by

$$F_\alpha = i\frac{\xi\epsilon_0}{\mathcal{D}}\hat{\mathbf{e}}_m^* \cdot \hat{\boldsymbol{\mathcal{E}}}_0^{+}(\mathbf{r}_j), \tag{16}$$

and are similarly arranged. The off-diagonal elements of the matrix $\mathcal{H}$ are

$$\mathcal{H}_{\alpha\beta} = \xi G_{mn}^{(jl)}, \quad j \neq l, \tag{17}$$

where β is defined similarly to α in terms of l and n and the diagonal elements are $i\gamma$. Matrix $\delta\mathcal{H}$ is diagonal and contains the beam detunings $\Delta_m^{(j)}$. With these definitions, we can write Eq. (8) as a matrix equation as [57]

$$\dot{\mathbf{b}} = i(\mathcal{H} + \delta\mathcal{H})\mathbf{b} + \mathbf{F}. \tag{18}$$

The steady-state solution can also be found by solving the matrix equation

$$-i(\mathcal{H}+\delta\mathcal{H})\mathbf{b}=\mathbf{F}. \tag{19}$$

2.1.5 Collective eigenmodes

The system can be analysed through the eigenvectors and eigenvalues of the 'interaction matrix' $\mathcal{H}$ as in [13]. The eigenvectors $\mathbf{v}_p$ ($\mathcal{H}\mathbf{v}_p = h_p\mathbf{v}_p$,$\mathbf{w}_p^\dagger\mathcal{H} = \mathbf{w}_p^\dagger h_p$) contain a set of polarisations $\boldsymbol{\mathcal{P}}_p^{(j)}$ for all the atoms in the sample for a given set of atomic positions. Each eigenvector $\mathbf{v}_p$ will be referred to as a collective eigenmode since it describes the polarisation of the entire collection. The eigenvectors $\mathbf{v}_n$ are not necessarily orthogonal ($\mathbf{v}_p^\dagger\mathbf{v}_q \neq \delta_{pq}$) because $\mathcal{H}$ is not hermitian, however they are biorthogonal $\mathbf{w}_p^\dagger\mathbf{v}_q = \delta_{pq}$ and do form a basis [13, 51, 57] because the interaction matrix $\mathcal{H}$ is symmetric where $\delta\mathcal{H}$ is assumed to contain any terms that would break symmetry, such as level shifts. Therefore, any particular polarisation of the system $\mathbf{b}$ can be written in terms of the eigenvectors $\mathbf{v}_p$ as

$$\mathbf{b}(t)=\sum_p c_p(t)\mathbf{v}_p, \qquad \mathbf{F}=\sum_p f_p\mathbf{v}_p, \tag{20}$$

where the incident field is also expressible in this basis. The interaction matrix has corresponding eigenvalues h_n. These eigenvalues are complex, in general, because $\mathcal{H}$ is, in general, non-hermitian. Therefore, the eigenvalues can be written in terms of real and imaginary components

$$h_p=\delta_p+iv_p, \tag{21}$$

where δ_p is the collective resonance shift and v_p is the collective linewidth.

When studying the system's steady-state solution, it is useful to describe the polarisation in terms of components of the eigenvectors. Since the eigenvectors $\mathbf{v}_p$ are not necessarily orthogonal, the occupation of each mode is not simply the coefficient c_p. The symmetry of $\mathcal{H}$ means that the biorthoginality condition can be simplified to $\mathbf{v}_p^\dagger\mathbf{v}_p = 0$, since $\mathbf{w}_p^\dagger = \mathbf{v}_q^T$ and therefore the occupation of a mode is measured by [13, 57]

$$L_p=\frac{|\mathbf{v}_p^T\mathbf{b}|^2}{\sum_q|\mathbf{v}_q^T\mathbf{b}|^2}. \tag{22}$$

The indexes p, q signify enumerated eigenmodes of the system, which may be ordered, for example, by the linewidth or resonance shift values. In the next section, we will discuss how

to calculate the expectation values of the system by stochastically sampling atomic positions. This set of atomic positions (or system realisations) is then the ensemble. The eigenmodes labelled by p, q can refer to eigenmodes of a single realisation of the ensemble but generally refer to the set of eigenmodes for all of the realisations of the entire ensemble.

3 Stochastic simulations

3.1 Stochastic electrodynamics

In the previous section, we saw how to solve the polarisation dynamics of a collection of dipoles at fixed positions. However, the system we are interested in inherently includes quantum fluctuations of atomic positions. These fluctuations can be accounted for by employing stochastic methods [20, 57, 58]. The systems considered here are assumed to be cold, so only quantum fluctuations will be considered. However, similar stochastic methods can be used in the thermal case as well [19].

To solve the polarisation dynamics, including position fluctuations, the atomic positions can be treated as stochastic variables [6, 54, 57], when the low light intensity limit is assumed. Single realisations of the system (a set of fixed atom positions $\mathbf{R}_\sigma$) are sampled from the probability distribution $P(\mathbf{r}_1, \mathbf{r}_2, \ldots, \mathbf{r}_N)$ that correctly describes the system of particles in the absence of light. Then, for each realisation σ, the polarisation dynamics are solved for the fixed atom positions $\mathbf{R}_\sigma$, according to Eq. (11). As well as the polarisation, other observables O for the realisation σ can be calculated, such as the total electric field outside the sample Eq. (14). The expected value of the observable O can be calculated as the ensemble average $\langle O \rangle$ over the set of sampled realisations $\{\sigma\}$.

To accurately sample the atom positions, we can calculate the appropriate probability distribution $P(\mathbf{r}_1, \mathbf{r}_2, \ldots, \mathbf{r}_N)$ for the system that correctly encodes the correlations between the atoms before the light is introduced. In the independent atom case, we can assume the atom positions are uncorrelated initially [2, 6, 8, 59]. $P(\mathbf{r}_1, \mathbf{r}_2, \ldots, \mathbf{r}_N)$ then often takes a simple form. In the cases studied here, the Gaussian distribution resulting from the trapping potential can be used Eq. (46), for example.

However, we cannot take such an approach in the interacting case, such as for magnetic dipolar atoms studied here. Instead, we can sample the atom positions according to the square modules of the ground state wavefunction $P(\mathbf{r}_1, \mathbf{r}_2, \ldots, \mathbf{r}_N) = |\Psi(\mathbf{r}_1, \mathbf{r}_2, \ldots, \mathbf{r}_N)|^2$ [60]. Other methods for calculating the relevant wavefunction could be used [61]; however, in this work, the ground state wavefunction is calculated by Quantum Monte-Carlo methods as discussed in Sec. 3.2.3. In this work we will be considering bosons however systems obeying fermion statistics can also be treated similarly [62].

It can be shown that this stochastic classical-electrodynamics approach converges to an exact solution for stationary atoms at arbitrary densities assuming a single electronic ground state [54] and can also be used to incorporate multiple non-degenerate excited states [13, 52].

3.1.1 Expectation values and transmission

In the previous section, we discussed calculating the expectation value of a general observable O of a system of N dipoles through stochastic classical-electrodynamics methods. Here, we discuss various useful observables and how they are calculated.

Firstly, the expected intensity of various fields can be expressed in terms of ensemble averages of the electric fields as [57]

$$I = 2cn\epsilon_0 \left\langle \mathbf{E}^- \cdot \mathbf{E}^+ \right\rangle , \tag{23}$$

where n is the refractive index. It should be noted that this formula for the field intensity differs from the standard convention [1] due to the use of phasor notation.

The transmission and reflection through the sample can then be calculated from these intensity expectation values. Since the exact proportionality is not of importance, we refer to the expectation values of the form $\langle \mathbf{E}^- \cdot \mathbf{E}^+ \rangle$ as 'intensities', even though strictly speaking, they are not. The transmission and reflection are defined as

$$T = \frac{\int\int \langle (\boldsymbol{\mathcal{E}}_0^- + \mathbf{E}_\mathrm{S}^-) \cdot (\boldsymbol{\mathcal{E}}_0^+ + \mathbf{E}_\mathrm{S}^+) \rangle \, dA}{\int\int \langle \boldsymbol{\mathcal{E}}_0^- \cdot \boldsymbol{\mathcal{E}}_0^+ \rangle \, dA} \tag{24}$$

and

$$R = \frac{\int\int \langle \mathbf{E}_{\mathrm{S}}^{-} \cdot \mathbf{E}_{\mathrm{S}}^{+} \rangle \, dA'}{\int\int \langle \boldsymbol{\mathcal{E}}_{0}^{-} \cdot \boldsymbol{\mathcal{E}}_{0}^{+} \rangle \, dA'} \tag{25}$$

where A and A' are the areas of the lenses that collect the light from the sample. A is a lens centred on the optical axis in front of the sample, ahead of the incident beam, while A' is a lens on the optical axis behind the sample. The collecting lenses areas A, and A' are defined by the lens numerical aperture

$$NA = n \sin(\theta), \tag{26}$$

where θ is the angle between the optical axis and the lens edge.

The scattered field from a single realisation can be written in terms of the ensemble-averaged scattered field and a contribution due to the fluctuation of the particular realisation from the ensemble average, [57]. Therefore the field scattered from a single realisation is [7]

$$\mathbf{E}_{\mathrm{S}}^{+} = \langle \mathbf{E}_{\mathrm{S}}^{+} \rangle + \delta \mathbf{E}_{\mathrm{S}}^{+}, \qquad \mathbf{E}_{\mathrm{S}}^{+} = \sum_{l} \mathbf{E}_{\mathrm{S}}^{(l)+}, \tag{27}$$

where $\langle \mathbf{E}_{\mathrm{S}}^{+} \rangle$ is the ensemble-averaged scattered field and $\delta \mathbf{E}_{\mathrm{S}}^{+}$ is the contribution due to the fluctuation of the realisation. The total intensity contained in Eq. (24) is then

$$\begin{aligned} \langle (\boldsymbol{\mathcal{E}}_{0}^{-} + \mathbf{E}_{\mathrm{S}}^{-}) \cdot (\boldsymbol{\mathcal{E}}_{0}^{+} + \mathbf{E}_{\mathrm{S}}^{+}) \rangle = \boldsymbol{\mathcal{E}}_{0}^{-} \cdot \boldsymbol{\mathcal{E}}_{0}^{+} + \boldsymbol{\mathcal{E}}_{0}^{-} \cdot \langle \mathbf{E}_{\mathrm{S}}^{+} \rangle + \langle \mathbf{E}_{\mathrm{S}}^{-} \rangle \cdot \boldsymbol{\mathcal{E}}_{0}^{+} \\ + \langle \mathbf{E}_{\mathrm{S}}^{-} \rangle \cdot \langle \mathbf{E}_{\mathrm{S}}^{+} \rangle + \langle \delta \mathbf{E}_{\mathrm{S}}^{-} \cdot \delta \mathbf{E}_{\mathrm{S}}^{+} \rangle \, , \end{aligned} \tag{28}$$

where

$$\langle \mathbf{E}_{\mathrm{S}}^{-} \cdot \mathbf{E}_{\mathrm{S}}^{+} \rangle = \langle \mathbf{E}_{\mathrm{S}}^{-} \rangle \cdot \langle \mathbf{E}_{\mathrm{S}}^{+} \rangle + \langle \delta \mathbf{E}_{\mathrm{S}}^{-} \cdot \delta \mathbf{E}_{\mathrm{S}}^{+} \rangle \, , \tag{29}$$

and

$$\langle \delta \mathbf{E}_{\mathrm{S}}^{-} \cdot \delta \mathbf{E}_{\mathrm{S}}^{+} \rangle = \langle (\mathbf{E}_{\mathrm{S}}^{-} - \langle \mathbf{E}_{\mathrm{S}}^{-} \rangle) \cdot (\mathbf{E}_{\mathrm{S}}^{+} - \langle \mathbf{E}_{\mathrm{S}}^{+} \rangle) \rangle \, . \tag{30}$$

The first term of Eq. (28) is the intensity due to the incident beam. The second, third, and fourth terms are the scattered intensity due to the ensemble average and its interference with the incident beam. This component will be referred to as the coherently scattered intensity. Finally, the fifth term is the component of the scattered intensity due solely to fluctuations of realisations of the ensemble from the ensemble average; this component is referred to as the incoherently scattered intensity [57]. The incoherent intensity is the 'noisy' contribution to the total scattered intensity, due to the contributions from the random fluctuations of positions

and polarisations across different realisations. Naming the intensity incoherent is not implying the incoherently scattered fields have random frequencies as it might suggest. In the case that there are no system fluctuations there is no incoherent scattering. The reflection and transmission can now similarly be defined in terms of coherent and incoherent components. The terms from Eqs. (28) and (29) are substituted into Eqs. (24), and (25) to calculate the coherent transmission or reflection, where the final term in each case, $\langle \delta\mathbf{E}_{\mathrm{S}}^{-} \cdot \delta\mathbf{E}_{\mathrm{S}}^{+} \rangle$ is omitted. Instead, the incoherent transmission and reflection are calculated by only including this final term. The coherent transmission will often be quoted throughout as an optical depth defined as

$$\mathrm{OD}_{\mathrm{coh}} = -\ln\left(T_{\mathrm{coh}}\right) \tag{31}$$

The collection regions A and A' are far from the sample, allowing the far-field approximation of the dipole radiation instead of the full radiation kernel. The field scattered by the lth atom in the far field is given by

$$\mathbf{E}_{\mathrm{S}}^{(l)+}(\mathbf{r}) = \frac{k^2\mathcal{D}}{4\pi\epsilon_0 R_l}\left\{\left(\hat{\mathbf{R}}_l \times \boldsymbol{\mathcal{P}}^{(l)}\right) \times \hat{\mathbf{R}}_l\right\} e^{ikR_l}, \tag{32}$$

where $\mathbf{R}_l = \mathbf{r} - \mathbf{X}_l$.

3.2 Particle Interactions

The positions of the atoms in the sample depend on their interactions with each other and the optical trap. In particular, in the absence of optical interactions, the system can be described by the Hamiltonian

$$\hat{H} = \sum_{j=1}^{N} \left[\frac{-\hbar^2}{2M} \boldsymbol{\nabla}_j^2 + V_{\text{trap}}(\mathbf{X}_j) \right] + \sum_{j=1}^{N} \sum_{l>j}^{N} V_{\text{dd}}(\mathbf{X}_{lj}) + V_{\text{LJ}}(\mathbf{X}_{lj}). \tag{33}$$

where

$$V_{\text{trap}}(\mathbf{X}_j) = \frac{1}{2} M \sum_{d=1}^{3} \left(\omega_d x_d^{(j)} \right)^2, \tag{34}$$

and where d denotes the three Cartesian coordinates, j is the atom index, ω_d is the frequency of the harmonic trap in the dth dimension, and M is the mass of the species of atom in the system. V_{dd} gives the dipole potential between atom pairs, while V_{LJ} is the Lennard-Jones potential between pairs of atoms.

3.2.1 Dipole potential

The interaction potential between two arbitrary magnetic dipoles μ_j, μ_l is given by [1, 29]

$$V_{\text{dd}}(\mathbf{X}_{lj}) = -\frac{\mu_0}{4\pi |\mathbf{X}_{lj}|^3} [3(\boldsymbol{\mu}_l \cdot \hat{\mathbf{X}}_{lj})(\boldsymbol{\mu}_j \cdot \hat{\mathbf{X}}_{lj}) - \boldsymbol{\mu}_l \cdot \boldsymbol{\mu}_j] - \frac{2}{3} \mu_0 \boldsymbol{\mu}_l \cdot \boldsymbol{\mu}_j \delta(\mathbf{X}_{lj}), \tag{35}$$

where $\mathbf{X}_{lj} = \mathbf{X}_j - \mathbf{X}_l$ is the vector going from the lth to jth atom, and $\boldsymbol{\mu}_l$ is the dipole moment of the lth atom. Atoms in the pancake-shaped trap are assumed to have internal magnetic dipoles aligned perpendicular to the trap plane. Therefore, we can simplify the expression to

$$V_{\text{dd}}(\mathbf{X}_{lj}) = -\frac{\mu_0 \mu^2}{4\pi |\mathbf{X}_{lj}|^3} [3(\hat{\boldsymbol{\mu}} \cdot \hat{\mathbf{X}}_{lj})^2 - 1] - \frac{2}{3} \mu_0 |\boldsymbol{\mu}|^2 \delta(\mathbf{X}_{lj}). \tag{36}$$

The interaction length can characterise the dipole-dipole interaction strength

$$R_{\text{dip}} = \frac{M \mu_0 \mu^2}{4\pi \hbar^2} \tag{37}$$

For clarity, in the literature, a different definition [45] of the dipole-dipole interaction length scale $a_{dd} = R_{\text{dip}}/3$ is used, although this work will not use this definition. In this system, when the dipole-dipole potential is predominately repulsive, the potential can be approximated as

$$V_{\text{dd}}(\mathbf{X}_{lj}) = \max \left\{ 0, \frac{-\mu_0 \mu^2}{4\pi |\mathbf{X}_{lj}|^3} \left[3(\hat{\boldsymbol{\mu}} \cdot \hat{\mathbf{X}}_{lj})^2 - 1 \right] \right\} \tag{38}$$

To use the above approximation, the confining trap needs to prevent the atoms from moving above or below each other into the attractive region of the potential. When this is not the case, we can employ the Lennard-Jones potential.

3.2.2 Lennard-Jones Potential

The Lennard-Jones potential can model the interactions between the atoms that would be present without the magnetic interactions [45]. The c_6 term models the Van der Walls interaction, and the c_{12} interaction models a hard wall potential that prevents atoms from overlapping.

$$V_{\mathrm{LJ}}(\mathbf{X}_{lj}) = -\frac{c_6}{|\mathbf{X}_{lj}|^6} + \frac{c_{12}}{|\mathbf{X}_{lj}|^{12}} \tag{39}$$

When including the Lennard-Jones potential, the values for c_6 and c_{12} match the known values for Dysprosium [29, 45]. The Lennard-Jones potential allows for the attractive region of the dipole-dipole interaction to be included because of the repulsive contribution of the LJ potential at short range.

3.2.3 Quantum Monte-Carlo

At zero temperature, the atom positions are distributed according to the square modulus of the ground state wavefunction ψ. For some systems, simpler or known distributions can be used. For example, the positions of cold, non-interacting atoms in an optical trap are described by a Gaussian distribution. This distribution is known analytically and has the advantage of allowing the separation of variables. In the interacting case studied here, such simple distributions cannot be used since they don't capture the correlations between atom positions. The most direct way to find a suitable distribution is to calculate the ground-state wavefunction of the system $|\psi(\mathbf{R})|^2$ as it necessarily captures the position correlations in the probability distribution, where $\mathbf{R}$ is the position vector of the N particles in D dimensional space. Calculating the many-body wavefunction of a D dimensional, N particle system requires calculating high dimensional $(D \times N)$ integrals. Standard integration methods become very inefficient in such cases if the system is also not separable, as is the case here. For example, the composite trapezoidal and Simpsons' rule integration methods converge as $O\left(n^{-2/D}\right)$ [63] and $O\left(n^{-4/D}\right)$ [64], respectively. Quantum Monte Carlo methods are employed in this work

because they are particularly suited to such problems. Monte-Carlo integration uses random sampling of the integration region to estimate the integral and, as such, converges at a rate in-dependent on dimensionality. Instead, a Monte Carlo integration that randomly samples the integration region using n points converges as $O\left(n^{-1/2}\right)$ [63, 64].

The system's ground state is determined through two successive calculations: a variational Monte Carlo (VMC) calculation followed by a diffusion Monte Carlo (DMC) calculation. The VMC method is a variational approach that provides a trial wavefunction ψ_{vmc}, that gives an upper bound on the ground state energy. This trial wavefunction is a guiding wavefunction in the DMC calculation, which determines the ground state. The DMC approach finds the ground state by evolving many-body configurations through imaginary time by simulating processes governed by the equation

$$-\frac{\partial f(\tau,\mathbf{R})}{\partial \tau} = -\frac{1}{2}\nabla^2 f(\tau,\mathbf{R}) - \nabla\cdot[\mathbf{F}(\tau,\mathbf{R})f(\tau,\mathbf{R})] + [E_l(\mathbf{R}) - E_R]f(\tau,\mathbf{R}), \tag{40}$$

where

$$f(\tau,\mathbf{R}) = \psi_{\text{vmc}}(\mathbf{R})\psi(\tau,\mathbf{R}), \quad \mathbf{F}(\mathbf{R}) = \frac{\nabla\psi_{\text{vmc}}(\mathbf{R})}{\psi(\mathbf{R})}, \tag{41}$$

$$E_l(\mathbf{r}) = \frac{\hat{H}\psi_{\text{vmc}}(\mathbf{r})}{\psi_{\text{vmc}}(\mathbf{r})}, \tag{42}$$

The diffusion equation is found from the imaginary time Schrödinger equation and describes the evolution of configurations towards the ground state over imaginary time [63, 64]. The terms in the equation from left to right describe the diffusion, the drift and population change of configurations (source/sink). $E_l(\mathbf{r})$ is called the local energy, while E_R is a reference energy used to control the population of configurations. In theory, this DMC calculation is exact for our system, given enough simulation time. The DMC calculation also naturally provides a collection of position configurations $\{\mathbf{X}_j\}$ that follow the distribution $\psi^*\psi_{\text{vmc}}$, making it ideal for stochastic sampling. Expectation values are then estimated via an ensemble average over the set of configurations. However, one should not use the entire set of configurations sampled in the DMC calculation. Sequential configurations are likely close to each other in configuration space since they are arrived at through a small imaginary time step. Therefore, a subset of the complete configuration set should be used to remove any serial correlation. Separating the configurations by large timesteps in imaginary time achieves this.

3.2.4 CASINO

The QMC calculations are performed with the CASINO software, [65]. In each case, a VMC calculation is performed first. In these calculations, the trial wavefunction form was

$$\Psi(\mathbf{r}_1, \ldots, \mathbf{r}_N) = e^{J(\mathbf{r}_1,\ldots,\mathbf{r}_N)} \prod_{i=1}^{N} \phi_i(\mathbf{r}_i), \tag{43}$$

where the $\phi(\mathbf{r}_i)$ are Gaussian functions, and the Jastrow term contains polynomial two and three body terms [66]. In the case of weak interactions, a single Gaussian orbital is used and chosen to be fixed at the centre of the trap where only the widths in each Cartesian dimension are optimisable parameters. When the confining trap is symmetric, a similar symmetry is imposed on the orbital width to improve computation speed. When stronger interactions are included, meaning the system passes the crystallisation transition, we choose to have N distinct Gaussian orbitals, one for each atom in the system. In this case, the positions of the orbitals are also optimisable. This choice produces much more accurate trial wavefunctions in the crystallised case at the cost of an increased number of optimisable parameters, which generally increases computation time. The two body terms are used to impose coalescence conditions on the wavefunction. At coalescence of two particles, due to the magnetic dipole-dipole potential, the local energy (42) would diverge as $1/r^3$. For the isotropic dipole potential of the form μ^2/r^3, the term $u_d(r) = -\sqrt{8\mu^2 M_r/r}$ would be included, where M_r is the reduced mass of atom pairs, to ensure the wavefunction goes to zero at coalescence points. These calculations include this term even though an anisotropic potential is used instead. In all cases, the trap geometry keeps the dipole-dipole potential primarily repulsive, making it difficult for atoms to move into regions where the anisotropy would be apparent. These choices ensure that local energy only has positive energy divergences. A positive divergence kills off walkers and can result in regions of configuration space being inadequately explored. Negative divergences instead create population explosions; these are much more problematic and can crash calculations. When the Lennard-Jones potential is included in calculations, similar terms are included that go as $-1/r^5$ imposing the exact behaviour at coalescence of the repulsive r^{-12} part of the potential [20].

This wavefunction optimisation in the VMC step is done using brute-force energy minimisation. Other minimisation methods are available, such as variance minimisation, which are generally

faster but were occasionally found unreliable for this particular system. This unreliability is likely due to the lack of an exact coalescence condition for the dipole-dipole potential and the propensity of the VMC calculation to converge to a local minimum rather than the ground state.

Once an optimised trial wavefunction is calculated, we find realisations of the ensemble using the DMC calculation. The stability and efficiency of the DMC calculation depend on the accuracy of the trial wavefunction. Generally, the trial wavefunction found in the VMC step is adequate in the DMC calculation. However, it can sometimes fail near the system's transition into crystallisation or if the system has crystallised but the Gaussian orbital centres were not optimisable parameters in the VMC step, Eq. (43). When these problems with the trial wavefunction arise, they can cause longer compute times for the DMC or VMC calculations if the trial wavefunction needs to be re-calculated. Secondly, directly optimising the trial wavefunction in the strongly interacting cases (either near or after crystallisation) can be challenging even when the trial wavefunction has adequate degrees of freedom. As the interaction strength increases, the system's ground state deviates further from the analogous non-interacting ground-state wavefunction. Therefore, generating an optimised wavefunction using the non-interacting ground state as an initial wavefunction becomes increasingly difficult with greater interaction strength. This problem was mitigated by performing VMC calculations in series with increasing interaction strength. In each subsequent calculation, a trial wavefunction from an earlier (weaker interaction) case is used as the initial wavefunction. This choice improves the fit of the initial wavefunction to the ground state at larger interaction strengths while necessarily serialising calculations, which adds to the compute time. If the system had already crystallised, the VMC wavefunction was sometimes calculated by first solving the classical analogue problem. The positions of the classical atoms in this system were then used as initial positions of the Gaussian orbitals in the localised wavefunction form.

3.3 Code implementation and commutation time

3.3.1 Optical expectation values

To calculate the optical expectation values of Sec. 3.1.1, after the DMC calculation has been completed, a subset of the configurations obtained is used to calculate the ensemble average. Configurations from the equilibration stage of the DMC calculation are not used, and only configurations sufficiently spaced in imaginary time (to un-correlate the realisations) are used in the analysis. For each included atomic configuration $\mathbf{R}_\sigma$, where σ is an index identifying the realisation, the steady-state polarisation of the atoms is calculated according to Eq. (19). The steady-state solution of the polarisations $\mathbf{b}_\sigma$ (Eqs. (15),(18)) is found by numerically solving

$$A_\sigma \mathbf{b}_\sigma = \mathbf{F}_\sigma, \tag{44}$$

where $A = -i\mathcal{H}$, using lower-upper factorisation with partial pivoting. The scattering at the lens from each atom of realisation σ is then calculated from Eq. (32). By inserting the sub-vector of $\mathbf{b}_\sigma$ corresponding to the l'th atoms' polarisation into Eq. (32), the scattering due to the l'th atom is calculated. The total scattered field from realisation σ, $\left(\mathbf{E}_{\mathrm{S}}^{+}\right)_\sigma$ is the sum of the scattered fields from the N atoms in the realisation. The relevant ensemble averages from Eqs. (28),(29) are then calculated. Finally, the transmission and reflection are calculated for given beam detunings Δ using trapezoid integration in cylindrical coordinates. The integral of the numerators of Eqs. (24),(25) are found analytically using Eq. (80). When calculating transmission and reflection (coherent or incoherent) with beam detuning, to speed up calculations, the integration tolerance is tested on a sub-sample of the desired detunings Δ to a tolerance of 0.1%. The number of evaluation points in both dimensions needed to achieve this tolerance is recorded; the remaining calculations then use this number of evaluation points. The validity of the calculations is also checked against the requirement that $R + T \leq 1$. The total reflection and transmission can be less than one since the lens may not necessarily capture all of the scattered intensity, but this value should be close to one and not larger than one.

It was found that VMC-DMC calculations for systems of 50 atoms take a few hours to around a day or two on the HEC cluster, depending on how simple the VMC optimisation is and if the process had to be serialised with interaction strength. Transmission and reflection calculations take of order an hour to complete for similar atom numbers.

3.3.2 Eigenmode analysis

The eigenmodes of the system are calculated via the interaction matrix $\mathcal{H}$ Eq. (17) using standard routines included in MATLAB to calculate the eigenvalues and associated eigenvectors of $\mathcal{H}$. For each system realisation σ, the interaction matrix $\mathcal{H}_\sigma$ is calculated from the atom positions $\mathbf{R}_\sigma$. The eigenmodes of realisation σ are then calculated, and from the eigenvalues, the collective resonances and linewidths of each mode are extracted according to Eq. (21). If only the eigenmodes of the system are required, it is not necessary to find the system's steady-state polarisation; the available eigenmodes of the system are entirely dependent on the atom positions. However, suppose the occupation of modes is needed. In that case, this requires knowing the steady state solution $\mathbf{b}$, which is found by solving equation Eq. (44) for driving field $\mathbf{F}$. For each mode p in each sampled realisation σ, the occupation of the mode L_p can be calculated according to Eq. (22). This occupation can be normalised across single or multiple realisations by changing the sum in the denominator.

4 Results

This section presents the results of various investigations into how 1D and 2D collections of dipolar atoms respond optically. The results start by looking at the optical response of weakly magnetically interacting systems before on to crystallised systems where magnetic interactions are large.

We begin by demonstrating how a 2D system of non-magnetic atoms responds optically depending on the density of the sample. This behaviour will inform how we determine what effects result from magnetic interactions alone. Following that, we study how a 2D system of interacting dipoles responds optically dependent on density and magnetic interaction strength, with reference to how the occupied eigenmodes of the system change in both cases. We also study how the polarisation of dipoles in the sample changes with density and interaction strength, and consider how Zeeman splitting from nearby dipoles modifies the optical response. Finally, we consider the 1D case of atom chains when the magnetic interactions are not too strong. There is no splitting between the magnetic sub-levels in these systems except when including local Zeeman shifts. These results closely follow those presented in [20], although

4-level, rather than 2-level atoms, are simulated here.

After considering the weakly interacting case, I look at systems that crystallise due to strong interactions. Both the 1D and 2D cases of crystallisation are considered. I look at how the optical response of crystallised systems differs from the weakly interacting case in terms of the system's scattered light and the excitable collective eigenmodes. Two beam orientations are considered here to study both in-plane and out-of-plane modes. In these systems the magnetic sub-levels are assumed to be degenerate.

4.1 2D weakly interacting systems

4.1.1 Non-interacting system

Before studying how the introduction of magnetic interactions modifies the optical response of the sample, it is instructive to look at how a non-interacting sample behaves. In Fig. (2) a sample of atoms is held in a symmetric pancake-shaped trap. In each dimension x, y, z, the trap has the length scale

$$\ell_i = \sqrt{\hbar/M\omega_i}, \tag{45}$$

where i is the dimension index. The trap is chosen to be symmetric in the $x-y$ plane, meaning $\ell_x = \ell_y$. The aspect ratio of the trap, between the long and short dimensions, is given by $\ell_x/\ell_z = 18$. The atom positions in the sampled according to the Gaussian distribution,

$$|\Psi(\mathbf{R})|^2 = \frac{1}{\ell_x\ell_y\ell_z\pi^{3/2}} \exp\left(-[x/\ell_x]^2 - [y/\ell_y]^2 - [z/\ell_z]^2\right), \tag{46}$$

the square modulus of the non-interacting ground state wavefunction. The density of the sample is modified by changing the number of atoms in the sample. A Gaussian beam is incident on the sample with a width $W_0k = 18, \ell_z = 1/k$ and linear polarisation $\hat{\mathbf{e}}_x$. A schematic of the system's set-up can be seen in Fig. (3, a). When the sample is at low density, the optical response line shape fits a Lorentzian, showing that the atoms in the sample act largely independently. As the density increases, the line shape deviates from the Lorentzian, forming multiple peak resonances. There is also a pronounced density-dependent resonance shift, seen clearly in the coherent transmission and reflection. These changes in optical response are due to the emergence of collective behaviour in the sample and are the results of the increased density of the sample. Finally, with increased density, due to a large

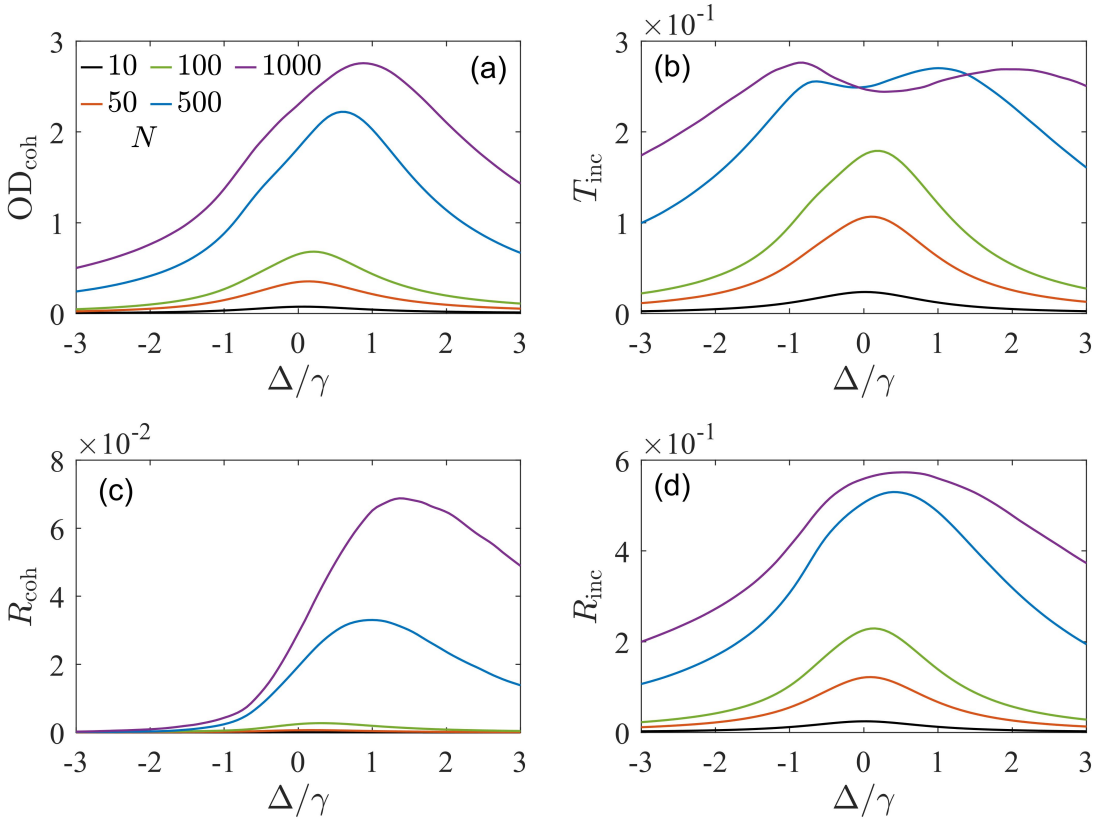

Figure 2: Transmission and reflection of non-interacting atoms held in a pancake-shaped trap of aspect ratio $\ell_x/\ell_z = 18$, as a function of beam detuning from the single atom transition frequency Δ [Eq. (3)], for different atom numbers N and no magnetic sub-level splitting. A Gaussian beam of width $W_0 k = 18$ and polarisation $\hat{\mathbf{e}}_x$ [Eq. (2)] propagating normal to the trap plane illuminates the system, where $\ell_z = 1/k$. Each sample has peak density $\bar{\rho}_{2\mathrm{D}}/k^2 = 0.01, 0.05, 0.1, 0.5, 1$ for atom numbers $N = 10, 50, 100, 500, 1000$ respectively. (a) Coherent transmission as an optical depth $\mathrm{OD}_{\mathrm{coh}}$ [Eq. (31)], (b) incoherent transmission T_{inc}, (c) coherent reflection R_{coh} and (d) incoherent reflection R_{inc} [Eqs. (24)-(29)].

increase in the number of atoms, greater scattering is seen and also increased optical depth, which is to be expected. Increasing the sample density without increasing the atom number may reduce this effect. Therefore, when studying the change in the optical response due to magnetic interactions, we need to consider the density carefully.

4.1.2 Introduction of magnetic interactions

The introduction of dipole-dipole interactions to the sample will modify the distribution of atoms. This is the mechanism by which the response will be modified. The modification of the sample shape is independent of the interacting light, therefore we need to be able to quantify the interaction strength in a wavelength independent manner. This interaction strength can be quantified by the 'ratio' $R_{\mathrm{dip}}\left(\bar{\rho}_{D\mathrm{D}}\right)^{1/D}$, where D is the dimensionality of the system, R_{dip} is the dipole-dipole interaction length scale, Eq. (37) and $\bar{\rho}_{D\mathrm{D}}$ is the D-dimensional peak density of the sample. So for example in 2D this would be $R_{\mathrm{dip}}\left(\bar{\rho}_{2\mathrm{D}}\right)^{1/2}$. This gives the ratio between the interaction length and the minimum average separation between atoms in the sample; this quantity will be referred to as the 'interaction strength'. For clarity, throughout the work systems will be referred to as 'interacting' and 'non-interacting' or 'weakly' or 'strongly interacting' etc. referring to whether they are interacting via magnetic dipole-dipole interactions or how strong these interactions are. It is assumed that in all the optical systems the atoms are interacting with the incident field and with each other optically.

4.1.3 Sample density and size

The introduction of magnetic dipole-dipole interactions modifies the shape and density profile of the sample as well as correlations between atom positions. Specifically, with all other parameters remaining equal, the system tends to get larger and more dilute with interaction strength. Shown in Fig. (3) is the increase in 2D radius

$$\varrho = \sqrt{x^2 + y^2} \tag{47}$$

and decrease in 2D density $\rho_{2\mathrm{D}}$ of a sample of 100 dipoles as the magnetic interaction length R_{dip} is increased, for a fixed trap geometry with $\ell_x/\ell_z = 100$. For this fixed geometry the sample widens with interaction length R_{dip}. When introducing interactions, changes in the density and size of the sample can complicate the study of its optical response, as seen from

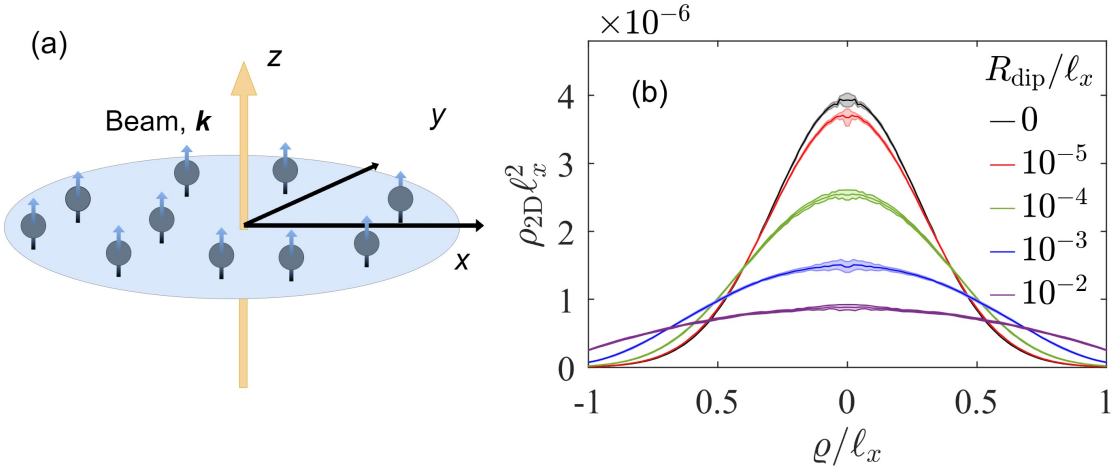

Figure 3: (a) Schematic of atom trap and incident beam. The sample of atoms is held in a pancake-shaped trap in the x-y plane. Each atom has an internal magnetic dipole aligned perpendicular to the trap plane. The incident light propagates perpendicular to the trap plane with wave-vector $\mathbf{k}$. (b) 2D density, $\rho_{2D}\ell_x^2$, of a sample of 100 atoms plotted for different interaction lengths R_{dip} [Eq. (37)] for fixed trap geometry, $\ell_x/\ell_z = 100$ [Eq. (45)]. The curves show the 2D density ρ_{2D} of each sample as a function of radial distance ϱ [Eq. (47)] from the centre of the trap. 10000 realisations of each sample were used. The sample widens and becomes less dense with increased interaction length. Specifically, the peak 2D density $\bar{\rho}_{2D}$ decreases with interaction strength.

Sec.4.1.1. Firstly, because the sample changes size with interaction strength, the size of the incident Gaussian beam needs to be modified correspondingly. The width of the beam will need to be matched so that it continues to illuminate the whole sample as the size changes. The width of the beam would ideally be chosen so that each atom has the same incident power on it. However, since the sample profile will deviate from a Gaussian in the interacting case, it is impossible to do this. Still, the choice of width should aim to illuminate the sample as evenly as possible. Secondly, we can see from Fig. (2) that a change in density in terms of k will modify the optical response, independent of the magnetic interactions. Because of this, when modifying the interaction strength, we have two approaches available to isolate the two effects.

1. The density can be modified for a constant dipole interaction length. The interacting case must then be compared to the non-interacting analogue at the same density.

2. The interaction length can be modified in terms of the density while maintaining a constant density in terms of k

I will begin by studying how the optical response changes with density for an interacting and non-interacting system. Then, I will consider changing the interaction strength via the density in terms of R_{dip} while maintaining constant density in terms of k.

4.1.4 Transmission at fixed interaction strength with density

We study how the density of the sample modifies the optical response for fixed interaction length $R_{\mathrm{dip}}k = 0.1, 0,$ [Eq. (37)]. A system of 200 atoms is studied, and the density is modulated by varying the trap parameters (see Fig. (4)). The density is modulated by varying $\ell_x k$ while keeping the aspect ratio of the sample constant $\ell_x/\ell_z = 25,\ \ell_x = \ell_y$. This choice is made to ensure that the sample is always quasi-2D throughout. If, instead, the aspect ratio was altered when the density was modified, it would be possible for a transition from 2D to 3D to be causing changes in the optical response. The incident beam has a circular polarisation of $\hat{\mathbf{e}}_+$ [Eq. (2)] and propagates along the z-axis, perpendicular to the plane of the trap, (Fig. (3, a)). A lens $zk = 10000$ away from the sample with NA [Eq. (26)] of $0.2,\ 0.8$ collects the coherent and incoherent scattering respectively. This choice is made because the coherent scattering is mostly directed along the optical axis while the incoherent scattering is more broadly directed. In principle, a large lens could collect both since it would also capture the coherent scattering. However, the coherent scattering will have negligible intensity over a large fraction of the surface of such a lens. The intensity from this region contributes insignificantly to the convergence of the integral, negatively impacting the calculation speed (Eq. (24)). Instead, in each case, the lens size is chosen to be as small as possible while still capturing the majority of the intensity; this allows the integration to be as fast as possible without losing accuracy.

The optical response of the interacting case is compared to non-interacting systems of comparable peak 2D density, $\bar{\rho}_{\mathrm{2D}}$. The optical response of both the interacting and non-interacting cases is similar qualitatively but deviates at high density. As the density increases, the line shape in both cases broadens but broadens more dramatically in the interacting case. There is a significant increase in the scattering for red-detuning in the interacting case, which is missing in the non-interacting case. In Fig. (5), the response of the two most dense cases (for both interacting and non-interacting samples) is shown over a larger range of detunings

since the line shapes have broadened significantly in these cases. Both the interacting and non-interacting cases also show an asymmetry in response to detuning, having more scattering for red-detuning and an increased optical depth for blue detuning.

We can investigate more precisely how the width and peak of the individual line shapes vary with interaction strength. If the optical response was Lorentzian, we could define the linewidth by fitting the line shape to a Lorentzian. However, since many of the curves are not Lorentzian, this approach would not work. Instead, for clarity for each curve $Y(\Delta/\gamma)$ with maximum value $\max(Y)$, the HWHM can be defined by the detuning values for which the curve is $1/2$ of the peak value, $X = Y^{-1}(\max(Y)/2)$. There will be two solutions to this X_1, X_2. The half-width of the line shape is then defined as $\mathrm{HWHM} = |\mathrm{X}_1 - \mathrm{X}_2|/2$. Defining the half-width this way allows the width of the line shape to be well-defined for Lorentzian and arbitrarily shaped curves. The peak resonance will be denoted δ_{peak}.

Both the interacting and non-interacting cases broaden substantially with increased density by of order a factor of 10, see Fig. (5,6(c)). However, the interacting case is significantly more broadened than the comparable non-interacting case. The increased broadness of the line shape at high density implies modes are more easily excited at large detuning, most likely due to the increased availability of modes with large collective resonance. There is also a trend in the peak scattering in both cases; the peak value first increases significantly and then decreases for very high density. This behaviour may imply that as the density increases, multiple different eigenmodes become resolved in terms of detuning. At low density, modes can only be excited near the single-atom resonance, and the peak scattering is the sum of the scattering from these modes. As the density increases, these modes separate spectrally, and multiple peaks emerge. Since these modes are now excited at different detunings, we should expect the peak scattering to decrease. As well as the emergence of various peaks and a broadening of the line shape, we see a shift of the peak resonant frequency, particularly in the coherent scattering. These behaviours together imply a complex relationship between density and the availability and occupation of eigenmodes in the system, with the introduction of magnetic interactions modifying this further. To understand how the eigenmodes change with density, with and without interactions, we first need to know how the distribution of atoms varies in both cases.

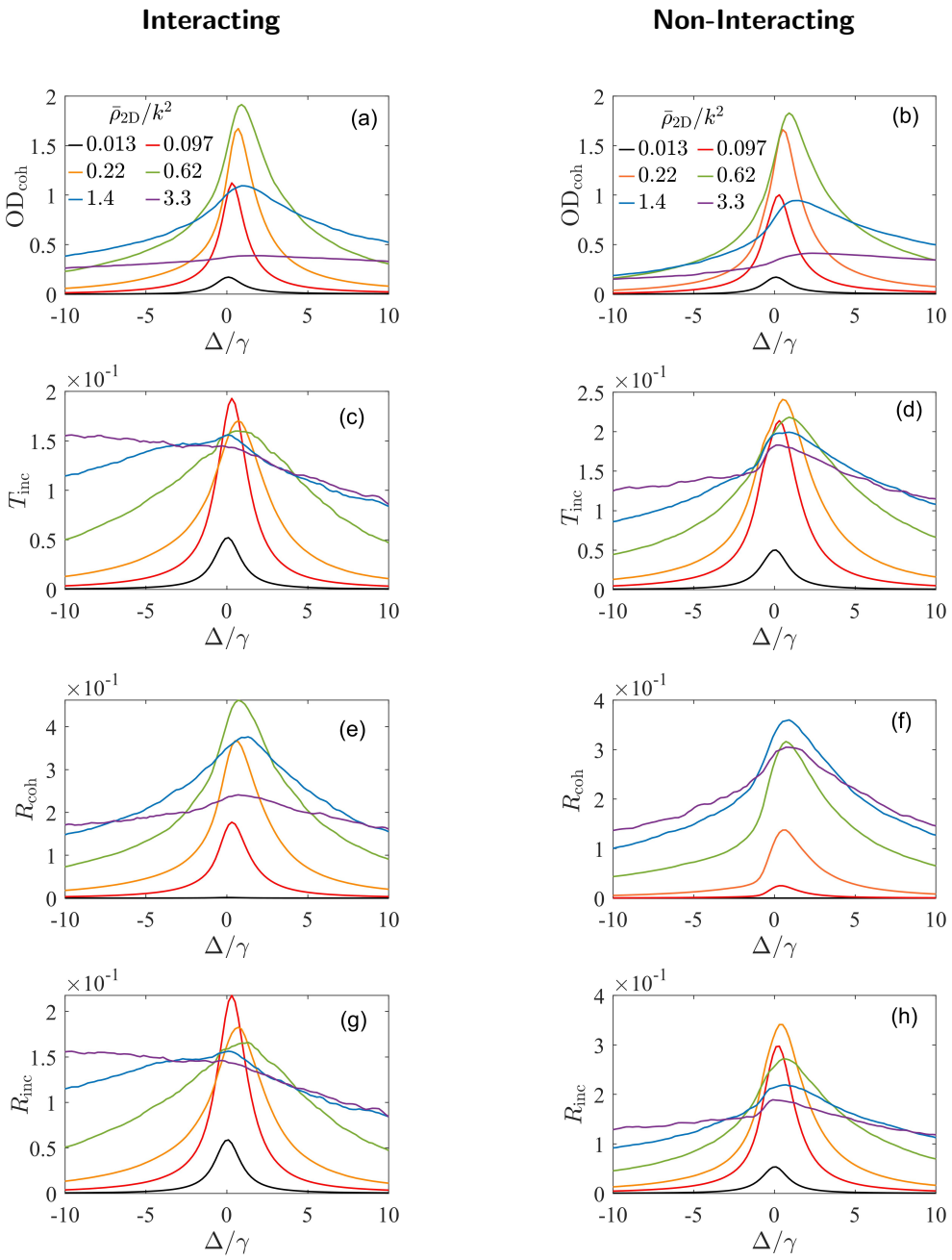

Figure 4: Transmission and reflection from samples of 200 atoms, with no magnetic sub-level splitting, held in a pancake-shaped trap ($\ell_x/\ell_z = 25$) for peak densities $\bar{\rho}_{2D}/k^2 = 0.013, 0.097, 0.22, 0.62, 1.4, 3.3$. The left column shows the optical response of interacting systems with interaction strengths $R_{\mathrm{dip}}\sqrt{\bar{\rho}_{2D}} = 0.011, 0.028, 0.047, 0.079, 0.12, 0.18$, respectively ($\ell_z k = 1, 0.32, 0.18, 0.10, 0.05, 0.032$ and $\ell_x k = 25, 8.0, 4.4, 2.5, 1.4, 0.8$). In contrast, the right column shows the response of non-interacting analogues with matched peak densities ($\ell_z k = 2.8, 1.0, 0.68, 0.41, 0.27, 0.18$, $\ell_x k = 70, 26, 17, 10, 6.8, 4.4$). Each sample has incident on it a Gaussian beam matched to the width of the sample with polarisation $\hat{\mathbf{e}}_+$. (a,b) Coherent transmission as an optical depth $\mathrm{OD}_{\mathrm{coh}}$ [Eq. (31)], (c,d) incoherent transmission T_{inc}, (e,f) coherent reflection R_{coh} and (g,h) incoherent reflection R_{inc} [Eqs. (24)-(29)] for beam detuning from the single atom transition frequency Δ [Eq. (3)].

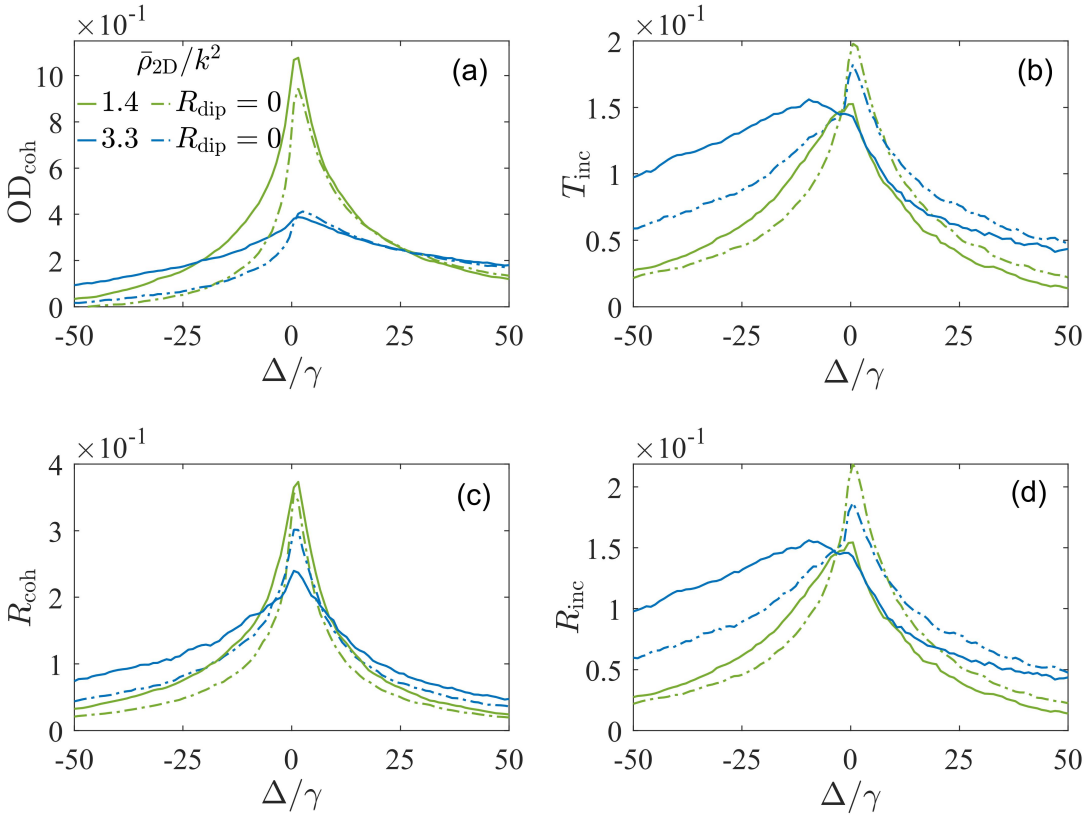

Figure 5: Optical response of samples of 200 atoms as in Fig. 4 with detuning over a larger detuning range. The trap has a fixed aspect ratio of $\ell_x/\ell_z = 25$. The interaction strength for each case is $R_{\rm dip}\sqrt{\bar{\rho}_{2D}} = 0.12, 0.18$, with peak densities, $\bar{\rho}_{2D}/k^2 = 1.4, 3.3$ respectively. The dashed curves show the response of comparable non-interacting systems with matching peak densities. $\ell_z k = 0.05, 0.032, \ell_x k = 1.4, 0.8$ in the interacting systems, $R_{\rm dip}\sqrt{\bar{\rho}_{2D}} = 0.12, 0.18$ respectively while $\ell_z k = 0.27, 0.18, \ell_x k = 6.7, 4.4$ in the non-interacting analogues. A Gaussian beam with polarisation $\hat{\mathbf{e}}_+$ and width matched to the sample is incident on each sample. (a) Coherent transmission as an optical depth $\mathrm{OD}_{\rm coh}$ [Eq. (31)], (b) incoherent transmission $T_{\rm inc}$, (c) coherent reflection $R_{\rm coh}$ and (d) incoherent reflection $R_{\rm inc}$ [Eqs. (24)-(29)] for beam detuning from the single atom transition frequency Δ [Eq. (3)].

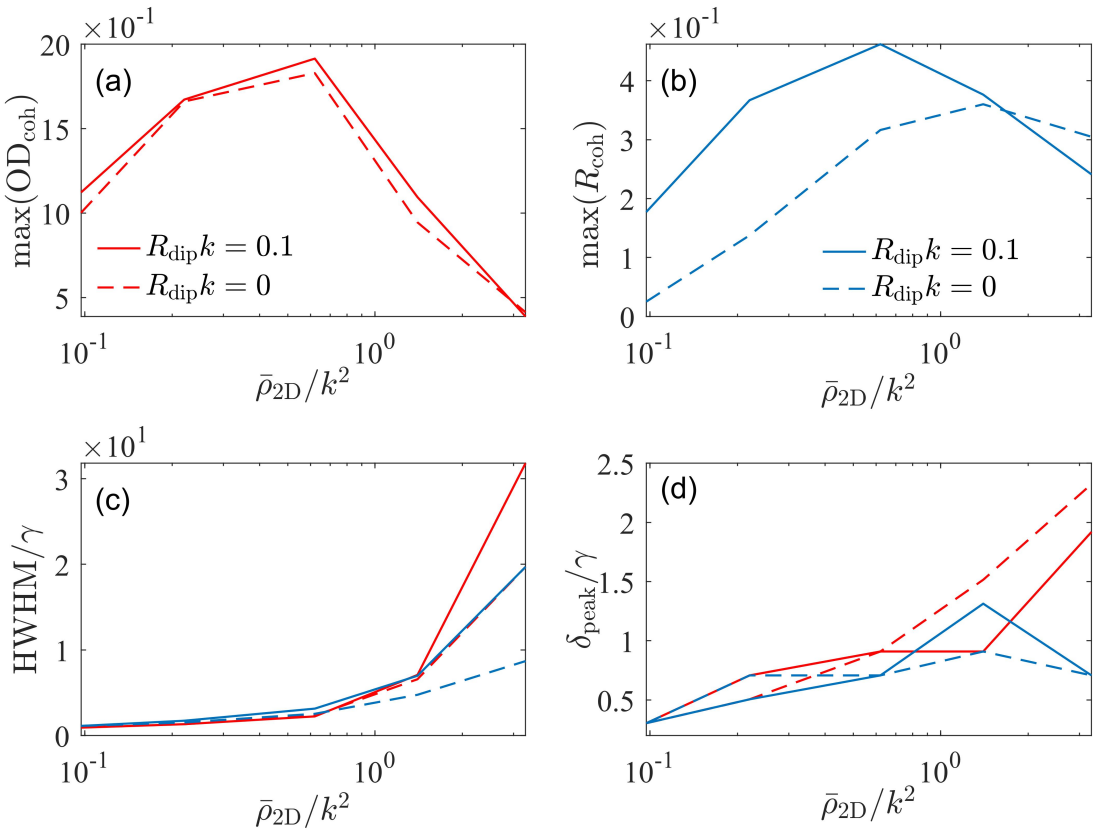

Figure 6: Variation of peak scattering, linewidth and peak resonance with density for the interacting and non-interacting 200 atom systems with fixed interaction length from Fig. (4). (a) Peak optical depth $\max(\mathrm{OD}_{\mathrm{coh}})$, with increasing density for the interacting and non-interacting cases. (b) Peak coherent reflection $\max(R_{\mathrm{coh}})$ (c) HWHM of the coherent response (d) Peak resonant frequency of the coherent response. The non-interacting comparison in each case is shown with a dashed line. The blue (lower) lines show the coherent reflection and the red (upper) lines show the optical depth.

4.1.4.1 Atom correlations

The change in optical response with density in both the interacting and non-interacting cases is due to the change in the distribution of atoms in the sample, specifically the distribution of separations between the atoms. This distribution defines the collective eigenmodes of the system via Eq. (19). Fig. (7) shows the probability of atom pairs having separation dk in the sample of 200 atoms. Shown separately are the distributions for all atom pairs $P(d_{\mathrm{aa}}k)$ and only nearest neighbours $P(d_{\mathrm{nn}}k)$, referred to as the 'nearest neighbour' and 'all-atom', respectively. The set of separations $\{d_{aa}\}$ is the set of distances $d_{ij} = |\mathbf{r}_i - \mathbf{r}_j|, i \neq j$ for all atoms i, j in the system, whereas $\{d_{nn}\}$ is the set $d_{ij} = |\mathbf{r}_i - \mathbf{r}_j|, i \neq j$ where for each i only the minimum value of d_{ij} across all j is included. The distributions shift to shorter separations with increased density, as expected, but the shape and width of the distribution also vary between the two cases. When interactions are introduced, the atoms become confined to a smaller range of possible separations, with short and large separations being suppressed. The change in optical response from increased density is due to the shift of the distribution to the left, while the change due to interactions results from the change in the width and shape of the distribution instead.

4.1.4.2 Eigenmode availability with density

The change in density of the system modifies the distribution of atom separations in the system, modifying the eigenmodes available in the system. The change in optical response with increased density and interaction strength can be understood by considering the change in the available eigenmodes of the system. Firstly, we look at how the available eigenmodes change with density.

If the collective resonances of available modes change, this will potentially allow for greater excitation of different modes at different detuning values. These shifted modes are potentially subradiant or superradiant as well. The available collective eigenmodes of the system can be shown as points in the plane where each eigenmode is shown as a point defined by its collective linewidth ν and collective resonance δ.

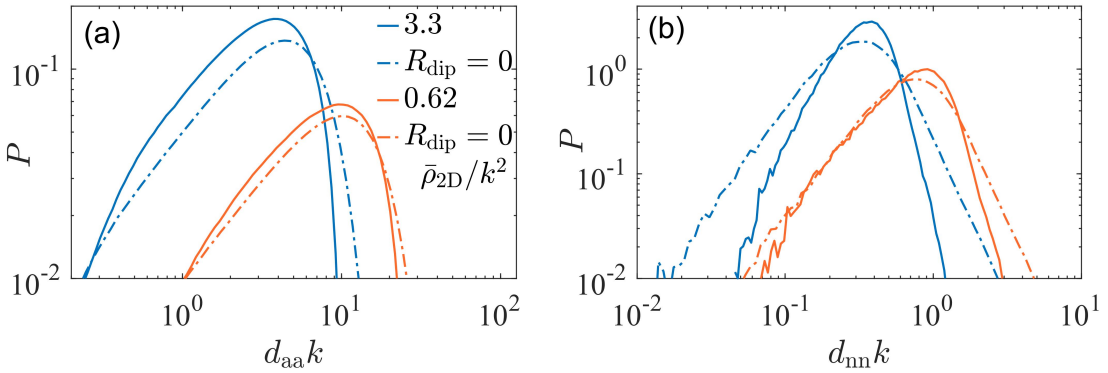

Figure 7: probability of atoms in 200 atom samples having interparticle-separations d/k for varied density and interaction strengths. The samples shown are a selection from Fig. (4). (a) Probability $P(d_{\mathrm{aa}}k)$ of all-atom pair separations $d_{\mathrm{aa}}k$. (b) Probability $P(d_{\mathrm{nn}}k)$ of nearest neighbour separations $d_{\mathrm{nn}}k$. The atom samples are held in a pancake-shaped trap with aspect ratio $\ell_x/\ell_z = 25, \ell_x = \ell_y$, and have peak densities $\bar{\rho}_{2\mathrm{D}}/k^2 = 3.3, 0.6$ for the blue and orange curves respectively. The solid and dashed curves correspond to interacting systems and their analogous non-interacting systems. $R_{\mathrm{dip}}\sqrt{\bar{\rho}_{2\mathrm{D}}} = 0.18, 0, 0.079, 0$ where $\ell_z k = 0.032, 0.018, 0.10, 0.41, \ell_x k = 0.8, 4.4, 2.5, 10$ respectively according to the legend ordering.

The eigenmodes of the system of 200 atoms are studied with varied densities in terms of incident beam wavenumber k. First, we study the non-interacting case to exclude the impact of interactions. From a collection of 100 realisations of the ensembles, the eigenmodes present are binned in terms of their resonant frequency and linewidth. The probability P that a mode δ/γ, ν/γ, is found in the system is calculated for increasing density of the system, Fig. (8). The linewidth is plotted on a logarithmic scale to differentiate different subradiant modes better. P is plotted against the negative of the collective resonance so that features in transmission and reflection curves with detuning align on the x-axis. These conventions will be used throughout when showing collective eigenmodes in terms of linewidth and resonance.

In the low-density case (a), the available eigenmodes are concentrated around the single-atom resonance and linewidth, as is to be expected, since the atoms are responding mostly independently to the incident field in this case. The most common eigenmode is also at exactly the single atom linewidth and resonance. With increasing density, the central region's size increases in width in terms of resonance and linewidth. The distribution also forms long arms extending into regions of large collective resonance. These arms have linewidths corresponding

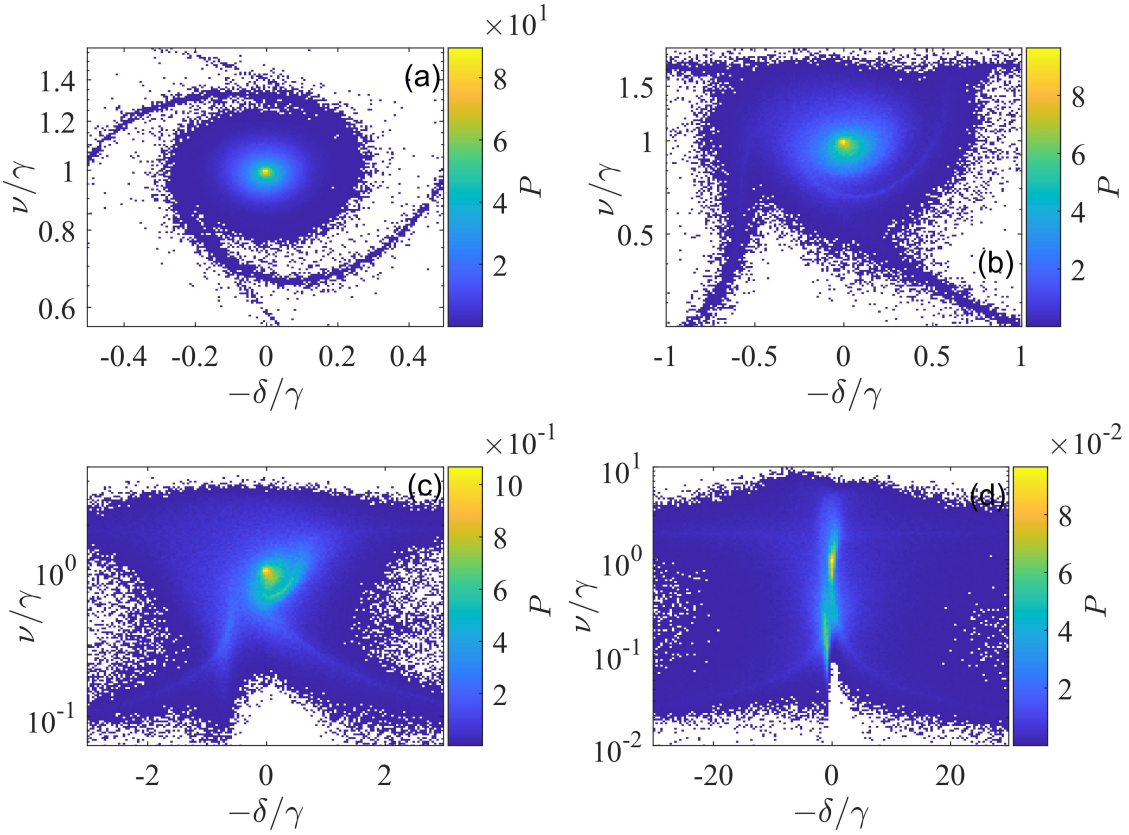

Figure 8: The available eigenmodes of 200 non-interacting atoms in a pancake-shaped trap with varied densities. The trapping aspect ratio is $\ell_x/\ell_z = 25$ throughout, while the density varies by adjusting the trap width relative to k. The collective eigenmodes are represented on the complex plane by points, where the coordinates of each point are the collective linewidth and resonance shift of the given eigenmode. The linewidth is shown on a log scale because subradiant modes have linewidths that approach zero. Plotting on a linear scale can cause a loss of detail in the subradiant modes. The colour shows the probability that an eigenmode, $\nu/\gamma, -\delta/\gamma$, is found within the set of stochastic realisations of the samples. The systems in each case (a,b,c,d) have densities $\bar{\rho}_{2D}/k^2 = 0.001, 0.01, 0.1, 1$. Shown are 100 realisations of the 200 atom samples.

to either super- or subradiant modes and can be seen most clearly in (c) and (d); one pair of arms has a super radiant linewidth $\nu/\gamma \approx 2$ while the other two are subradiant with linewidths $\approx 0.1\gamma$. These modes appear when pairs of atoms in the sample have small separations. We would expect to see more of these closely spaced pairs of atoms and, therefore, more of these kinds of modes as we increase the density of the sample, which we do (Fig. (8)). We can also see that as the density increases, the collective resonances of the modes in these arms increase, which is clearly seen in Figs. (8b,d). This implies that closely spaced atom pairs produce these kinds of modes in the system and that, as the separation decreases, the collective resonance of these modes is pushed further from the single atom resonance. We will also see in later sections (Fig. (14)) that with increased magnetic interactions, the arms become less apparent as these closely spaced pairs are suppressed, in line with Fig. (7). These modes are not very common in the system but can be accessed with large detuning as we will see later (Fig. 10). This change in available eigenmodes allows for the increased linewidth seen with increased density. As the density increases, there are more collective modes to excite with resonances further from the single-atom resonance. The distribution also becomes significantly asymmetrical as the density increases. The most prevalent mode shifts in collective resonance to the right in line with the density-dependent shift seen in the optical response, Fig. (4). This shift can be seen most clearly in Fig. (8c). The increase in density also gives rise to multiple regions with prevalent eigenmodes. In (c), there is a second region below the most likely mode, while in (d), a second region with red-detuning is seen, with a subradiant linewidth.

The change in density changes the available collective modes of the sample, but the availability of eigenmodes alone does not fully explain the change in optical response. The lack of highly shifted cooperative modes at low density does prevent modes with large collective resonance from being excited because they do not exist. However, simply because such modes exist at high density does not mean they can be excited by the incident beam. The availability of modes is necessary but not sufficient to explain the change in optical response. Instead, we need to look at the occupation of these modes.

4.1.4.3 Eigenmode occupation with density

When studying the eigenmodes of the system and how they contribute to total scattering, it is useful to introduce the binned occupation $\tilde{L}(\delta,\nu)$. This is the value of the total occupation [Eq. (22)] of all the modes found in a bin $S_{\delta,\nu}$.

$$\tilde{L}(\delta,\nu)=\sum_{p\in S_{\delta,\nu}} L_p, \tag{48}$$

$$S_{\delta,\nu}=\left\{(u,w)\in\mathbb{R}^2 : |u-\delta|\leq \frac{\varkappa}{2}, \log_{10}\left(|w-\nu|\right)\leq \log_{10}\left(\frac{\eta}{2}\right)\right\}, \tag{49}$$

where L_p is given by [Eq. (22)] and the sum over p is over all the eigenmodes across all of the realisations found in $S_{\delta,\gamma}$, not just a single realisation. $\varkappa$ and η are small and define the width and height of each bin. The sum is normalised such that the sum of the binned occupations over all bins is one,

$$\sum_{\delta}\sum_{\nu}\tilde{L}(\delta,\nu)=1. \tag{50}$$

This choice matches the normalisation of the occupation, the sum total of which is also one. The binned occupation of the eigenmodes indicates how excited a particular eigenmode in the system is based on the incident field. It is also useful to be able to consider the total occupation across all collective resonances for a single linewidth,

$$\tilde{L}_{\delta}(\nu)=\sum_{\delta}\tilde{L}(\delta,\nu). \tag{51}$$

The availability of eigenmodes alone does not consider how closely the beam polarisation and detuning match each collective eigenmode. Simply because a particular eigenmode is very common does not mean it is easy to excite, so we need to study how the occupation behaves for the system.

In Fig. (9), I look at how the occupation of eigenmodes in the sample of 200 atoms, from Fig. (4) varies with density. I look at the interacting systems at zero detuning and a detuning of 3γ.

At low density, the change in occupation with detuning is minimal. It should be noted the binned occupation is normalised so that the total occupation across all collective resonances and linewidths will be one, which is why the magnitude of the occupation does not change

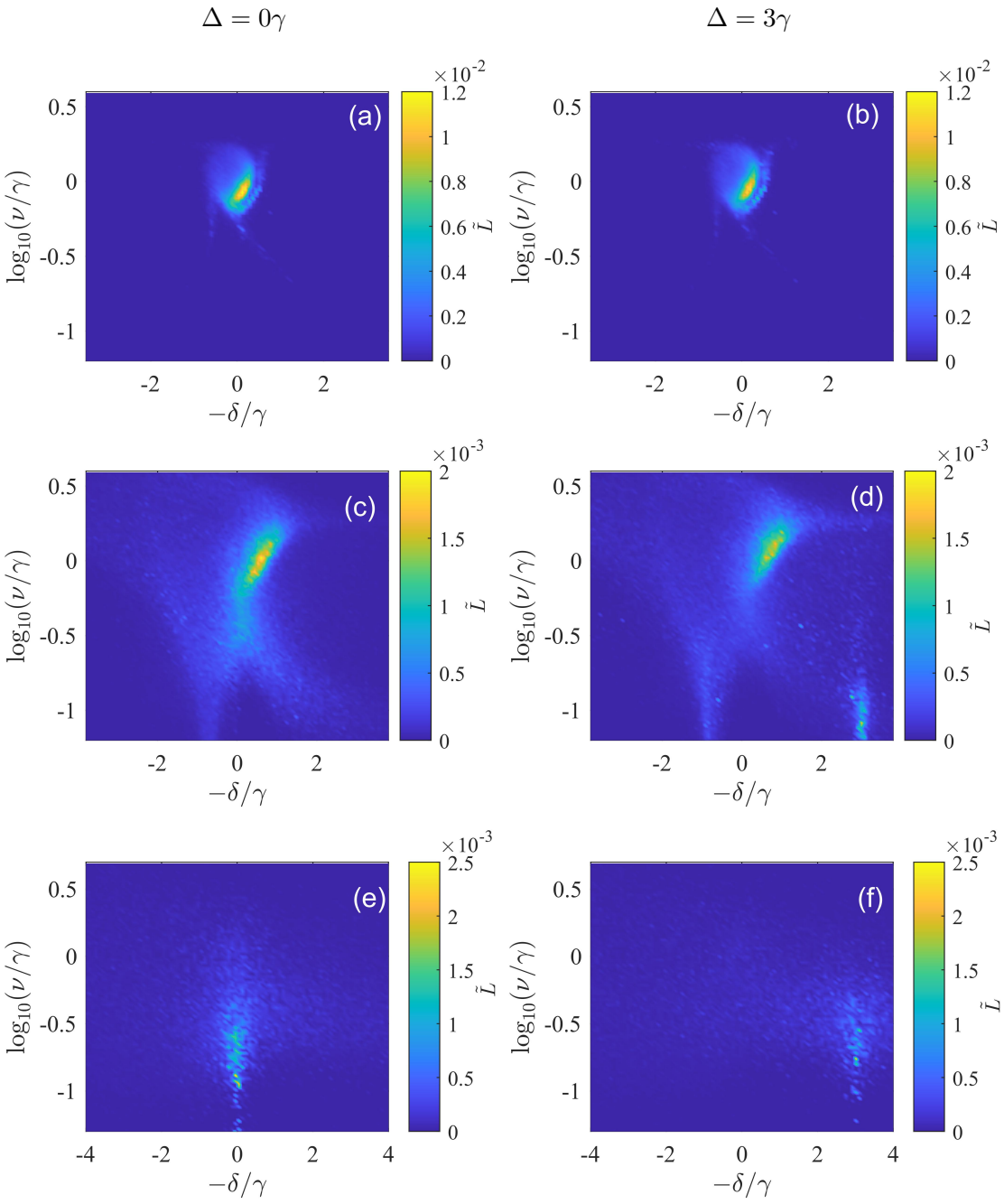

Figure 9: Occupation of available eigenmodes in samples of 200 dipolar atoms held in a pancake-shaped trap of fixed aspect ratio of $\ell_x/\ell_z = 25$ where there is no magnetic sub-level splitting. A Gaussian beam of matched width and polarisation $\hat{\mathbf{e}}_+$ is incident on each sample. (a,b),(c,d),(e,f) Eigenmode occupation where interaction strength for each case is $R_{\rm dip}\sqrt{\bar{\rho}_{\rm 2D}} = 0.011, 0.079, 0.18$, with peak densities, $\bar{\rho}_{\rm 2D}/k^2 = 0.013, 0.22, 1.4$ respectively, where $\ell_z k = 1, 0.18, 0.05, \ell_x k = 25, 4.4, 1.4$. (a,c,e) Eigenmode occupation for detuning 0γ, (b,d,f) Eigenmode occupation for detuning 3γ.

with detuning. We should expect that modes with resonances far from the detuning will not be as well excited as modes that are resonant with the detuning. Therefore, at low density ($\bar{\rho}_{2D}/k^2 = 0.013$), the same mode is excited for a broad range of detuning. Still, it becomes less excited with greater detuning, matching the Lorentzian profile of the optical response. When the density increases to $0.22k^2$, the occupation begins to change with detuning. The mode primarily occupied for zero detuning is still occupied with 3γ detuning. However, a subradiant mode is now near this detuning that is also being occupied. Subradiant modes are modes with a linewidth smaller than the single atom linewidth, while superradiant modes have a larger linewidth. For high density $1.4k^2$, the occupation becomes prominent only around modes with resonance matching the detuning; there is little occupation of modes away from this resonance.

Therefore, the chosen incident beam can excite the modes made available by larger density. Thus, the increase in linewidth of the optical response with density results from the increased availability of collective modes with larger collective resonance frequencies. In particular, for strong interactions, the excitation is centred only around the detuning, explaining the very broad line shape we see in that case.

Finally, we can study how the occupation of modes changes between interacting and non-interacting systems, specifically at densities high enough that the optical response is likely to be cooperative. We will examine this more in the following section, where we study fixed-density systems. However, we can look at the occupation change between the examples we have seen already. Specifically, we look at the occupation for the densest case where there is a larger change in the peak resonance frequency between the non-interacting and interacting cases, Fig. (5).

In both the interacting ($R_{\mathrm{dip}}k = 0.18$) and non-interacting cases ($R_{\mathrm{dip}}k = 0$), the eigenmodes excited are similar (Fig. (10)), however in the non-interacting case a broad range of off-resonance modes are also excited while in the interacting case the excitation is concentrated around a single collective resonance. This occupation change corresponds to the peak formation in the incoherent scattering. The introduction of magnetic dipole-dipole interactions makes it easier to excite modes selectively at the chosen detuning. As the interaction strength

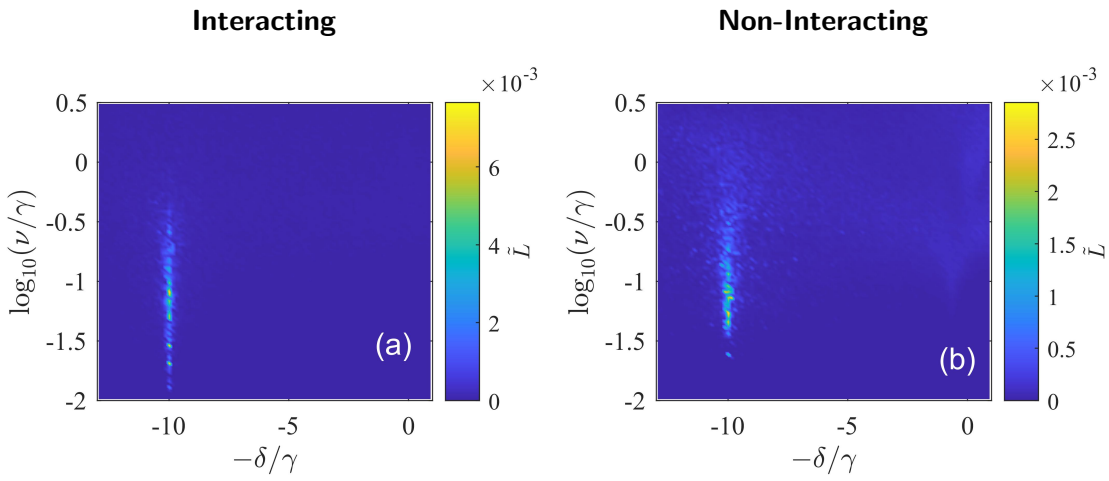

Figure 10: Comparison of eigenmode occupation between interacting and non-interacting samples of 200 atoms at large detuning -10γ. In both cases the trap has an aspect ratio of $\ell_x/\ell_z = 25, \ell_x = \ell_y$ and both samples have a peak density $\bar{\rho}_{2D}/k^2 = 3.3$. Each sample has incident on it a Gaussian beam matched to the width of that sample with polarisation $\hat{\mathbf{e}}_+$. The interaction strength in each case (a),(b) is $R_{\rm dip}\sqrt{\bar{\rho}_{2D}} = 0.18, 0$ with trap lengths $\ell_z k = 0.032, 0.18,$ and $\ell_{\rm x}{\rm k} = 0.8, 4.4$ respectively.

increases, we see the occupied modes become more subradiant as well. In the non-interacting case, Fig. (10b), many more occupied modes are not significantly subradiant or of a collective resonance far from the beam detuning. We will investigate in more detail how a change in interaction strength modifies the optical response for fixed density.

4.1.5 Transmission at fixed density with interaction strength

To better study the change in optical response with the introduction of magnetic interactions, we can modify the interaction strength while maintaining the density in terms of k. This allows any changes in response to be isolated from any change in density. Maintaining fixed density is not a trivial problem in the interacting system. An increase in confinement does increase peak density $\bar{\rho}_{2D}$ but always less than would be expected for a similar non-interacting system. This change can be predicted, but finding the appropriate confinement often leaves an error between the achieved peak density and the target peak density. For that reason, to achieve a fixed density in terms of k, after the confinement is modified, the value of k is effectively tuned to correct the error in the density. It should be noted that this does cause the thickness of the pancake in terms of k to shift slightly as a trade-off, but this change should be insignificant for a quasi-2D (or 1D) system.

The change in interaction strength has a second side-effect: it causes a change in the shape of the sample, which deviates from a Gaussian profile towards a flat uniform density distribution. This causes a second problem: the sample width does not remain constant when we keep the density constant. This means we will need to adjust the width of the Gaussian beam in lockstep with the change in the sample width. More details of exactly how this is done can be found in the Appendix. C.

In Figs. (11) and (16), the transmission and reflection for a system of 200 atoms are shown as the magnetic interaction is modified. The interaction strengths are given by the product of the interaction length and peak density, $R_{\rm dip}\sqrt{\bar{\rho}_{\rm 2D}} = [0, 0.017, 0.15, 1.6]$ [Eq. (37)], where the peak 2D density is maintained at $\bar{\rho}_{\rm 2D}/k^2 = 0.1, 1$ respectively (considered low and high density respectively). The incident beam has a circular polarisation of $\hat{\mathbf{e}}_+$ [Eq. (2)] and propagates along z perpendicular to the plane of the pancake-shaped trap. The transmission is collected over a lens $zk = 10000$ away from the sample with $\rm NA$ [Eq. (26)] of $0.2,\ 0.8$ for coherent and incoherent scattering respectively.

4.1.5.1 Optical response at low density

Firstly we consider the 'low density' case that $\bar{\rho}_{\rm 2D}/k^2 = 0.1$. The increase in interaction strength at low density (Fig. (11, 13)) has a substantial effect on the coherent response when it is large enough. For weak interaction strength, there is little modification to the optical response; however, when the interaction strength becomes larger, both the peak coherent reflection and optical depth increase. The number of atoms in the sample and the density of the sample are maintained constant here, so this is not due to an effect like what is seen in Fig. (2), instead, this change in response is due to the change in interaction strength. There is also a small reduction in the amount of incoherent transmission. This general behaviour makes sense when we consider the effect of the increase in interaction length $R_{\rm dip}$ [Eq. (37)] on the distribution of atoms in the sample. Fig. (12) shows the probability distribution of atom separations for the sample of 200 atoms as the interaction strength increases. Specifically, the distribution for pairs of nearest neighbours only and all atom pairs in the sample are shown. We

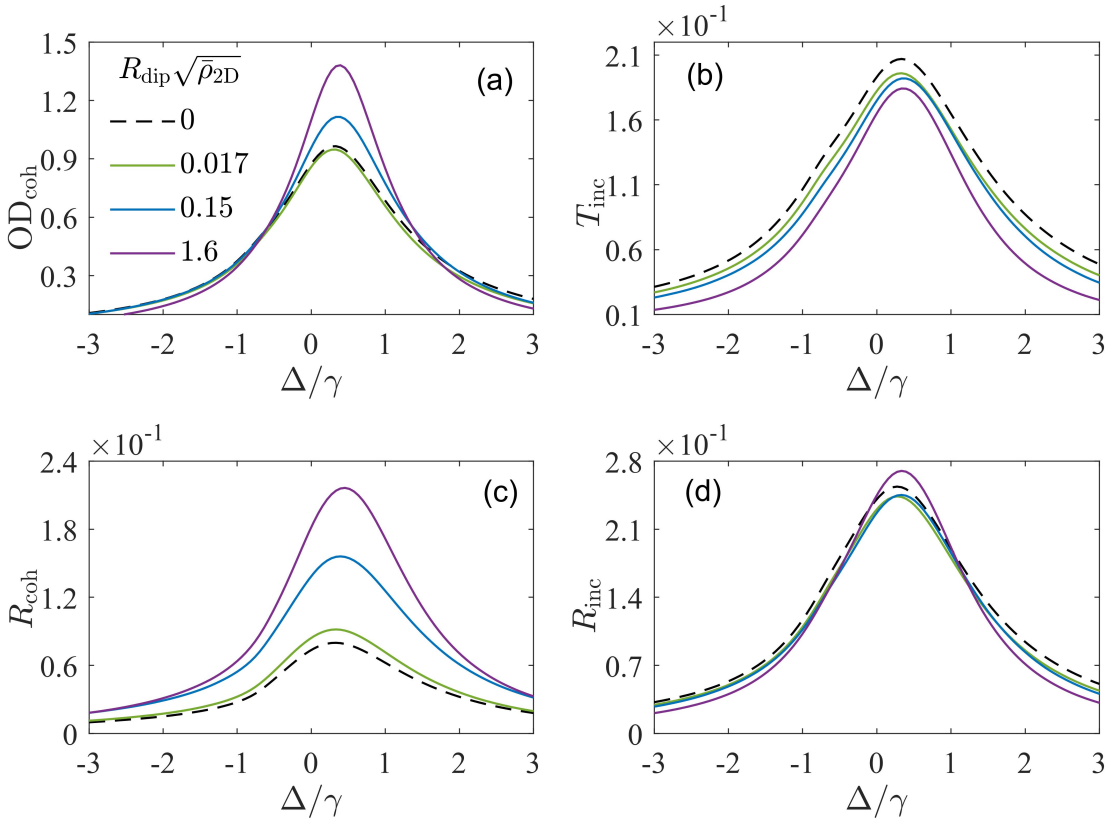

Figure 11: Optical response of 200 atoms, with no sub-level splitting, in a pancake-shaped trap at peak density $\bar{\rho}_{\rm 2D}/k^2 = 0.1$ as the interaction strength is increased. The system is illuminated with a Gaussian beam with polarisation $\hat{\mathbf{e}}_+$ [Eq. (2)] propagating normal to the trap plane. (a) Coherent transmission as an optical depth $\mathrm{OD}_{\rm coh}$ [Eq. (31)], (b) incoherent transmission $T_{\rm inc}$, (c) coherent reflection $R_{\rm coh}$ and (d) incoherent reflection $R_{\rm inc}$ [Eqs. (24)-(29)] for beam detuning from the single atom transition frequency Δ [Eq. (3)]. The sample density is increased by increasing the confinement of the sample in the x-y direction. The transmission is collected over a lens $zk = 10000$ away from the sample with a numerical aperture of $\mathrm{NA} = 0.2,\ 0.8$ for coherent and incoherent scattering, respectively. The beam waist radii are matched to the sample widths. Those widths are $W_0 k = 25, 28, 30, 31$ [Eq. (77)] $\ell_x k = 25, 10, 6, 5.3$ and $\ell_z k = 0.63, 0.54, 0.48, 0.38$ [Eq. (45)] for $R_{\rm dip} k = 0, 0.054, 0.48, 3.8$ respectively. $R_{\rm dip}\sqrt{\bar{\rho}_{\rm 2D}} = [0, 0.017, 0.15, 1.6]$

can see that as the interaction strength increases, the atoms are confined to a range of smaller possible separations. This is most clearly seen in Fig. (12 a,b). As the interaction increases, the atoms are both prevented from having small separations and very large separations. The former is due to the increased repulsion between atoms, and the increased confinement of the trapping potential causes the latter. This change in distribution reduces fluctuations between the different realisations of the sample, which would naturally decrease the scattering due

to fluctuations (incoherent scattering). The incoherent reflection shows a similar trend as the incoherent transmission except for the strongest interaction case (purple); the increase in reflection is so pronounced for this case that the two effects may be competing, resulting in the trend reversal. The increase in interactions also reduces the HWHM of the response (Fig. (13 a)), indicating that the sample is becoming more easily excited near the peak resonance but harder to excite further from it. This is in line with what we have seen previously; the presence of magnetic interactions appears to make it easier to excite certain modes, in this case modes near the single atom resonance but previously we also saw subradiant modes become easier to excite, Fig. (10).

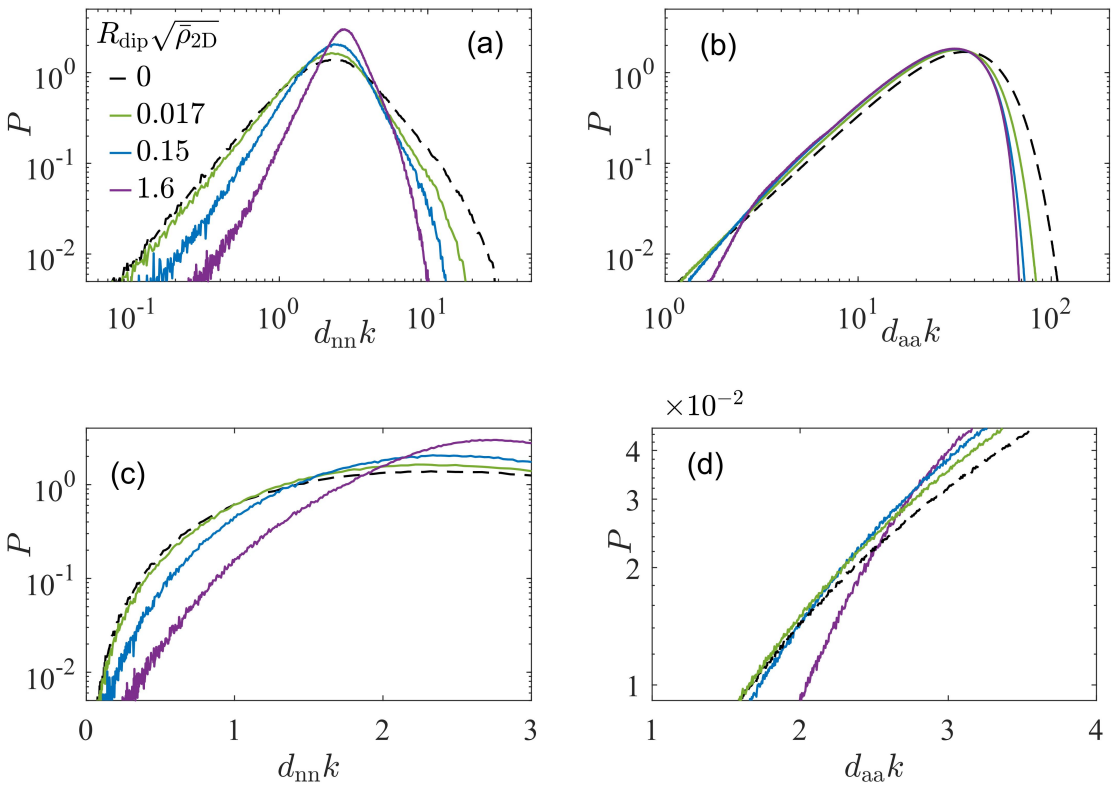

Figure 12: Atom separations for the system of 200 atoms in a pancake-shaped trap with density $\bar{\rho}_{\rm 2D}/k^2 = 0.1$ from Fig. (11). All physical parameters from Fig. (11) are the same here. (a),(c) Probability density $P(d_{\rm nn}k)$ of two atoms in the sample being nearest neighbours and having separation $d_{\rm nn}k$, with the short-range separation highlighted in (c). (b),(d) Probability density $P(d_{\rm aa}k)$ of two atoms in the sample having separation $d_{\rm aa}k$, with the short-range separations highlighted in (d). The short-range distributions (c-d) are shown on a linear scale, while the long-range plots are shown on a logarithmic distance scale (a-b). $\ell_x k = 25, 10, 6, 5.3$ and $\ell_z k = 0.63, 0.54, 0.48, 0.38$ [Eq. (45)] for $R_{\rm dip}k = 0, 0.054, 0.48, 3.8$ respectively. $R_{\rm dip}\sqrt{\bar{\rho}_{\rm 2D}} = [0, 0.017, 0.15, 1.6]$.

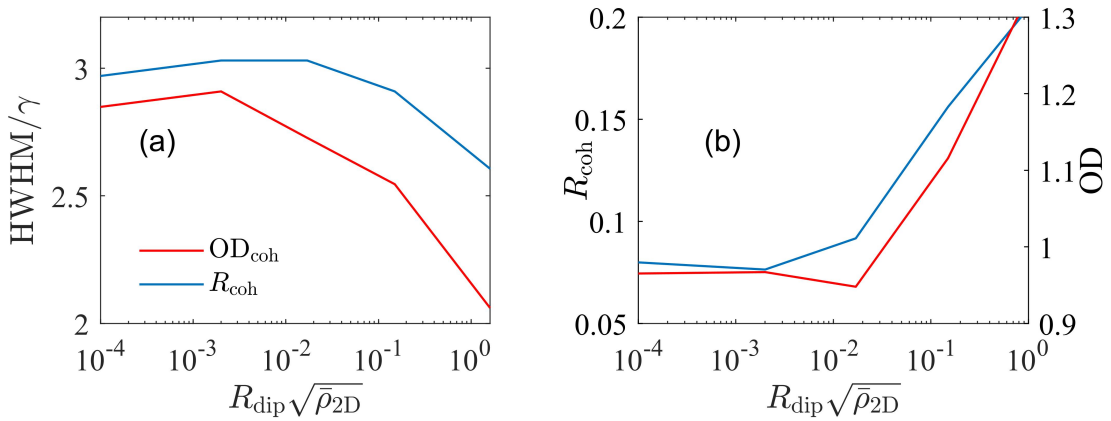

Figure 13: Change in linewidth and peak scattering of the sample of 200 atoms at peak density $\bar{\rho}_{2\mathrm{D}}/k^2 = 0.1$ from Fig. (11). All physical parameters are the same as in Fig. (11). (a) Linewidth of the coherent scattering line shape. (b) Peak coherent reflection and peak optical depth.

4.1.5.2 Eigenmodes at low density

The increase in interactions restricts the possible separations between atoms in the sample. We expect that the available eigenmodes are also similarly restricted. We can look at the availability of eigenmodes in the system by comparing the strongly interacting and non-interacting cases, Fig. (14).

At low density, the probability distribution $P(\delta, \nu)$ of available eigenmodes changes in two important ways with the introduction of strong interactions. Firstly, the distribution of collective modes becomes restricted in terms of collective resonance. Particularly, it becomes much less likely to find modes in the system with large collective resonances, especially if they are also super- or subradiant. This can be seen in the reduction of the size of the 'arms' of the distribution with increased interaction strength. This change in the distribution of available eigenmodes can explain the decrease in linewidth seen in the optical response. Few modes are available in the interacting system with de-tunings far from the most easily excited eigenmodes. This would imply that the excitation of particular modes would be reduced more quickly with detuning in the interacting case.

Secondly, how the most likely modes are distributed across collective linewidth and resonance changes between the two cases. In the non-interacting case, there is one very common mode, and the rest of the modes in the system are much less prevalent; this most prevalent mode also has the single-atom linewidth and resonance. In the strongly interacting case, the most common eigenmodes have moved. The most common modes are now slightly sub-radiant and have a shifted collective resonance; we also see a shift in this direction in the optical response. There is also a collection of modes in the red detuning region (approximately $-\delta/\gamma = -1$) that is subradiant in both cases (Fig.(15)); if this mode is excitable, we would expect to see this in the optical response. Studying the line shape of the incoherent scattering (Fig.(11)), it does deviate from a Lorentzian for a detuning that matches the collective resonance of this second mode. This deflection is not very large, indicating either that the mode is not easily excited or that it creates scattering not collected by the lens well.

Again, simply looking at the available eigenmodes is not enough to understand the optical

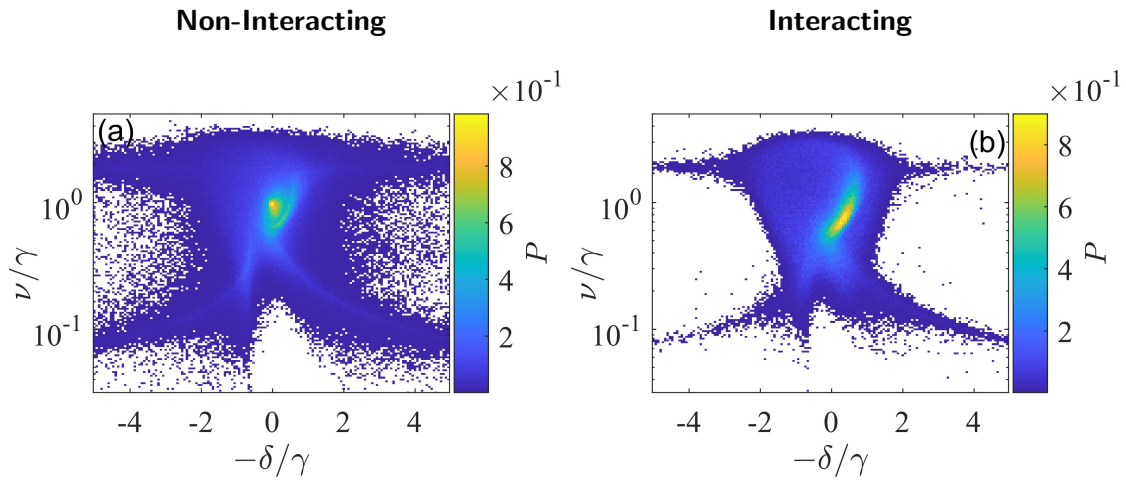

Figure 14: Distribution of available eigenmodes in a sample of 200 atoms held in a pancake-shaped trap $\ell_x/\ell_z = 40, 14$ respectively ($R_{\rm dip}\sqrt{\bar{\rho}_{\rm 2D}} = 0, 1.6$). The examples shown are selected from Fig. 11. The non-interacting and interacting cases are compared in (a,b). The sample density for both cases is $\bar{\rho}_{\rm 2D}/k^2 = 0.1$.

response; we also need to understand how the occupation of the eigenmodes changes. In Fig. (15), the occupied eigenmodes are compared for the interacting and non-interacting systems where the beam is detuned to match the peak resonance. The occupation of available modes changes with the increase in interaction strength. In the non-interacting case, there is a prominent occupation for a collective eigenmode of linewidth $\log_{10}(\nu/\gamma) = 0$, and a less occupied subradiant mode at $\log_{10}(\nu/\gamma) = -0.5$. As the interaction increases, the most highly occupied mode transitions to the subradiant mode. This change in the excited mode is likely to be the cause of the increased response with interaction strength.

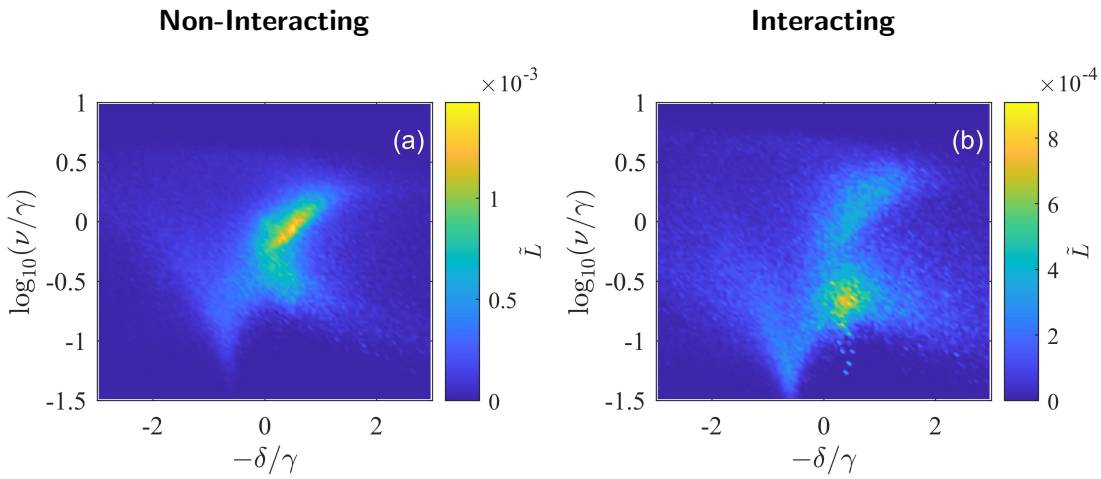

Figure 15: Binned occupation $\tilde{L}$ [Eq. (48)] of modes for the system of 200 atoms at peak density $\bar{\rho}_{2D}/k^2 = 0.1$ as in Fig. (11). The Eigenmodes are plotted by their collective linewidth ν and collective resonance shift δ [Eq. (21)]. In each plot there are 100×100 bins of height $\log_{10}(\nu/\gamma) = 0.025$, and width $\delta/\gamma = 0.06$. The systems are (a) Non-interacting and (b) with interaction strength $R_{\rm dip}\sqrt{\bar{\rho}_{2D}} = 1.6$ [Eq. (37)]. In each case, the incident Gaussian beam is detuned from the single atom resonance, $\Delta/\gamma = 0.4$ [Eq. (10)]. All physical parameters are the same as in Fig. (11) for the specific interaction strength shown here.

4.1.5.3 Optical response at high density

At higher densities Fig. (16), we see similar behaviour to the low-density case in that the modification to the optical response is minimal for weak interaction. When the interaction becomes stronger, the peak reflection and optical depth increase similarly to the low-density case. However, at high density, the change in response is only pronounced for the most strongly interacting case. For this strongest interaction case, there is also a significant increase in the linewidth in all the different channels, Fig. (17 b,d), but it is much more pronounced in the incoherent scattering. This sudden change in the optical response only for the strongest interaction appears to be the result of the system approaching crystallisation, which can most clearly be identified in Fig. (18, b). When crystallisation occurs, many local maxima appear in this curve, corresponding to the regular atom separations. The appearance of the first local maxima (seen in purple) indicates the system is nearing the crystallisation transition. The strongest interaction case curves also deviate from the others at short range. This can be seen clearly in Fig. (18, b)), whereas we approach zero separation from the right, after passing the local maxima, the probability of smaller separation quickly goes to zero. This deflection of

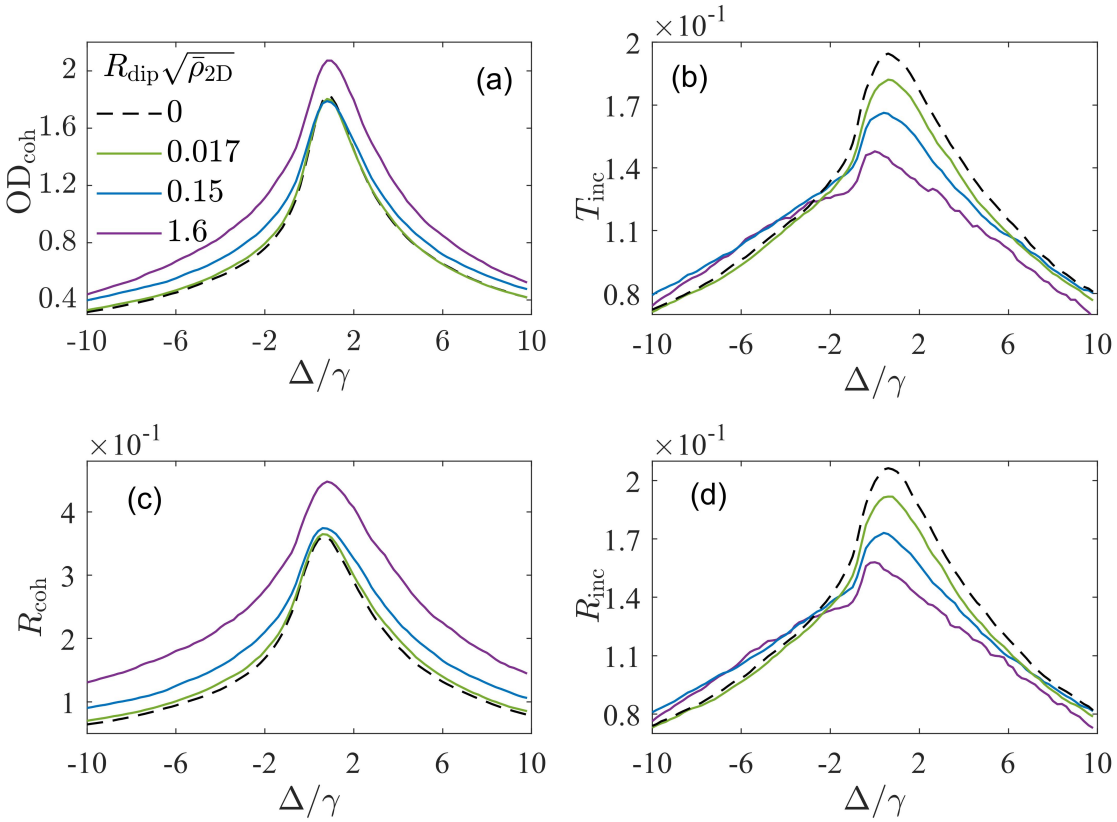

Figure 16: Optical response of 200 atom systems, with no sub-level splitting, in a pancake-shaped trap at peak density $\bar{\rho}_{\rm 2D}/k^2 = 1$ as the interaction strength is increased. The system has a Gaussian beam incident on it with polarisation $\hat{\mathbf{e}}_+$ [Eq. (2)] propagating normal to the plane of the pancake-shaped trap. (a) Coherent transmission as an $\rm OD_{coh}$ [Eq. (31)], (b) incoherent transmission $T_{\rm inc}$, (c) coherent reflection $R_{\rm coh}$ and (d) incoherent reflection $R_{\rm inc}$ [Eqs. (24)-(29)] in terms of detuning from the single atom resonance Δ [Eq. (3)]. The transmission is collected over a lens distance $zk = 10000$ away from the sample with a numerical aperture of $0.2,\ 0.8$ for coherent and incoherent scattering, respectively. The beam waist radii are matched to the sample widths. Those widths are $W_0 k = 8, 8.9, 9.6, 9.8$ [Eq. (77)]. $\ell_x k = 8.0, 3.2, 2, 1.7$ and $\ell_z k = 0.20, 0.17, 0.15, 0.16$ [Eq. (45)] for $R_{\rm dip} k = 0, 0.017, 0.15, 1.6$ [Eq. (37)] respectively.

the probability distribution at short range shows the atoms are unable to approach each other, another sign the system is near crystallising.

The optical response, particularly incoherent, is no longer Lorentzian at high density. This is true for all interaction strengths but is more pronounced for larger interaction strengths. This can be seen most clearly in Figs. (16b,d). The incoherent response with detuning becomes almost linear for larger detuning rather than Lorentzian; for the strongest interaction strength

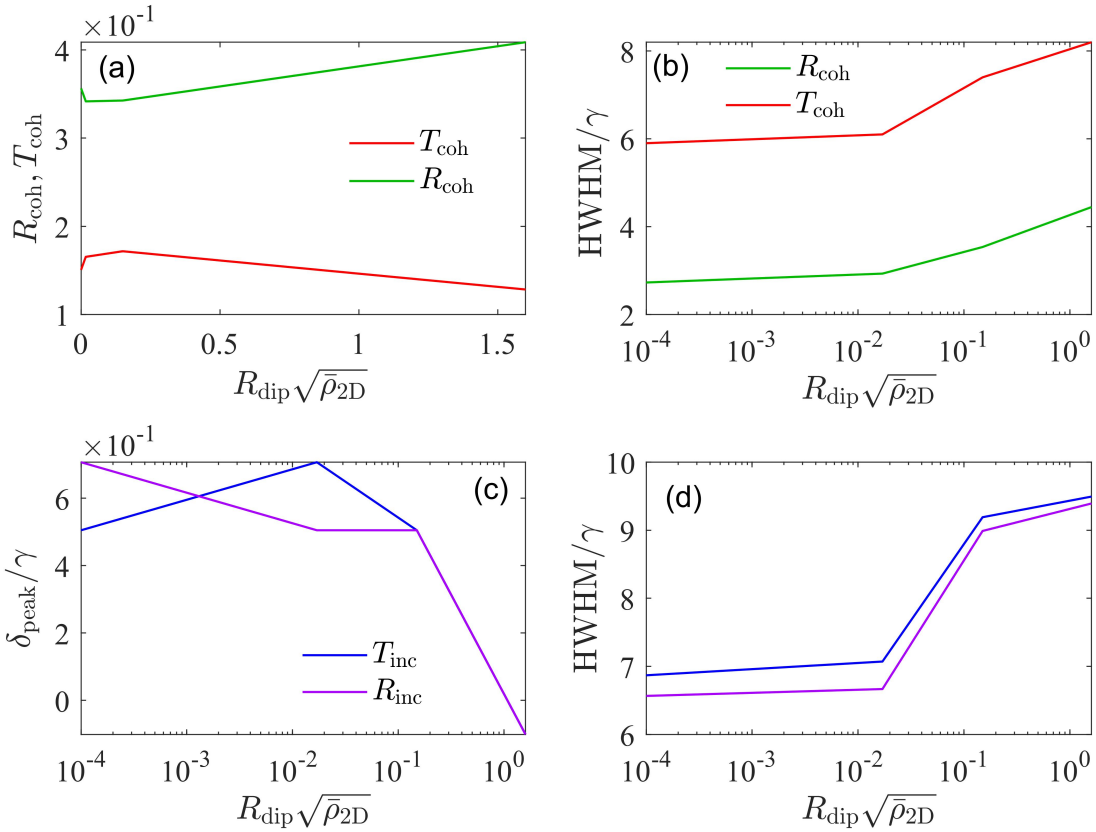

Figure 17: Line shape characteristic parameters for the system of 200 atoms at density $\bar{\rho}_{\rm 2D}/k^2 = 1$, as in Fig. (16) as the interaction strength increases in terms of density $R_{\rm dip}\sqrt{\bar{\rho}_{\rm 2D}}$. (a) Peak coherent scattering in terms of the coherent reflection and transmission, $R_{\rm coh}, T_{\rm coh}$ respectively. (b) HWHM of coherent scattering. (c) Peak resonance of the incoherent scattering $\delta_{\rm peak}$ (d) HWHM of incoherent scattering.

case, the line shape is also asymmetric. The peaks of the incoherent and coherent scattering are also now at different de-tunings from each other, which was not the case at low-density Fig. (11). The incoherent scattering shows a much broader peak than the coherent scattering, which also shifts as the interaction strength increases. The coherent scattering intensity quickly falls off for large detuning, which is not true for incoherent scattering. We will see that this broadened peak and change in peak resonance can again be explained by considering the out-of-plane polarisation of the sample.

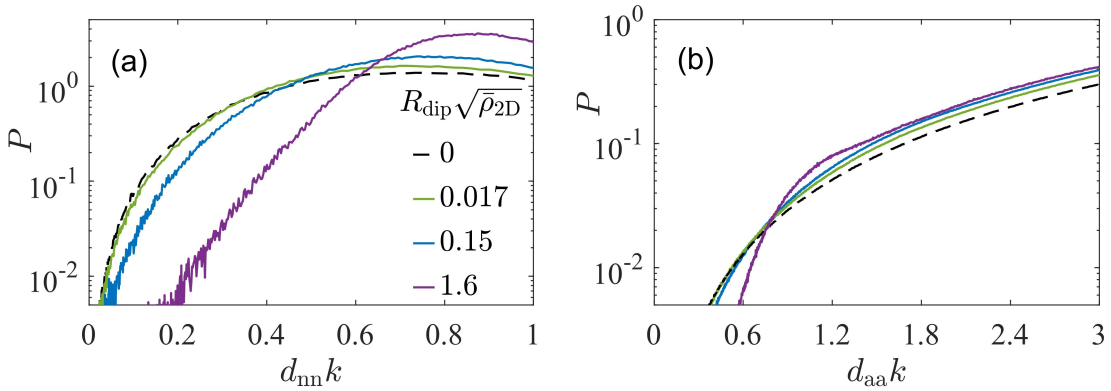

Figure 18: Atom separations for the system of 200 atoms in a pancake-shaped trap at density $\bar{\rho}_{\rm 2D}/k^2 = 1$ as in Fig. (16). All physics parameters are the same here as used in Fig. (16) for the density. (a) Probability density $P(d_{\rm nn}k)$ of two atoms in the sample being nearest neighbours and having separation $d_{\rm nn}k$. (b) Probability density $P(d_{\rm aa}k)$ of two atoms in the sample having separation $d_{\rm aa}k$. $\ell_x k = 8.0, 3.2, 2, 1.7$ and $\ell_z k = 0.20, 0.17, 0.15, 0.16$ [Eq. (45)] for $R_{\rm dip}k = 0, 0.017, 0.15, 1.6$ [Eq. (37)] respectively. The strongest interaction case seen in purple shows the start of crystallisation. The deflection of this curve (b) at short-range separations away from the other cases, as well as the formation of a local maxima around $d_{\rm nn}k = 1$, are indications of this.

4.1.5.4 Polarisation amplitudes

The transmission at high density and larger interaction strength gains a pronounced asymmetry with beam detuning from the single atom resonance. This indicates the polarisation of the atoms in the sample is asymmetric with detuning. The expected polarisation magnitude of an atom in the sample can be calculated as

$$\langle|\boldsymbol{\mathcal{P}}_q^{\rm av}|\rangle = \sum_{q=1}^{Q} \frac{|\boldsymbol{\mathcal{P}}_q^{\rm av}|}{Q} = \sum_{q=1}^{Q} \frac{1}{Q} \left| \sum_{i=1}^{N} \frac{\boldsymbol{\mathcal{P}}^{(i)+}}{N} \right| \tag{52}$$

where Q is the total number of realisations of the sample used in the ensemble average. The expected in-plane $\langle|\boldsymbol{\mathcal{P}}_{\parallel}|^{\mathrm{av}}\rangle$ and out-of-plane $\langle|\boldsymbol{\mathcal{P}}_{\perp}|^{\mathrm{av}}\rangle$ polarisation magnitudes can be found similarly, where

$$\boldsymbol{\mathcal{P}}_{\parallel}^{(i)+} = \boldsymbol{\mathcal{P}}_{x}^{(i)+} + \boldsymbol{\mathcal{P}}_{y}^{(i)+}, \quad \boldsymbol{\mathcal{P}}_{\perp}^{(i)+} = \boldsymbol{\mathcal{P}}_{z}^{(i)+}. \tag{53}$$

In-plane polarisation $\boldsymbol{\mathcal{P}}_{\parallel}^{(i)+}$ will result in scattering propagating primarily perpendicular to the trap plane; in other words, it will be detected with a lens on the optical axis. Likewise, The out-of-plane polarisation will produce scattering parallel to the trap plane, away from the optical axis. The incoherent scattering has been collected over a much larger lens with a numerical aperture $\mathrm{NA} = 0.8$. Therefore, the incoherent scattering is expected to include some scattering from out-of-plane polarisation, which would be missing in the coherent scattering.

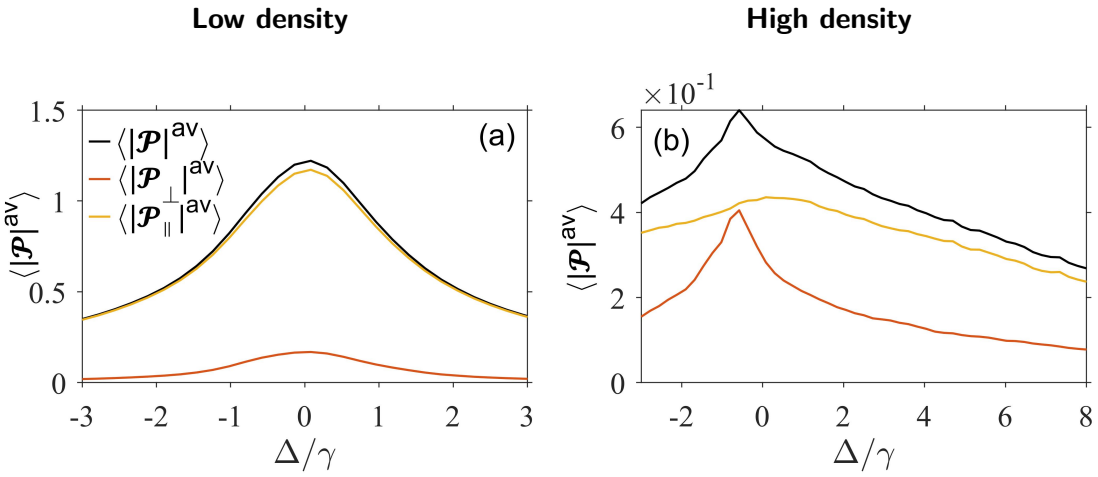

Figure 19: Expected total atomic polarisation and components $\langle|\boldsymbol{\mathcal{P}}|^{\mathrm{av}}\rangle, \langle|\boldsymbol{\mathcal{P}}_{\parallel}|^{\mathrm{av}}\rangle, \langle|\boldsymbol{\mathcal{P}}_{\perp}|^{\mathrm{av}}\rangle$ for the dense and dilute system of 200 dipoles, with no magnetic sub-level splitting, in a pancake-shaped trap illuminated with a Gaussian beam as in Fig. (11) and Fig. (16). The average of the polarisation magnitude is taken rather than the magnitude of the average polarisation. Taking the mean first causes the out-of-plane mode to appear very small or zero because the out-of-plane polarisations are often out of phase. $R_{\mathrm{dip}}\sqrt{\bar{\rho}_{\mathrm{2D}}} = 0.15$ [Eq. (37)] in all cases and all other parameters are identical as in those Fig. (11) and Fig. (16) for the $R_{\mathrm{dip}}\sqrt{\bar{\rho}_{\mathrm{2D}}} = 0.15$ cases. The plots show the total expected polarisation as an amplitude and the in-plane and out-of-plane polarisations [Eqs. (52),(53)] (where the polarisation absolute value is shown in units $\hbar\gamma/\mathcal{D}\mathcal{E}_0$) as a function of detuning from the single atom resonance Δ [Eq. (3)]. (a) Polarisation in the low density case where $\bar{\rho}_{\mathrm{2D}}/k^2 = 0.1$. (b) Polarisation in the high density case where $\bar{\rho}_{\mathrm{2D}}/k^2 = 1$.

We investigated the atomic polarisation expectation in both the in-plane and out-of-plane directions for dense and dilute systems. Figs. 19(b) and (a) show the in-plane and out-of-

plane polarizations for $\bar{\rho}_{2\mathrm{D}}/k^2 = 0.1$ and $\bar{\rho}_{2\mathrm{D}}/k^2 = 1$, where $R_{\mathrm{dip}}\sqrt{\bar{\rho}_{2\mathrm{D}}} = 0.15$ [Eq. (37)] for both systems.

The in-plane polarisation of both the low and high-density cases matches well with the coherent transmission and reflection of each. This makes sense since this polarisation will direct scattering towards the smaller 0.2 aperture lens. However, the in-plane polarisation of the high-density case does not match the incoherent transmission well. The peak in the polarisation is not at the correct detuning, and the broadness of the peak does not match the line shape. However, the out-of-plane polarisation has an asymmetric response with a peak for negative detuning. The incoherent scattering will detect some of the scattering from this out-of-plane polarisation. The incoherent scattering has a broad peak (Fig. (16)), which can then be seen to be the result of contributions from both polarisation modes. This can also be seen by considering how the peak incoherent scattering shifts as interaction strength increases. The peak resonance in the incoherent transmission shifts to match that of the out-of-plane polarisation, indicating this mode is becoming more dominant. This change in peak resonance also occurs when the system is approaching crystallisation, and we also saw significant changes in the peak scattering and HWHM. By looking at the occupation of eigenmodes in the high-density system, we can see why this change in polarisation occurs. In Fig. (20), the binned occupation of modes in the high-density case for red and zero detuning is calculated. The chosen red detuning matches the peaks in the out-of-plane polarisation at high density.

At high density, the eigenmode occupation becomes sensitive to the detuning of the incident beam from the single atom linewidth (This was also seen in the non-interacting case Fig.(10)). For no detuning (Figs. (20, b)) a slightly subradiant mode is mostly occupied, with also a broad excitation of nearby modes. For the red-detuned case -0.6γ (Figs. (20, a)), the linewidth changes substantially, becoming highly subradiant. Very few modes outside the main excited region show any excitation, indicating a shift between two different modes being excited. The excitation is also much higher for this subradiant mode. This excitation seems consistent with the peak in the out-of-plane polarisation seen in Fig. (19).

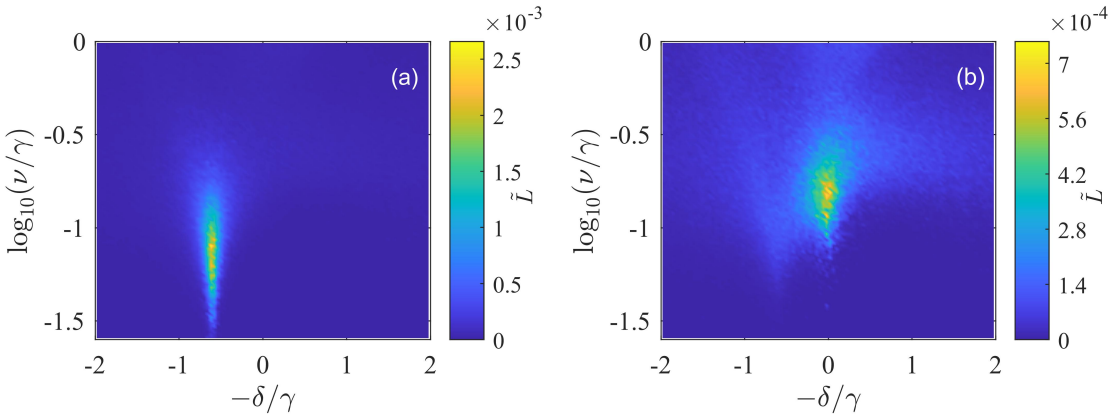

Figure 20: Occupation $\tilde{L}$ [Eq. (48)], of modes for the system of 200 atoms from Fig. (16) where peak density is $\bar{\rho}_{2D}/k^2 = 1$. The cases where $R_{dip}\sqrt{\bar{\rho}_{2D}} = 0.15$ [Eq. (37)] are used. In each plot there are 100×100 bins of height $\log_{10}(\nu/\gamma) = 0.016$, and width $\delta/\gamma = 0.04$. All physical parameters for this case are the same as in Fig. (16). The Eigenmodes are plotted by their collective linewidth ν and collective resonance shift δ [Eq. (21)]. (a), (b) Show the excitation at a detuning of the incident beam $[-0.6, 0]\gamma$ [Eq. (10)]. The excitation is sensitive to detuning and has a pronounced subradiant excitation for red detuning.

The introduction of dipole-dipole interactions at high density is then seen to allow for the excitation of multiple different modes, including subradiant modes.

4.2 Localisation of polarisation

The change in eigenmode availability and occupation with density and interaction strength changes the polarisation of the system as a whole. Here, we study in more detail how the polarisation of the samples changes in terms of the localisation of the polarisation of atoms. To do this, for each realisation of the sample, the most polarised atom in terms of magnitude $\max(|\boldsymbol{\mathcal{P}}|)$ is identified. Then, the polarisations of its five nearest neighbours are calculated. For each realisation the distribution of polarisations $|\boldsymbol{\mathcal{P}}(\varrho)|$ is then fitted to a decaying exponential of the form

$$\max(|\boldsymbol{\mathcal{P}}|)\exp(-|\boldsymbol{\varrho} - \boldsymbol{\varrho}_{\max}|/\varrho_0) \tag{54}$$

with maximum polarisation amplitude $\max(|\boldsymbol{\mathcal{P}}|)$ which is at position $\boldsymbol{\varrho}_{\max}$. ϱ_0 is a fitting parameter which describes the width of the localisation. The averages of the fitting parameters $(\langle\max(|\boldsymbol{\mathcal{P}}|)\rangle, \langle\varrho_0\rangle)$ are then calculated for the entire ensemble. From this, a decaying exponential fit is calculated, which describes the localisation of polarisations in the sample. As well as looking at the entire ensemble, we also investigate the most localised polarisations

from the sample; Fig (21) includes the 2% most localised realisations.

As the interaction length is increased across the samples, the peak polarisation increases, Fig. (21). This is more pronounced for the most localised 2%. The trend is easier to observe when looking at the fitting parameters, Fig. (22). This appears to result from the increased magnetic interactions, making it easier to excite particular eigenmodes, resulting in larger polarisations overall. As the density increases, the peak polarisation does not change monotonically; the polarisation increases slightly first before decreasing significantly for the highest density case $\bar{\rho}_{2\mathrm{D}}/k^2 = 1$. We have seen similar behaviour at high density in the peak scattering. The width of the localisation decreases with increasing density in terms of k also. This decrease could, in principle, be due to the change in length scale, so a few example samples are shown in figure Fig. (23) to show this is not the case. A clear change in localisation occurs, changing from nearly Gaussian to spiky as the density increases. These localised polarisations then are only possible when the system is sufficiently dense. There is an increase at low density in the localisation width with interaction length, but this is reduced at high density where the localisation is most pronounced. This change in localisation is likely due to the change in the distribution of atom separations. When the interaction strength is high, the most polarised atoms will naturally have more distant nearest neighbours, which would naturally increase the width of the localisation.

The localisation of the polarisation of atoms in the 200-atom system with density is seen in Fig. (23), which shows the polarisation of atoms over the system. In the low-density case, the polarisation profile is not localised and is similar to a Gaussian profile. In contrast, in the highest density case, the polarisation of the atoms is significantly localised.

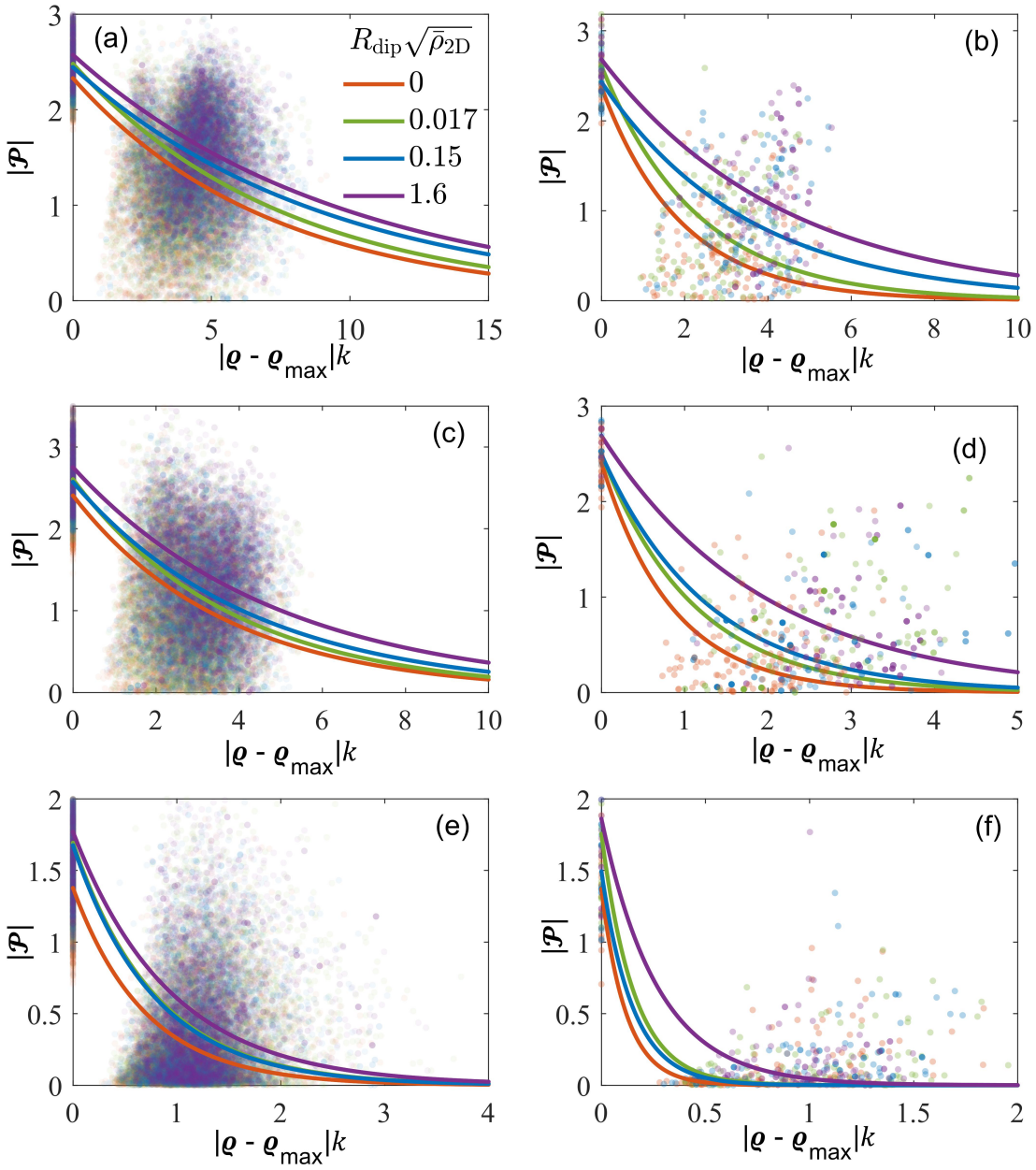

Figure 21: Localised polarisation of a 200 atom pancake-shaped sample (for 1000 realisations) with incident beam $\hat{\mathbf{e}}_+$. The atomic polarisations $|\boldsymbol{\mathcal{P}}|$ (in units $\hbar\gamma/\mathcal{D}\mathcal{E}_0$) are fit to the function [Eq. (54)] where $|\boldsymbol{\mathcal{P}}|_{\mathrm{max}}$ is the expected polarisation of the most polarised atom and $|\boldsymbol{\varrho} - \boldsymbol{\varrho}_{\mathrm{max}}|$ is the radial distance from that atom. The peak 2D density $\bar{\rho}_{2\mathrm{D}}$ in each case is (a,b) $\bar{\rho}_{2\mathrm{D}}/k^2 = 0.04$, (c,d) $\bar{\rho}_{2\mathrm{D}}/k^2 = 0.1$, and (e,f) $\bar{\rho}_{2\mathrm{D}}/k^2 = 1$. The width of the Gaussian beam is matched to the width of the sample. The cases in the left column (a,c,e) show all of the realisations sampled, whereas in the right column (b,d,f), the 2% of cases with the sharpest decay (smallest ϱ_0) are selected from (a,c,e) respectively.

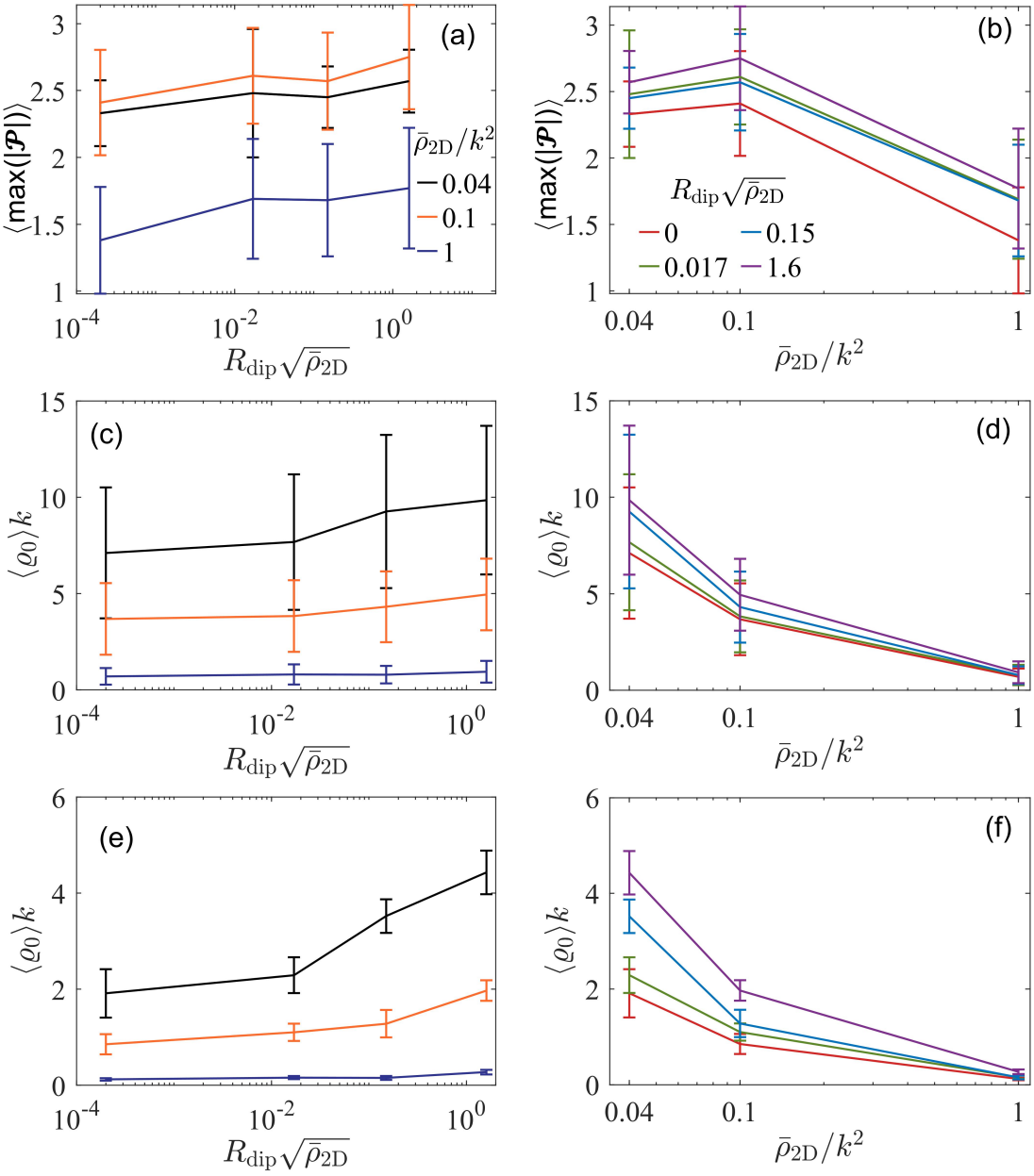

Figure 22: Peak expected localised polarisation $\langle \max(|\boldsymbol{\mathcal{P}}|)\rangle$and expected decay width $\langle \varrho_0\rangle$ as a function of interaction strength $R_{\rm dip}\sqrt{\bar{\rho}_{\rm 2D}}$ [Eq. (37)] for 200 atoms in a pancake-shaped trap with incident beam $\hat{\mathbf{e}}_+$. These are the values of the fitting parameters for the localised polarisation from Fig. (21). The error bars show the standard deviation of the fitting parameters across the 1000 realisations, where the error bars span two standard deviations. The polarisation values are in units $\hbar\gamma/\mathcal{D}\mathcal{E}_0$. (a)-(b) The expected peak polarisation and standard deviation as a function of interaction strength and density. (c)-(d) The expected distribution width and standard deviation. (e)-(f) The expected distribution width and standard deviation for the 2% most localised polarisations. The beam widths match the sample sizes in Fig. (21). (d) The values of $\langle \rho_0\rangle k = 1.28, 1.69, 1.68, 1.77$ for the density $\bar{\rho}_{\rm 2D}/k^2 = 1$, (f) The values of $\langle \rho_0\rangle k = 0.27, 0.15, 0.16, 0.199$ for the density $\bar{\rho}_{\rm 2D}/k^2 = 1$

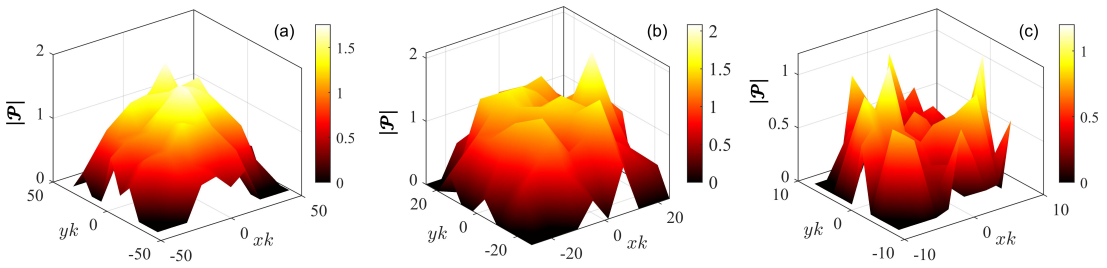

Figure 23: Polarisation localisation (in units $\hbar\gamma/\mathcal{D}\mathcal{E}_0$) in a sample of 200 atoms as the sample density in terms of beam wavenumber k is varied. The sample is illuminated with a Gaussian beam with polarisation $\hat{\mathbf{e}}_+$. The sample peak density is fixed at [(a)-(c)] $\bar{\rho}_{2\mathrm{D}}/k^2 = [0.04, 0.1, 1]$ in each case while the interaction length is given by $R_{\mathrm{dip}}\sqrt{\bar{\rho}_{2\mathrm{D}}} = 0.15$ in all cases. In each plot, a single realisation of the sample is shown.

4.3 Local Zeeman splitting

So far, in studying the optical response of dipolar systems, it has been assumed that the energy levels of the atoms are not affected by the magnetic fields of neighbouring dipoles. Here, we will study how including this local Zeeman shifting due to neighbouring dipoles changes the optical response of the system. We will consider that the $J \to 0, J \to 1, m = \pm 1$ transitions of the atoms are shifted only by the external field each atom sees. Applying an external magnetic field (such as the one used to align the magnetic dipole) would cause homogeneous shifting, while inhomogeneous shifts arise from the magnetic fields of the dipoles themselves. The sum of the two still produces inhomogeneous shifts overall. However, the detuning of the beam from the various level transitions can be written in terms of these homogeneous and inhomogeneous contributions.

$$\Delta_m^{(j)} = \omega - \omega_m^{(j)} \tag{55}$$

$$= \Delta_0 + \delta_m + \delta_m^{(j)}, \tag{56}$$

$$\delta_m = \omega_0 - \omega_m, \qquad \delta_m^{(j)} = \omega_m - \omega_m^{(j)}, \tag{57}$$

where δ_m is homogeneous contribution and $\delta_m^{(j)}$ the inhomogeneous contribution to the level shift. The inhomogeneous shifts are assumed to be due to Zeeman splitting, and therefore, the level transition frequency shift (from the $m = 0$ to $m = m$ level) is given by

$$\delta_m^{(j)} = gm\frac{\mu_B B_j}{\hbar}, \tag{58}$$

where g is the Landé g-factor, $m = \pm 1, 0$ for the 4-level atom, μ_B is the Bohr magneton, and B_j is the z-component of the total magnetic field at the jth atom in the system due to the other dipoles. We can introduce the 'coupling strength' C between the dipole fields and the local Zeeman shift so that

$$\delta_m^{(j)} = Cm \left[\frac{3z_{lj}^2}{|\mathbf{X}_{lj}|^5} - \frac{1}{|\mathbf{X}_{lj}|^3} \right], \qquad C = \frac{g\mu_B\mu_0\mu}{4\pi\hbar}. \tag{59}$$

This coupling strength can also be defined dimensionlessly in terms of various relevant ratios, see Appendix D, which may be more useful in different contexts. The sample's optical response depends on the level-splitting due to the fields of dipoles in the system. The exact distribution of the level shifts will depend on the separations between the atoms.

4.3.1 Distribution of level shifts

In Fig. (24), the distribution of shifts due to the dipole interaction of the $m = 1$ level is shown. The change in the distribution is shown as the coupling strength C is changed. Alongside this, the HWHM of each distribution is shown. Specifically, for a system of 200 atoms with $R_{\rm dip}\sqrt{\bar{\rho}_{\rm 2D}} = 0.15$. The atoms are held in a pancake-shaped trap with $\ell_x/\ell_z = 40$ [Eq. (45)]. As the coupling strength increases, the most likely shift and the linewidth increase linearly.

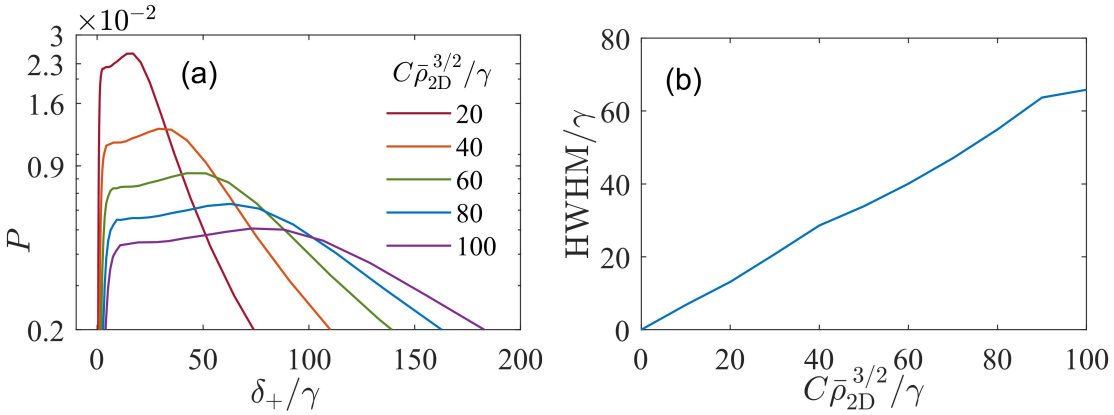

Figure 24: Probability density of frequency shifts $P(\delta_+/\gamma)$, of the $m = 1$ sub-level δ_+ [Eq. (58)] as a function of the coupling strength C [Eq. (59)] for a 200 atom sample in a pancake-shaped trap where the interaction length is $R_{\rm dip}\sqrt{\bar{\rho}_{\rm 2D}} = 0.15$ [Eq. (37)]. (a) The probability distribution of a level shifts normalised on the logarithmic scale. (b) HWHM of the distribution with coupling strength. These plots use 10000 realisations.

From Fig. (24, a), we can see that the increase in coupling strength scales the distribution of

level shifts along the x-axis, so this is to be expected. The attractive part of the potential is being neglected to match the repulsive systems studied here, so no negative shifts are seen in the distribution.

4.3.2 Optical response with local Zeeman splitting

The change in the most common level shift and the width of the level shift distribution will present themselves in the scattering as a change in the peak resonance and a change in linewidth. In Fig. (25), the transmission and reflection from the sample of 200 atoms are shown for various coupling strengths. The incident Gaussian beam has circular polarisation $\hat{\mathbf{e}}_+$ and a width matched to the sample radius. The line shape is shown relative to the peak level shift value from Fig. (24)

$$\zeta = \Delta - \bar{\delta}_{+1}, \tag{60}$$

where Δ is the beam detuning and $\bar{\delta}_{+1}$ is the peak (most likely) level shift due to local Zeeman splitting. This removes the large shift of the peak scattering, which is shown in Fig. (25, f). The lineshape of the scattering from the sample broadens substantially with an increased coupling of the transitions to the external field C, in line with the broadness of the distribution of level shifts (The HWHM of the transmission and reflection curves are shown in (e)). It should be noted that peak resonance in the optical response still shifts to the left even though the plots are adjusted to account for the most common level shift Fig. (25).

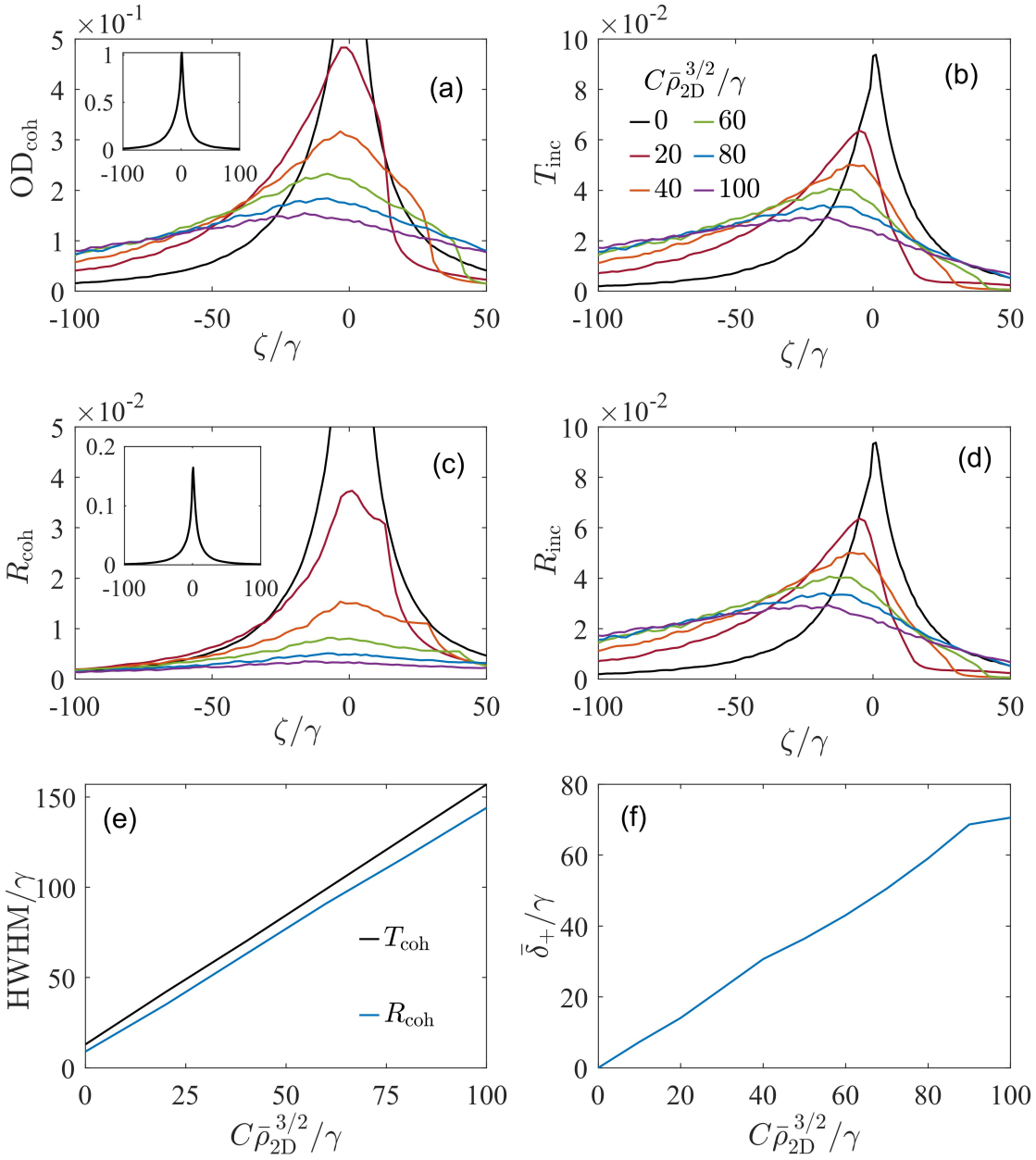

Figure 25: Optical response of a 200 atom sample in a pancake-shaped trap with included local Zeeman shifts and peak density $1k^2$. The system is in a pancake-shaped trap with a Gaussian beam incident on it with polarisation $\hat{\mathbf{e}}_+$ [Eq. (2)] propagating normal to the trap plane. (a) Coherent transmission as an optical depth $\mathrm{OD}_{\mathrm{coh}}$ [Eq. (31)], (b) incoherent transmission T_{inc}, (c) coherent reflection R_{coh} and (d) incoherent reflection R_{inc} [Eqs. (24)-(29)] with coupling strength C [Eq. (59)] in terms of frequency ζ [Eq. (60)]; the detuning from the peak (most likely) level transition frequency. The beam waist radii match the sample width, $W_0 k = 9.6$ [Eqs. (77)]. $\ell_x k = 2$, and $\ell_z k = 0.15$ for $R_{\mathrm{dip}} k = 0.15$ [Eq. (45)] respectively. The non-interacting coherent response is truncated because the peak is so high that it obscures the other curves otherwise. (e) Linewidth of each curve as a function of coupling strength. (f) Peak shift of the distribution of level shifts; each transmission curve shifts to correct for this [Eq. (60)].

The change in optical response can be explained by considering the dipole-dipole interactions that cause the local Zeeman shifts. I show the dipole-dipole potential of two dipoles in Fig. (26). The dipoles are assumed to be pointing in the z-direction and confined in a 2D plane. One of the dipoles is assumed to be at the origin, and the other is a radial distance ϱ away.

The Zeeman splitting of a particular atom will depend on the dipole-dipole potentials between it and the other atoms in the system. The exact splitting will depend on the total contributions from all of these interactions. Since each atom sees a different total potential, the exact shifts of all of the atoms in the system will have a distribution. The largest contributions to the level shifts of a particular atom will be from its nearest neighbour. Therefore, any large shifts seen in the distribution are likely due to pairs of atoms with very small separations. Since atoms can, in principle, get arbitrarily close, these shifts can get arbitrarily large. However, the repulsive force between the atoms reduces the likelihood of small separations. In the distribution of level shifts, we expect to see a long tail of larger shifts that quickly become vanishingly unlikely, which we do. Given the same distribution of nearby atoms, increasing the coupling strength C makes shifting the levels easier. Therefore, increasing the coupling will magnify all of the shifts seen in the system, which in turn scales the distribution along the x-axis, Fig. (24). Therefore, the distribution's width and the value for the most likely shift will increase linearly with the coupling strength. This is seen in the values of ζ, that each curve is shifted by, as the coupling increases, Fig. (25). The incident light is chosen to be positively circularly polarised to drive the $m = 1$ transition that is being shifted. We would expect the optical response to broaden with increased coupling since the incident field can drive this transition at frequencies further from the single-atom resonance. After accounting for the most likely shift, the shift seen in the optical response seems to be due to the presence of local Zeeman shifting at all. In the distribution of level shifts Fig. (24) we see a shoulder for small level shifts before the distribution goes to zero. This tells us that all of the atoms, regardless of the distribution of nearby atoms, will have an expected small shift in their energy levels. Atoms near the edge of the sample are good examples of this since they will be maximally separated from all other atoms in the sample but still experience a local Zeeman shift. This minimum expected shift of the energy levels also grows with the increased coupling and is not corrected by plotting the optical response against ζ. Therefore, when local Zeeman shifts are significant, we expect to

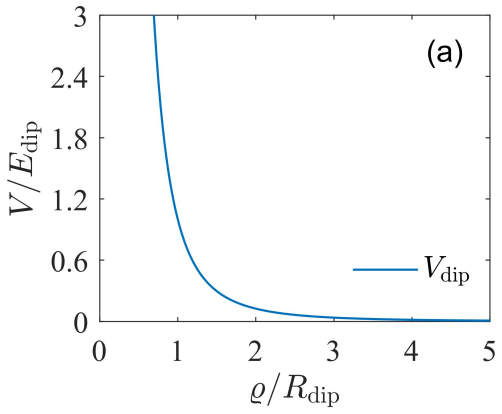

Figure 26: Dipole-dipole potential for two dipoles. The first dipole is assumed at position (0,0,0), and the second is a radial distance ϱ away. Both dipoles are assumed to be pointing in the z-direction.

see a broadening of the line shape of the sample and a shift of the peak resonance. The main contribution to this shift is due to the expected separation of nearest neighbours. Still, there is a smaller additional shift due to the long-range interactions between atoms as well.

4.4 1D weakly interacting systems

We investigate the optical response of small quasi-1D systems of atoms with dipole interactions where local zeeman shifts are ignored. In this case, the system is held in a cigar-shaped trap, and the interaction length and confinement are varied to change the distribution of atoms in the trap. The magnetic dipoles of the atoms are all aligned in the same direction perpendicular to the long direction of the trap such that they are primarily repulsive to each other. We will study a small system of 10 atoms illuminated by a Gaussian beam. In this case, we will look at two different orientations of the beam, as shown in Fig. (27). The beam can either be directed along the axis of the trap ('on-axis') or perpendicular to it ('off-axis').

4.4.1 Optical response

When studying the optical response of the 1D atom chain, the scattered power from the sample is studied rather than the reflection or transmission because, for a 1D chain, depending on the orientation, these can be very small. The coherently scattered power is given by

$$I_c = \int\int \langle \mathbf{E}_{\mathrm{S}}^{-} \rangle \cdot \langle \mathbf{E}_{\mathrm{S}}^{+} \rangle \, dA \tag{61}$$

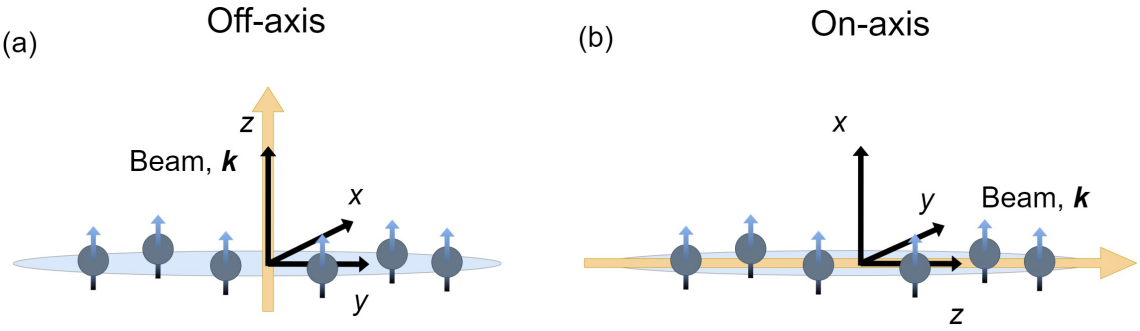

Figure 27: Schematic of the cigar-shaped atom traps and the incident Gaussian beam. The magnetic dipoles of the atoms are aligned so that the atoms are predominantly repulsive to each other. (a) The beam propagates along the z-axis along the short axis of the trap (off-axis). (b) The beam propagates along the z-axis along the long axis of the trap (on-axis).

while the incoherently scattered power is given by

$$I_\delta = \int\int \langle \delta \mathbf{E}_{\mathrm{S}}^{-} \cdot \delta \mathbf{E}_{\mathrm{S}}^{+} \rangle \, dA. \tag{62}$$

4.4.1.1 On-axis scattering

For the on-axis case, a high and low-density system are studied with 1D peak densities $\bar{\rho}_{1\mathrm{D}}/k = 0.1, 1$ respectively. Similar to the 2D systems, the change in optical response is substantial with density. The low-density case has a Lorentzian response with a peak resonance near the single atom resonance, while the high-density system has a highly asymmetric response. The optical response of the two systems can be seen in Fig. (28). In this 1D case, the Lennard-Jones potential is also included with parameters chosen to match Dy as in [45] such that the s-wave scattering length is $0.15 R_{\mathrm{dip}}$.

The optical response of the two density cases can be understood by again looking at the eigenmode occupation and atom separations. At low density, the available eigenmodes (Fig. (30)) are closely centred around the single atom resonance, similar to the 2D case. The occupation of eigenmodes is shown when the incident beam has no detuning from the single-atom resonance. This explains the Lorentzian response since, like in the 2D case, it is only possible to excite modes near the single atom resonance and linewidth because few others exist. The same modes are always being excited but less easily with greater detuning. As the interaction strength increases, there is a slight shift of the most occupied modes towards

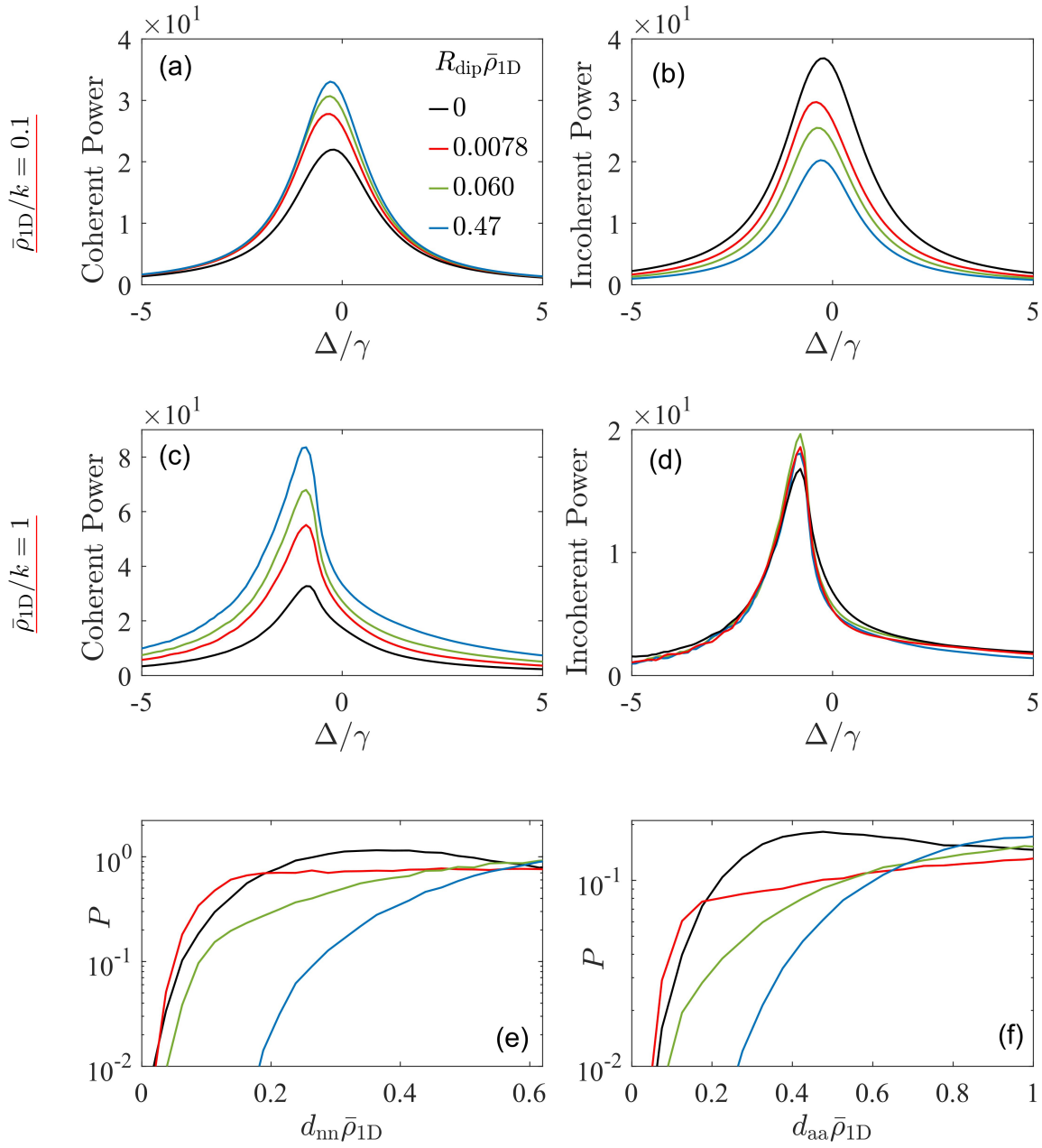

Figure 28: Optical response of a system of 10 atoms in a cigar-shaped trap with a $\hat{\mathbf{e}}_+$ polarised incident Gaussian beam of width $W_0 k = 25$ propagating parallel to the length of the cigar. The interaction strength is increased for fixed trap aspect ratio $\ell_z/\ell_x = 25$ for values $R_{dip}\bar{\rho}_{1D} = 0, 0.0078, 0.060, 0.47$. The density of the system is maintained constant in terms of k at $\bar{\rho}_{1D}/k = 0.1$, for (a),(b) while for (c),(d) $\bar{\rho}_{1D}/k = 1$. As in [45], the Lennard-Jones potential parameters fix the scattering length to match Dy; the s-wave scattering length is $0.15R_{dip}$. [(a)-(d)] Forward coherent and incoherent scattered power $I_c k^2/\mathcal{E}_0^2, I_\delta k^2/\mathcal{E}_0^2$ Eqs. [(61),(62)]. (e) Probability density $P(d_{nn}\bar{\rho}_{1D})$ of two atoms in the sample being nearest neighbours and having separation $d_{nn}\bar{\rho}_{1D}$. (f) Probability density $P(d_{aa}\bar{\rho}_{1D})$ of two atoms in the sample having separation $d_{aa}\bar{\rho}_{1D}$. In both cases, a lens on the z-axis with a numerical aperture of 0.8 collects the coherent and incoherent scattering.

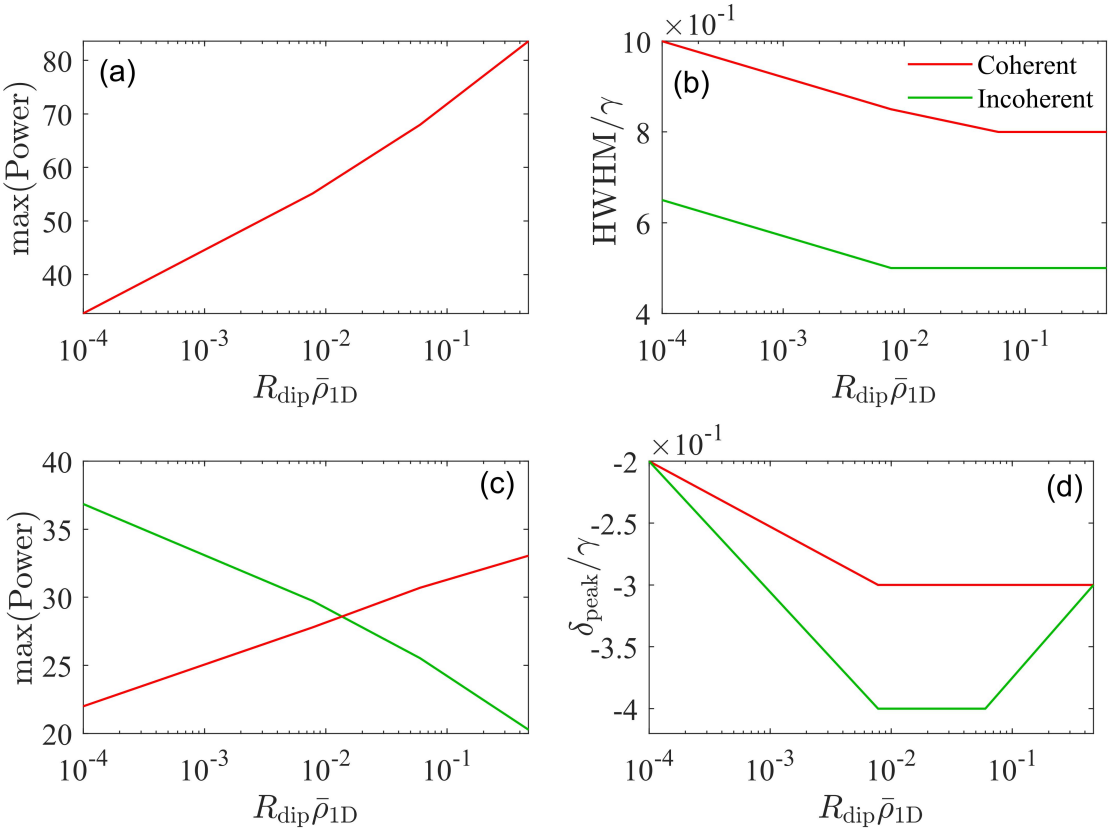

Figure 29: Lineshape parameters a ten-atom chain with an on-axis incident Gaussian beam. (a) Peak coherent scattering for $\bar{\rho}_{1\mathrm{D}}/k = 1$ (b) Coherent and incoherent line shape HWHM for $\bar{\rho}_{1\mathrm{D}}/k = 1$, (c) Peak coherent and incoherent scattering for $\bar{\rho}_{1\mathrm{D}}/k = 0.1$(d) Peak resonance δ_{peak} for $\bar{\rho}_{1\mathrm{D}}/k = 0.1$

negative detuning, most clearly seen in (c) and (d). This shift of the occupied modes is also seen in the shift of the peak scattering, Fig. (29). With increased interaction, we also see an increase in the coherent response and a decrease in the HWHM, which is again similar to the 2D case. This indicates the occupied modes are easier to excite while nearby modes are less excited for larger interactions. This increases the peak scattering on resonance with the excited modes but quickly reduces it when off-resonance. The reduction of modes with larger collective resonance shifts can also be seen with increasing interaction strength in the reduction of modes in the 'arms' of the distribution. Comparing Figs. (30 b,d), the spiral arms are almost completely removed when the interactions become larger. Comparing this change in the available eigenmodes with the probability distribution of separations of atom pairs in the samples, Fig. (28 e,f), we can see that short-range separations are suppressed when the arms are absent. It's only in the strongest interaction case (Fig. (30 d)) that the arms are removed completely, and simultaneously, the separations between nearest neighbour atoms increase significantly, shown in Fig. (28 e,f) in blue. Similar behaviour was seen in the 2D case Fig. (14) where highly shifted collected modes are suppressed for large interaction strengths also in line with an increase in inter-atom separation Fig. (12). At larger interaction strength, we also see suppression of distantly separated atom pairs; however, these do not produce the highly shifted modes. This can be seen by considering a dilute, non-interacting system. We have already seen in the 2D case that as density decreases, the available eigenmodes tend towards the single atoms linewidth and resonance Fig. (8).

The reduction in incoherent scattering is similarly due to the decrease in widely or narrowly spaced atoms. The increase in interaction strength confines the atom pairs to a smaller range of separations, which reduces the fluctuations of realisations from the ensemble average. At high density, the occupation of eigenmodes (Fig. (31)) is much more complex. Several different eigenmodes emerge at high density, which are selectively occupied with detuning. The peak resonance corresponds to a subradiant mode with a collective resonance of approximately -0.9γ. This mode becomes highly occupied at this detuning, with very few neighbouring modes being excited. However, when no magnetic interactions exist, the ability to excite this subradiant mode is significantly reduced in favour of exciting other nearby modes. Similarly, near the single atom resonance, several different modes become occupied when the interaction strength is high but are not excited when these interactions are removed. When the magnetic

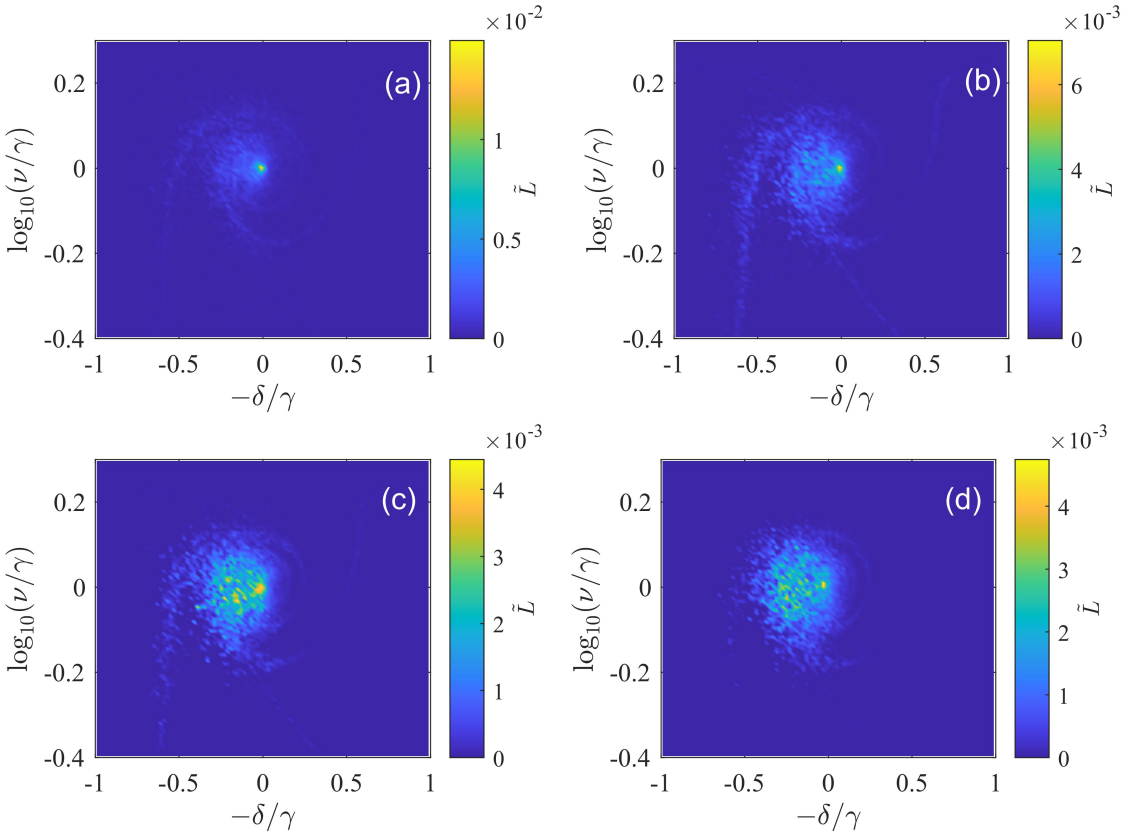

Figure 30: Eigenmode occupation $\tilde{L}$ of a system of 10 atoms in a cigar-shaped trap, $\ell_z/\ell_x = 25$, with an on-axis incident beam, for density $\bar{\rho}_{1\mathrm{D}}/k = 0.1$. Each mode is plotted in the plane where δ/γ (Eq. (21)) is the mode collective resonance, and ν/γ is the collective linewidth. The incident Gaussian beam has circular polarisation $\hat{\mathbf{e}}_+$ with width $W_0 k = 25$. The beam is tuned to the single-atom resonance in each case. The interaction strength in each case is given by $R_{\mathrm{dip}}\bar{\rho}_{1D} =$ (a) 0, (b) 0.0078, (c) 0.060 and (d)0.47

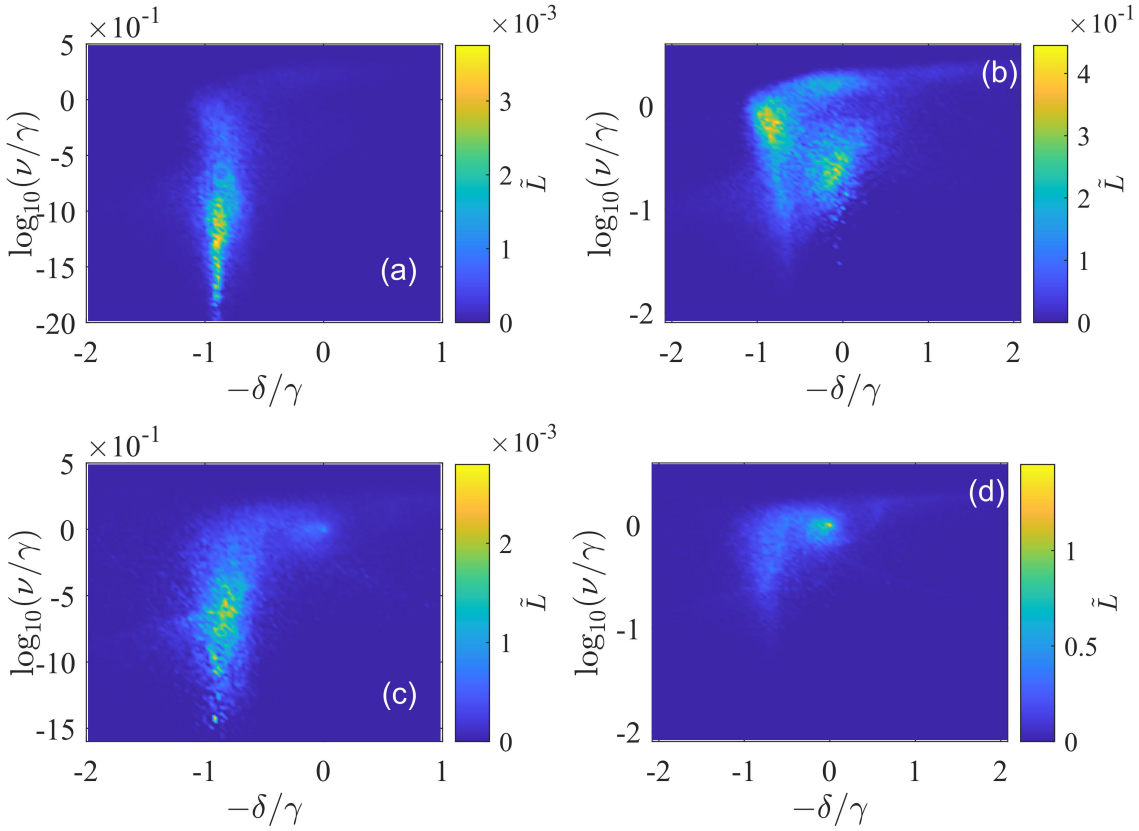

Figure 31: Eigenmode occupation of a system of 10 atoms in a cigar-shaped trap with on-axis incident beam, for density $\bar{\rho}_{1\mathrm{D}}/k = 1$. Each mode is plotted in the plane where δ/γ (Eq. (21)) is the mode collective resonance, and ν/γ is the collective linewidth. The incident Gaussian beam a has circular polarisation $\hat{\mathbf{e}}_+$ with width $W_0 k = 25$. The beam is on resonance with the single atom resonance in each case. $\ell_z/\ell_x = 25$. (a,c) $\delta/\gamma = -0.9$, (b,d) $\delta/\gamma = -0.9$. (a,b) $R_{\mathrm{dip}}\bar{\rho}_{1D} = 0.47$, (b,d) $R_{\mathrm{dip}}\bar{\rho}_{1D} = 0$.

interactions are significant, then it is possible to excite eigenmodes that are hard to occupy otherwise.

4.4.1.2 Off-axis scattering

We can also study the scattering of the 1D chain when the incident light is incident perpendicular to the length of the chain. This orientation allows for different eigenmodes to be excited, particularly those with electric dipoles polarised along the axis of the cigar. The scattering in the off-axis case is markedly different to the on-axis case. As we have seen before, the coherent scattering generally increases with interaction strength. The strongest interaction case (for which crystallisation is almost occurring) has a dramatically different line shape to

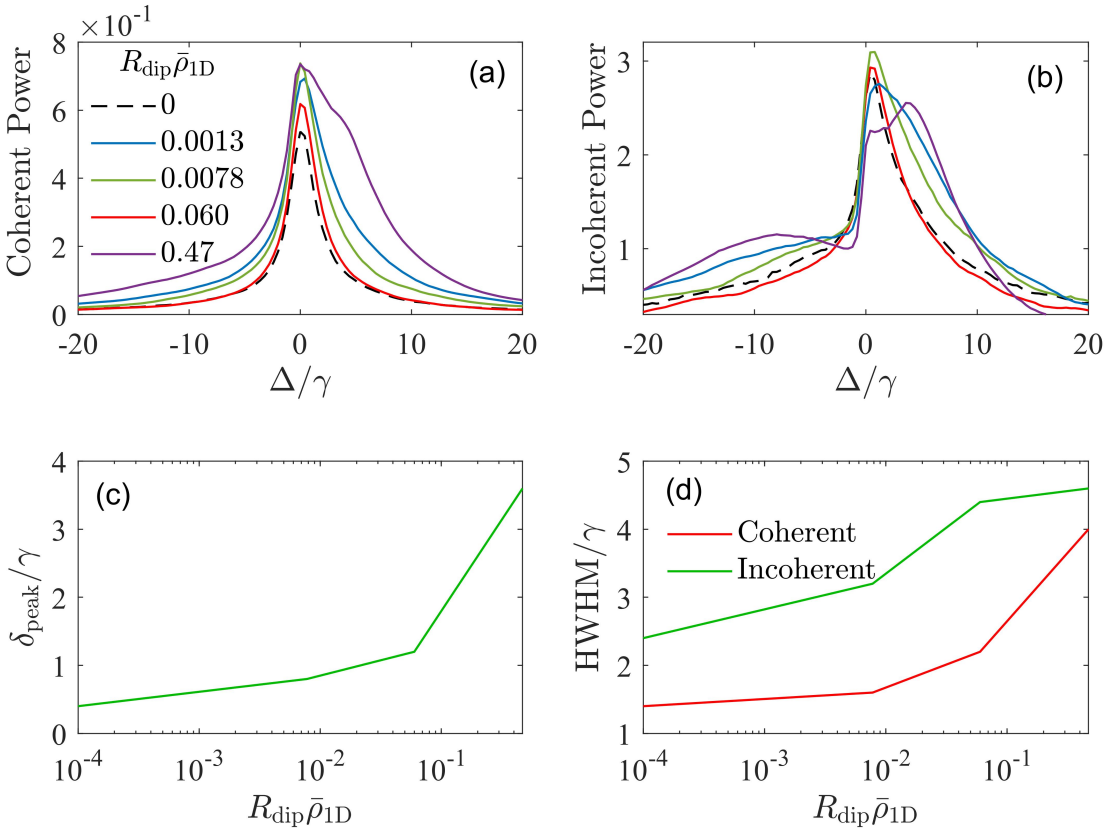

Figure 32: Optical response of a system of 10 atoms in a cigar-shaped trap. A Gaussian beam propagating perpendicular to the length of the cigar, with polarisation $\hat{\mathbf{e}}_+$ illuminates the sample. The width of the beam in each case is matched to the size of the sample, $W_0 k = 5.7, 5.6, 6.5, 6.5, 6.3$ respectively. The interaction strength is increased for fixed trap aspect ratio $\ell_y/\ell_x = 25$ for values $R_{\rm dip}\bar{\rho}_{\rm 1D} = 0, 0.0013, 0.0078, 0.060, 0.47$. The density of the system is maintained constant in terms of k at $\bar{\rho}_{\rm 1D}/k = 1$. The Lennard-Jones potential parameters set scattering length to match Dy as in [45] such that the s-wave scattering length is $0.15R_{\rm dip}$. (a),(b) Forward coherent and incoherent scattered intensities I_c, I_δ Eqs. [(61),(62)]. The coherent and incoherent scattering is detected with a lens on the z-axis with a numerical aperture of 0.2 and 0.8, respectively.

the preceding cases. Notably, a shoulder appears in the coherent scattering, and three peaks are present in the incoherent scattering. This indicates the semi-regular structure allows for the excitation of several different eigenmodes most easily excited at different resonant frequencies. Looking at the difference between the incoherent and coherent scattering, we see the peak in the red detuning region is absent from the coherent scattering. This indicates that the detected polarisation mostly directs scattering away from the collecting lens. The incoherent scattering is collected over a much larger 0.8 aperture lens, which will collect some of this scattering but not the smaller 0.2 aperture lens. We should also expect that the second blue detuning mode is perpendicular to the optical axis since it is seen in both cases. The line shape broadens with increased magnetic interaction, explained by the increased availability of modes with different collective resonant frequencies.

Fig. (33) shows the occupied eigenmodes of the 1D chain of 10 atoms. (a) and (b) compare the occupied eigenmodes between a non-interacting and interacting system while the incident Gaussian beam is tuned to the single atom resonance. When the interaction strength increases, the occupied modes shift from being mostly near the single atom linewidth to becoming slightly subradiant. This subradiant mode is not well excited in this case; instead, a central mode near the single atom resonance and linewidth is primarily excited regardless of interaction strength. This consistent occupation across interaction strength explains why the change in optical response (for the central peak) remains. The most interesting change is that there are excitable superradiant and subradiant modes at de-tunings corresponding to the other two peaks in the incoherent scattering, Fig. (33c,d). The secondary peaks appear to result from the superradiant modes, not the subradiant modes. In these cases, the total occupation is low for the subradiant modes. The excited subradiant modes are also sensitive to detuning, while the superradiant modes are not; they would not produce the kind of broad peak seen.

4.4.2 Summary of results for weak magnetic dipole interactions

Introducing magnetic dipole-dipole interactions into dense systems of atoms (in terms of incident light length scale k) modifies the system's cooperative optical response by modifying the distribution of atom positions. Increasing the magnetic dipole interactions between atoms for fixed trap parameters modifies the density profile. The sample size increases in width while

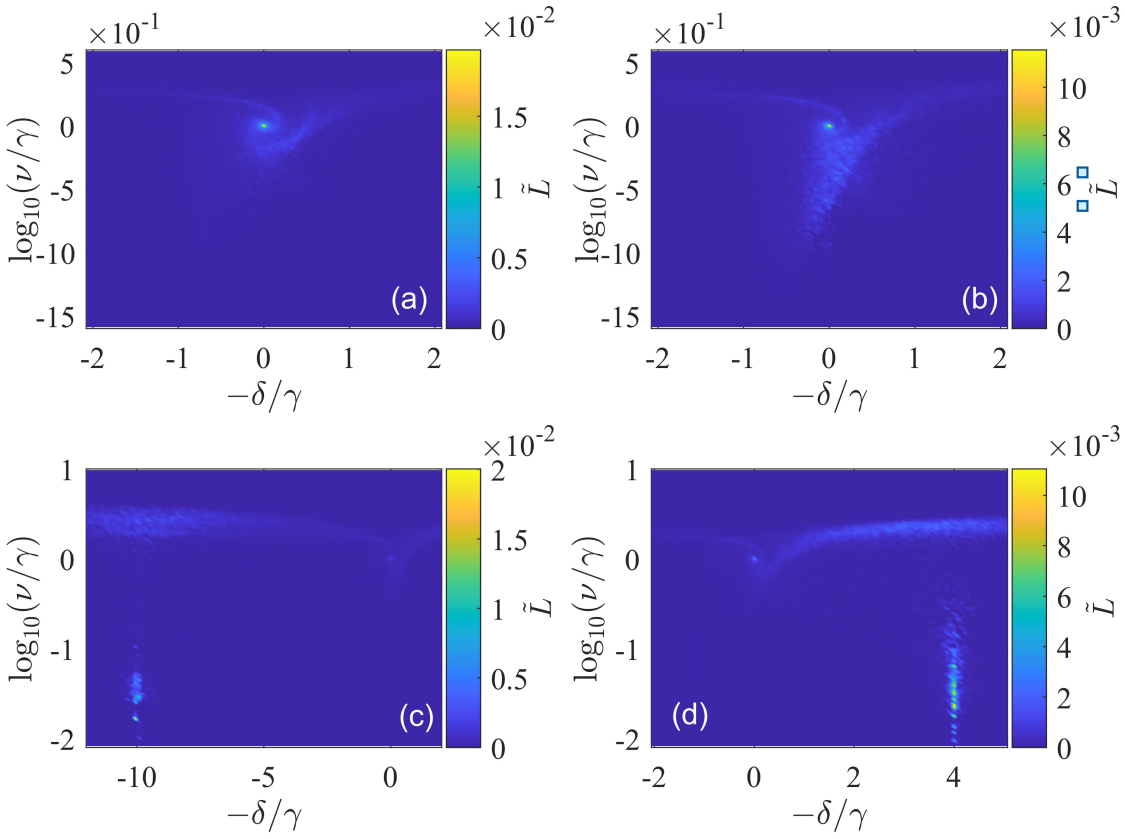

Figure 33: Eigenmode occupation for a system of 10 atoms held in a cigar-shaped trap, $\ell_y/\ell_x = 25$ with peak density $\bar{\rho}_{1\mathrm{D}}/k = 1$ for incident off-axis gaussian beam with polarisation $\hat{\mathbf{e}}_+$. (a) Non-interacting system for zero detuning. (b)-(d) Interacting systems where $R_{\mathrm{dip}}\bar{\rho}_{1\mathrm{D}} = 0.47$ and for (b) zero detuning, (c) -10γ and (d) 4γ. Parameters and systems used match those of Fig. (32), and the chosen detuning values match features of the curves in (a) and (b).

the peak density decreases. Because the density modifies the collective response in the absence of magnetic interactions, we consider modifying the magnetic interactions at constant density in terms of k. This is achieved by modifying the trapping parameters in tandem with the increasing magnetic interactions such that the sample peak density is maintained constant. In this case, we find the distribution of atom separations narrows. There is a reduction in both closely spaced and distantly spaced atoms; the density profile tends towards being a uniform distribution.

We also studied the available eigenmodes in these systems. It was found that highly super- and subradiant modes with large collective resonance shifts result from closely spaced pairs of atoms in the ensemble. Therefore, for fixed peak density, these super- and subradiant modes are generally suppressed with increasing magnetic interactions. Simultaneously, since extremely closely and distantly spaced atom pairs are suppressed, the ensemble's realisations become more similar to each other. This results in the enhanced occupation of modes in the ensemble. We see this feature in the low-density optical response where the peak coherent reflection increases with magnetic interaction strength (Fig. (28)). We similarly see a decrease in incoherent transmission and reflection, which implies smaller fluctuations between the realisations. Finally, we also see a decrease in the HWHM of the optical response lineshape. This also appears to be due to the reduction in realisation fluctuations. There are simply fewer modes to occupy in the ensemble that have collective resonances away from the single atom resonance. We should then expect that the scattering at large de-tunings would decrease with increased magnetic interactions at low density.

These highly shifted super- and sub-radiant modes are more prominent at high density, even for strong interactions. In this case, the increase in magnetic interactions produces an increase in coherent reflection and a decrease in incoherent scattering, as in the low-density case. In the 2D system specifically, we can also see an increase in the HWHM of the lineshape. This appears to be due to the increased ease with which highly shifted modes (that have not been suppressed) can be excited at high interaction strength.

4.5 Crystal Structures

Introducing repulsive dipole-dipole interactions to the collection of atoms under the correct conditions leads to crystal structure formation. So far, we have studied non-crystallised systems, but here, we study crystallised systems in more detail. When the interaction length is sufficiently large (or the density sufficiently high), the positions of the individual atoms become localised and regularly spaced. This crystallisation occurs in both 1D and 2D systems.

4.5.1 1D crystallisation

The crystallisation of a 1D atom chain is seen in (Fig. (34)). For a system of 10 atoms

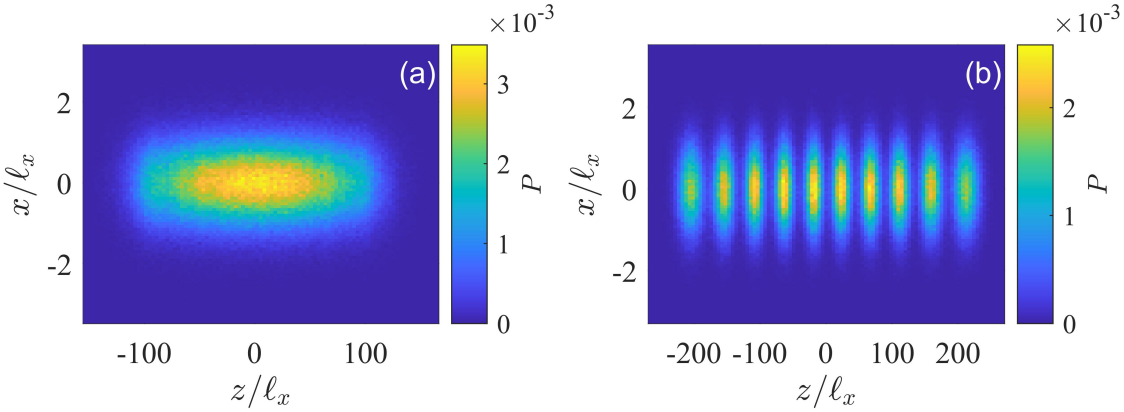

Figure 34: Normalised probability density $P(z,x)$ of an atom at position (z,x) for a collection of 10 atoms in a cigar trap ($\ell_z/\ell_x = 25$, $\ell_x = \ell_y$) for magnetic DD interactions (a) $R_{\rm dip}\bar{\rho}_{1D} \simeq 0.058$, $R_{\rm dip}/\ell_x = 1$ (b) $R_{\rm dip}\bar{\rho}_{1D} \simeq 2.5$, $R_{\rm dip}/\ell_x = 100$

in a cigar-shaped trap, the interaction length is increased while the confinement is kept constant with a ratio between the trap lengths of $\ell_z/\ell_x = 25$. For low interaction strength, the density profile of the sample retains the cigar shape of the trap itself, although it may be significantly modified from the non-interacting Gaussian distribution. When the interaction strength increases sufficiently, the atom positions within the sample become localised. There are exactly N localised regions in the probability density (Fig. (34, b)), one for each atom in the system.

The transition to the crystallised system can be identified through the separations between

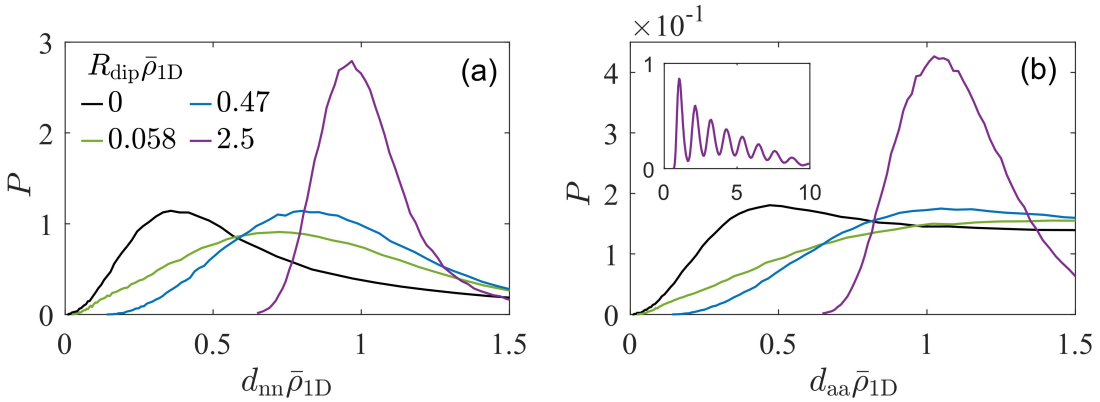

Figure 35: Atom separations of 10 atoms in a cigar-shaped trap ($\ell_z/\ell_x = 25$, $\ell_x = \ell_y$) for dipole interaction strength $R_{\rm dip}/\ell_x = 0, 1, 10, 100$. Probability distributions of (a) nearest neighbour pair $d_{\rm nn}\bar{\rho}_{1D}$ and (b) all-pair seperations $d_{\rm aa}\bar{\rho}_{1D}$. The inset shows the formation of local minima and maxima for the crystallised system. The interaction potential includes the fitted Lennard-Jones potential, so the scattering length is $0.15R_{\rm dip}$.

atoms. In Fig. (35) the probability $P(d\bar{\rho}_{\rm 1D})$ of finding a pair of atoms in the 1D sample being separated by a distance $d\bar{\rho}_{\rm 1D}$ is shown. The distribution of atom separations are shown for several different interaction strengths but fixed trap ratio, $\ell_z/\ell_x = 25$. In Fig. (35), the probability of finding any pair of atoms to have inter-particle distance $d_{\rm aa}$ is shown as well as the probability of pairs of nearest neighbour atoms being separated by distance $d_{\rm nn}$. With the increase in interaction strength, we can see that the separation between nearest neighbour atom pairs increases, as we have seen before. Short separations are prevented while the most likely atom separation increases. When the interaction strength becomes sufficiently large, there is a large increase in the peak value of the separation probability and a significant narrowing of the distribution; signalling crystallisation has occurred. However, the transition to crystallisation is easier to identify from $P(d_{\rm aa}\bar{\rho}_{\rm 1D})$. The shape of the distribution changes when crystallisation occurs, forming multiple local maxima and minima. This formation of local maxima shows the localisation of the atom positions in the sample, which have regular spacings from each other. This can be seen clearly in Fig. (35, b) in the purple curve.

4.5.2 2D crystallisation

In the 2D case, similar crystallisation emerges when the interaction strength is sufficiently high. Fig. (36) shows the probability distributions of atom pair separations for 2D systems with interaction strength. The behaviour is similar to the 1D case; As the interaction strength

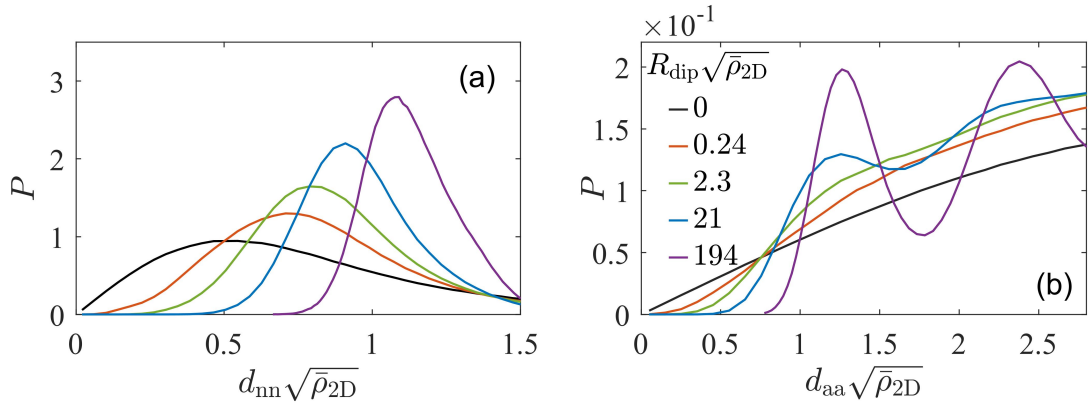

Figure 36: Atom separations of 50 atoms in a pancake-shaped trap ($\ell_x/\ell_z = 168, 53, 36, 25, 17$) with interaction strength. (a) Probability distributions of (a) nearest-neighbour atom pairs $d_{\mathrm{nn}}\bar{\rho}_{1\mathrm{D}}$ and (b) all-atom pair separations $d_{\mathrm{aa}}\bar{\rho}_{1\mathrm{D}}$. The formation of minima and maxima in the all-atom pair distribution shows the emergence of crystallisation.

increases, the expected nearest neighbour separation increases and the all-atoms separation distribution forms regular maxima and minima. In Fig. (37), I show the probability density of various 50-atom systems with interaction strength. As the interaction strength increases, the density profile of the sample first flattens out, and then concentric rings form before the system forms into a semi-regular lattice.

Comparing Fig. (37) with Fig. (34), we can see that in the 1D case, there are ten regions of high density, one corresponding to each atom in the trap. In the 2D system, we have only approximately 34 high-density regions rather than the expected 50, showing that multiple atoms must occupy some regions. We investigate the number density of atoms in each region to see if the regions in the 2D case contain integer or non-integer numbers of atoms.

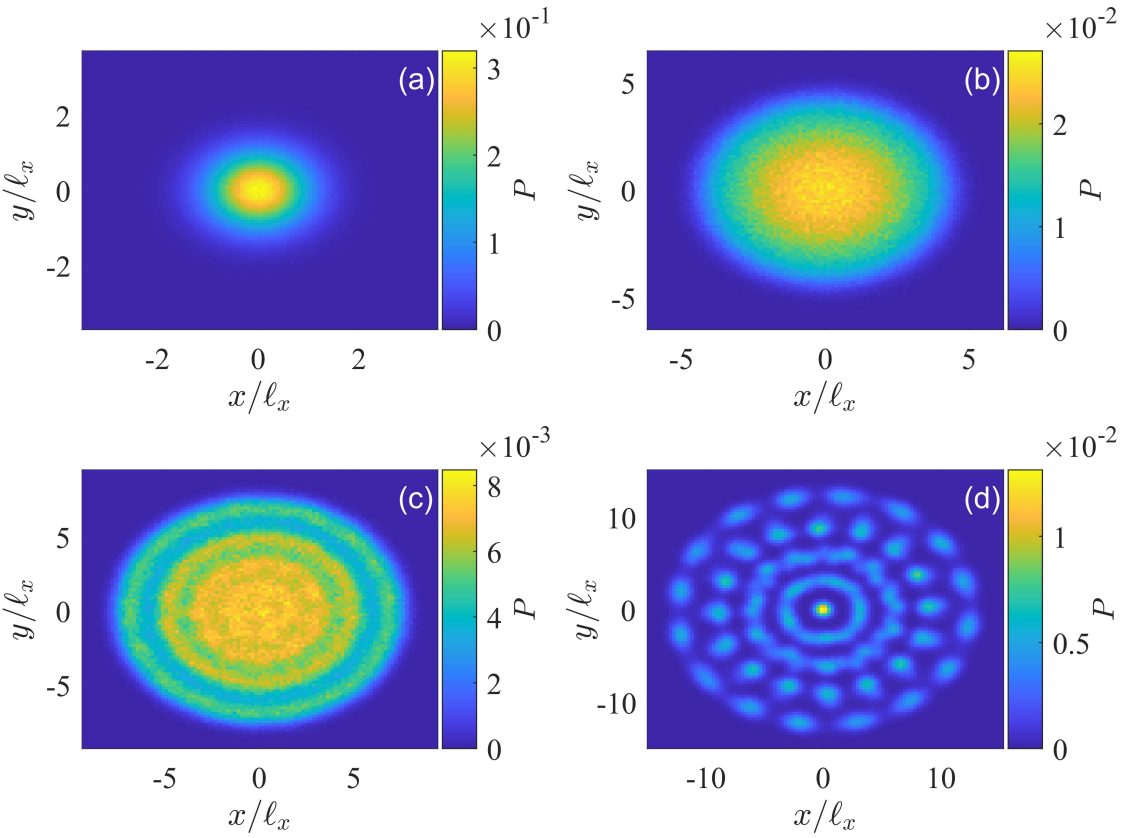

Figure 37: Normalised density profiles $P(x, y)$ for a system of 50 atoms held in a symmetric pancake-shaped trap ($\ell_x/\ell_z = 30, 30, 25, 30$) with interaction strengths (a) $R_{\rm dip}\sqrt{\tilde{\rho}_{\rm 2D}} = 0$, (b) 0.375, (c) 21 and (d) 120 in order of increasing density.

4.5.2.1 Occupation of crystal sites

If we define the wavefunction of the entire systems as a sum of localised sites as

$$\psi(\mathbf{r}) = \sum_j \phi_j(\mathbf{r}) a_j \tag{63}$$

where

$$\int \phi_j(\mathbf{r})^* \phi_j(\mathbf{r}) = 1, \tag{64}$$

then, we can calculate the expectation value for the number of atoms in each localised site as

$$N_j = \langle a_j^\dagger a_j \rangle \,. \tag{65}$$

Similarly, we can calculate the number density as

$$n_j = \langle a_j^\dagger a_j \rangle / V_j, \tag{66}$$

where V_j is the volume of the j'th site.

The form of each localised site is not known analytically, so instead, to identify the region of each localisation, the probability density of the atoms is mapped to either 0 or 1 using the function.

$$C = \begin{cases} 1 & \text{if } \rho_{\mathrm{2D}} \geq \rho_{\mathrm{cut}} \\ 0 & \text{if } \rho_{\mathrm{2D}} < \rho_{\mathrm{cut}} \end{cases} \tag{67}$$

where the cut-off density ρ_{cut} is chosen so that the isolated regions do not overlap where possible. The choice of cut-off changes the regions identified as individual sites, so the cut-off

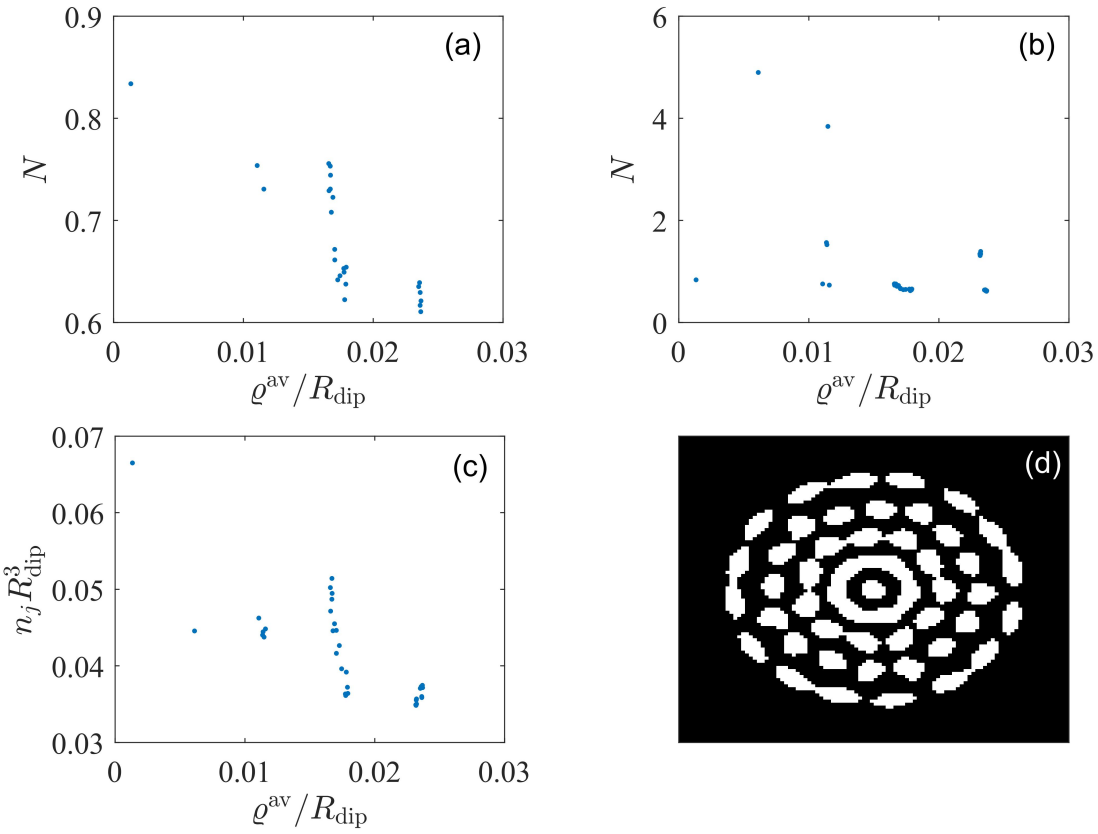

Figure 38: The expected occupation of localised regions in the crystal structure wavefunction. (a)-(b) Show the occupation of each region in terms of radial distance (of its average position) from the centre of the trap ϱ^{av}. An expanded view is shown in (b), whereas (a) cuts off the results for values above 0.9. (c) The number density of each selected region as a function of radial distance from the trap's centre and (d) selection regions used to calculate the expected occupation.

needs to be chosen carefully. Using a smaller cut-off creates larger selection regions and vice

versa. If the cut-off is too low, it causes sites to overlap even when the localisations could be resolved. Using a larger cut-off shrinks the regions, resolving different sites but at the cost of shrinking the selected areas, artificially reducing the value of the occupancy calculated. Therefore, the choice of cut-off is a compromise between resolving sites and undercounting occupations. In Fig. (38), the selected regions based on the chosen cut-off value for the density ρ_{cut} are shown. In this case, the occupation of most of the sites is lower than but near one.

The occupation across larger sites is not a continuous spectrum; the values cluster near integer values. This indicates each site contains nearly an integer number of atoms, but the method for selecting them cannot properly isolate each state. To confirm this, we can also calculate the number density of each of the localisations. The number density is not susceptible in the same way to a poor selection of region for each site. The number density of each site is much more consistent across the sample even though the occupation changes significantly. This indicates that the change in occupation is due mainly to how the region is selected and its size. Sometimes, the chosen region ideally should be resolved as two or three sites, which is reflected in the occupation. If, instead, the system contained single sites that contained multiple atoms, we would expect them to have a higher number density simultaneously. However, it should be noted there is an increase in number density in the central region and a decrease towards the outside. This is in line with the increase in the trapping potential towards the outside of the trap. Therefore, in 2D crystallised systems, most sites are expected to contain a single atom but with a bias away from the edge of the trap. These crystallised systems then contain atoms with regular separation distances from each other rather than any pairs very close together. Example realisations of such a system can be seen in Fig. (39). Even though the positions of atoms in each realisation fluctuate away from the ensemble average, no pairs of atoms overlap because of the strong repulsion between them.

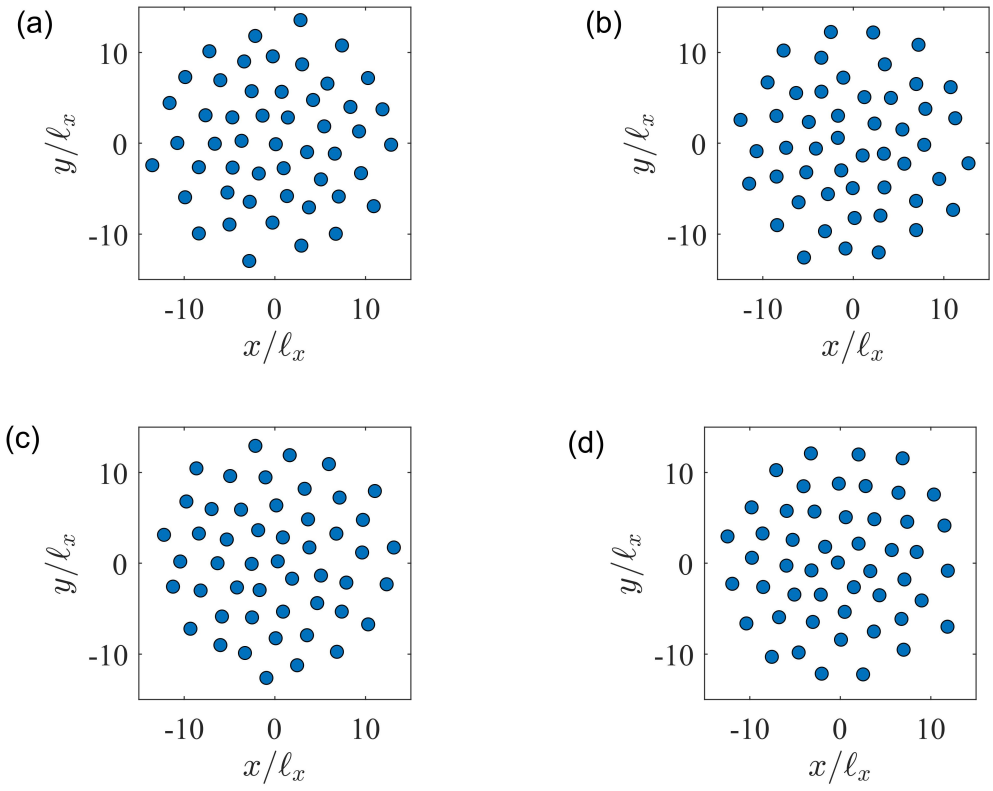

Figure 39: (a)-(d) Example realisations of a crystallised system of 50 atoms in a 2D pancake-shaped trap with aspect ratio $\ell_x/\ell_z = 30$. The parameters match those of Fig. (37 d).

4.6 Optical response of crystallised systems

We can study how these systems behave optically with the emergence of crystallised systems. Compared to non-crystallised systems, these systems' ordered structure could dramatically change the optical response. We start by looking at crystallised 1D chains before moving on to the crystallised 2D systems.

4.6.1 1D Chains

Incident on the 1D atom chains are beams with different propagation directions, which will change the response meaningfully. These two different beam orientations, 'on-axis' and 'off-axis', are shown in Fig. (27). These two different orientations can polarise the dipoles differently, leading to different optical responses in both cases. The on-axis orientation, for example, can easily polarise dipoles perpendicular to the chain axis but will struggle to polarise dipoles along the chain axis. Similarly, the perpendicular orientation can polarise dipoles along the axis but not in the beam propagation direction. We will begin with on-axis transmission and then study off-axis transmission.

4.6.1.1 On-axis incident beam

The optical response of a crystallised system of 10 atoms is studied where the sample is confined in a cigar-shaped trap $\ell_z/\ell_x = 25$. The incident beam has a width $W_0 k = 25$, polarisation $\hat{\mathbf{e}}_+$ and propagates along the z-axis as in Fig. (27b). The coherent and incoherent light is collected by a lens $1000/k$ away from the trap's centre, with a numerical aperture of 0.8 used in both cases. The optical response of the 1D chain Fig. (40) is markedly different from the non-crystallised analogue, Fig. (28); The line shape has multiple peaks, which are not seen in the non-crystallised system and has a striking asymmetry. Multiple eigenmodes appear excitable at different detunings in the crystallised case, while only one mode seems to contribute considerably to the peak scattering before crystallisation.

In Fig. (41), the occupation of eigenmodes within the system is shown at various detunings of the beam from the single atom resonance. For each peak in the scattering, a primary set of eigenmodes is occupied in the system, with this occupation changing with the beam detuning.

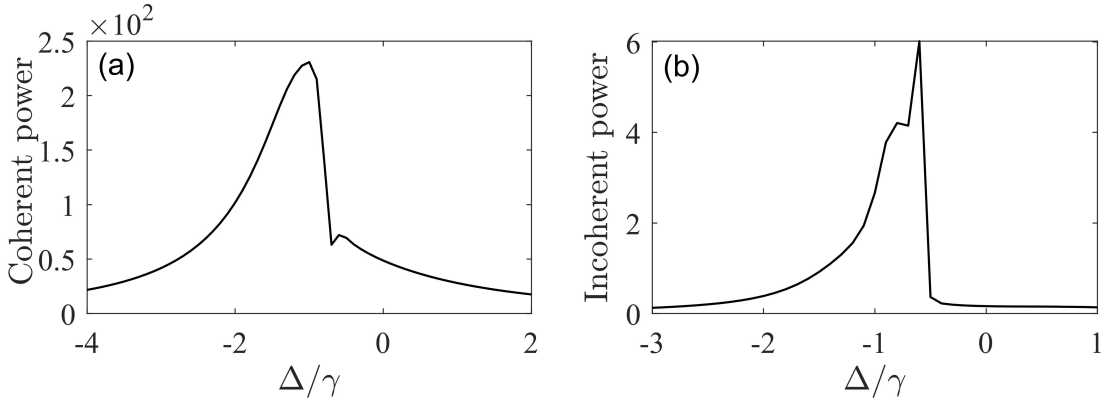

Figure 40: (a) Coherently and (b) incoherently forward-scattered power (in units of incident light intensity/k^2) from 10 atom chain in a cigar-shaped trap ($\ell_z/\ell_x = 25, \ell_x = \ell_y$) for magnetic interaction strength $R_{\rm dip}\bar{\rho}_{\rm 1D} \simeq 2.5$ at peak density $\bar{\rho}_{\rm 1D}/k \simeq 0.67$. The light propagates parallel to the long axis of the trap (Fig. 27 b), and a lens on the z-axis $1000/k$ away from the trap centre with NA 0.8 collects both coherent and incoherent power. The peak values of the scattering occur at -1γ and -0.6γ.

In Figs. (41, a-c) the occupation of the available modes in the system are shown where the beam detuning is matched to the peaks in the collected scattering. In Fig. (41,d) the total occupation of modes across all collective resonances is shown for the three cases above. The first peak at -1γ (Fig. (41, a)) corresponds to two modes, one that has a linewidth equal to the single atom linewidth while the other is slightly subradiant. The second peak at -0.6γ (Fig. (41, b)) is most clearly seen in the incoherent scattering but also as a small peak in the coherent scattering. This peak corresponds to the excitation of two subradiant modes almost exclusively. The narrowness of the peak in the transmission shows that when the beam detuning is not very close to the collective resonance of the subradiant modes, other modes will be preferentially excited. This narrow excitation is particularly clear in the incoherently scattered light. It should also be noted that the width of this peak is due to the excitation of either of the subradiant modes, which have slightly different resonant frequencies. Therefore, the width of this peak still overestimates the range of detunings the individual modes can be excited by. Finally, the occupied modes have collective resonances far from the single atom resonance for zero detuning. This explains the sharp drop in scattering seen for no-detuning and blue detuning. These modes are not going to be excited well for such a large detuning but are the ones primarily occupied in the system.

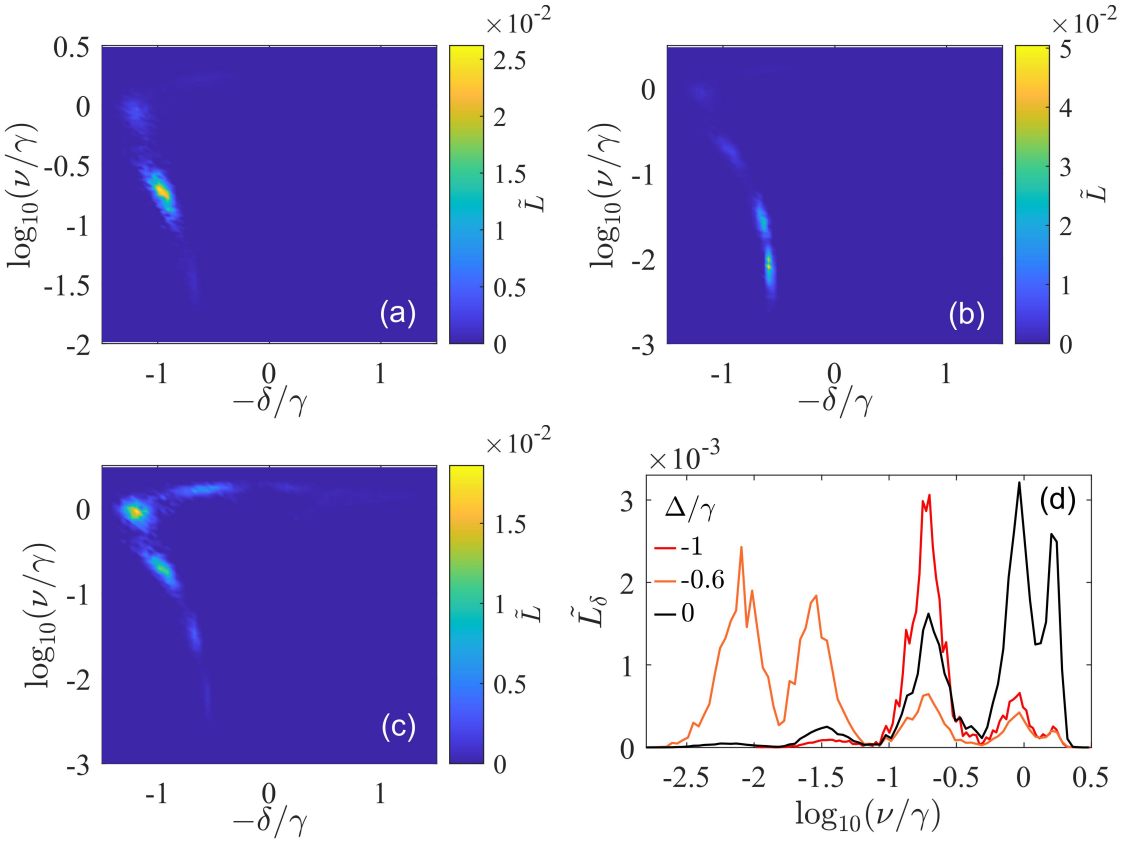

Figure 41: Eigenmode occupation for the 10-atom chain of Fig. (40) for beam detunings (a) -1γ, (b)-0.6γ, (c) 0γ where the beam detunings are selected to match features in Fig. (40). (d) Total occupation of modes for the linewidth $\log_{10}(\nu/\gamma)$ across all collective resonances δ/γ where the bin sizes $[\Delta \log_{10}(\nu/\gamma) \times \Delta\delta/\gamma] = [0.053, 0.023]$.

In Fig. (42), the eigenmode occupations of a single realisation of the 1D chain of 10 atoms from Fig. (41) is shown; All physical parameters remain the same. The incident beam in each case has the same detuning as previously. Each point in each figure shows an eigenmode of the system with eigenvalues $\nu/\gamma, \delta/\gamma$. Eigenmodes with reasonable occupation ($> 0.01\%$) are shown as blue points, while unoccupied eigenmodes ($< 0.01\%$) are shown in black. The occupations of modes of interest are labelled near each eigenmode. The most occupied modes are shown in red or orange. The occupation of these modes aligns well with the binned occupations from 41. However, there is some deviation based on the fluctuation of the realisation from the ensemble average. The specific realisation chosen is shown in Fig. (42d). On the left, the realisation is shown with equal scaling on both axes, while on the right, the x-axis is expanded to show separations between atoms in the short direction. With each different detuning, a small cluster of eigenmodes are highly occupied while all other modes are either negligibly occupied or have small occupation. When the detuning of the beam is -0.6γ, the excited modes are almost exclusively only the subradiant modes. A much wider cluster of modes is occupied for other detunings, even if only by a small amount. Comparing Fig. (42a,c), we can see that the occupied modes are very similar for both detuning values. Which modes are the most occupied is modified, but a similar set of modes is occupied. In this crystallised system, it is possible to excite a subradiant mode, but the detuning of the beam has to be very precise. In contrast, the other modes in the system can be easily excited for multiple detunings.

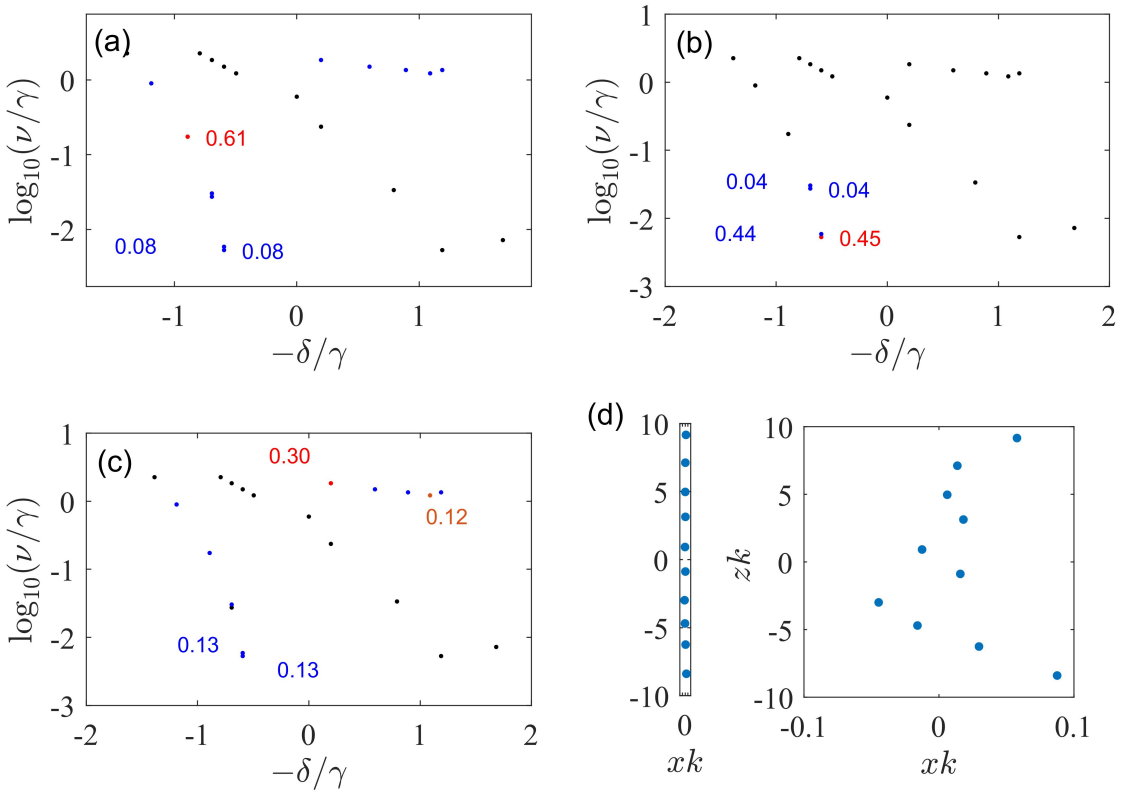

Figure 42: Eigenmode occupations of a single realisation of the 1D 10-atoms chain as in Fig. (40). The incident beam in each case has detuning (a) -1.6γ, (b) 1.6γ. (c) Scatter plots of the atom positions in the chain of the chosen realisation: Left shows the chain where the x and y axes have the same scaling, and right shows the same data with an expanded scale in the short direction. The modes shown have labelled occupations only if the occupation is greater than 0.01; these labels are red for the most occupied modes and orange when it would otherwise be hard to differentiate neighbouring modes.

4.6.1.2 Off-axis incident beam

We can similarly study the excitation of the 1D chain when the incident field propagates perpendicular to the axis of the chain, Fig. (27a). This orientation allows for the excitation of modes with atomic electric dipoles polarised along the axis of the chain. Fig. (43) shows the optical response of the chain to an incident Gaussian beam with circular polarisation $\hat{\mathbf{e}}_+$. In this case, the optical response is less complex, with two peaks in the incoherent scattering and one in the coherent. The coherent scattering peak also matches the second peak's detuning in the incoherent scattering, implying the same mode causes both. We should expect only two modes would be easily excitable in this orientation, which is indeed the case in Fig. (44).

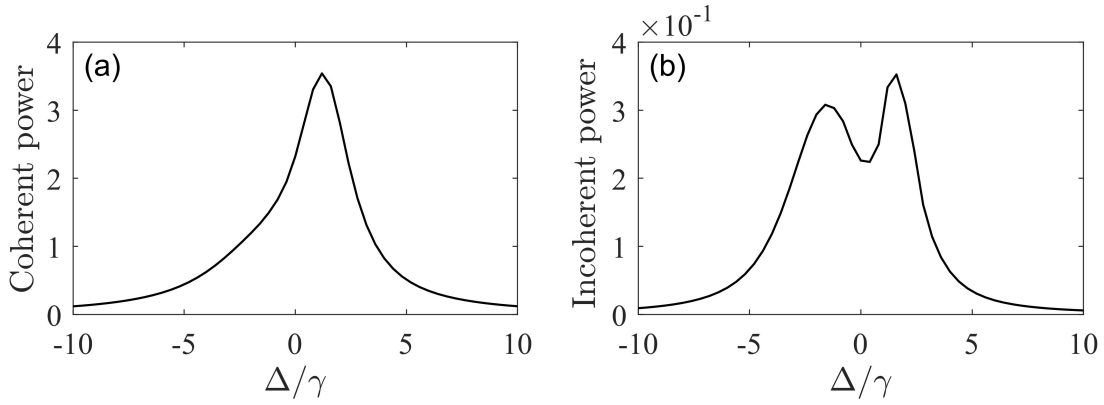

Figure 43: (a) Coherent and (b) incoherent forward-scattering of a crystallised 1D chain of 10 atoms. The incident Gaussian beam propagates along the cigar's short axis (Fig. 27 a), with polarisation $\hat{\mathbf{e}}_+$ and width $W_0 k = 8.5$. The system is at density $\bar{\rho}_{1\mathrm{D}}/k \simeq 0.67$ and the confining trap has an aspect ratio of $\ell_y/\ell_x = 25$

In this off-axis case, the modes primarily occupied are superradiant. There is a small excitation of a subradiant mode for blue detuning, but the primarily excited modes, in this case, are superradiant. The two superradiant modes are clearly differentiated and produce the two different peaks in the incoherent transmission.

We must consider the collecting lenses to understand better why a second peak is only present in the incoherent scattering. The coherent scattering is collected with a 0.2 aperture lens, while the incoherent is collected with a larger 0.8 numerical aperture lens. The second peak in the incoherent scattering, similar to earlier examples, is such that the scattering it produces is directed away from the optical axis.

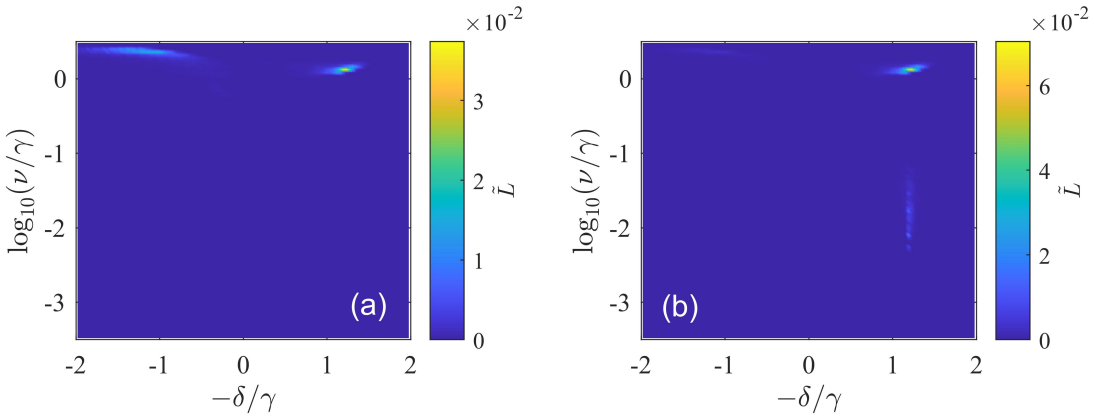

Figure 44: Binned eigenmode occupation for the 10-atom crystal with off-axis incident beam orientation as in Fig. (43). The detuning of the beam is varied to match each of the peaks across the coherent and incoherent scattering (a) -1.6γ, (b) 1.6γ.

Again, we can study single realisations of the system to get a clearer picture of how different eigenmodes are being excited. In the off-axis orientation, it is considerably harder to excite any subradiant modes, even when the beam detuning well matches the resonance; superradiant modes of similar resonance are preferentially excited instead. The excitable modes in the on and off-axis orientations depend on the polarisation of the incident light. We can show the form of some of these modes to understand better why we can or cannot excite them. In Fig. (46), the orientation of the electric dipoles is shown for different eigenmodes of the system. We look at examples of super- and subradiant modes that are excitable for both blue and red detuning in the on and off-axis orientations. Figures (a) and (d) show excitable modes in the on-axis orientation. The former is a subradiant mode, which can be expected from the many opposing dipole orientations, while (d) is a superradiant mode with many aligned dipoles next to each other. Similarly, (b) and (c) are modes most easily excited in the off-axis orientation because the dipoles are polarised primarily along the axis of the chain. Again, (b) is subradiant because of the opposing dipole orientations, while (c) is expected to be superradiant because of the long chains of aligned dipoles.

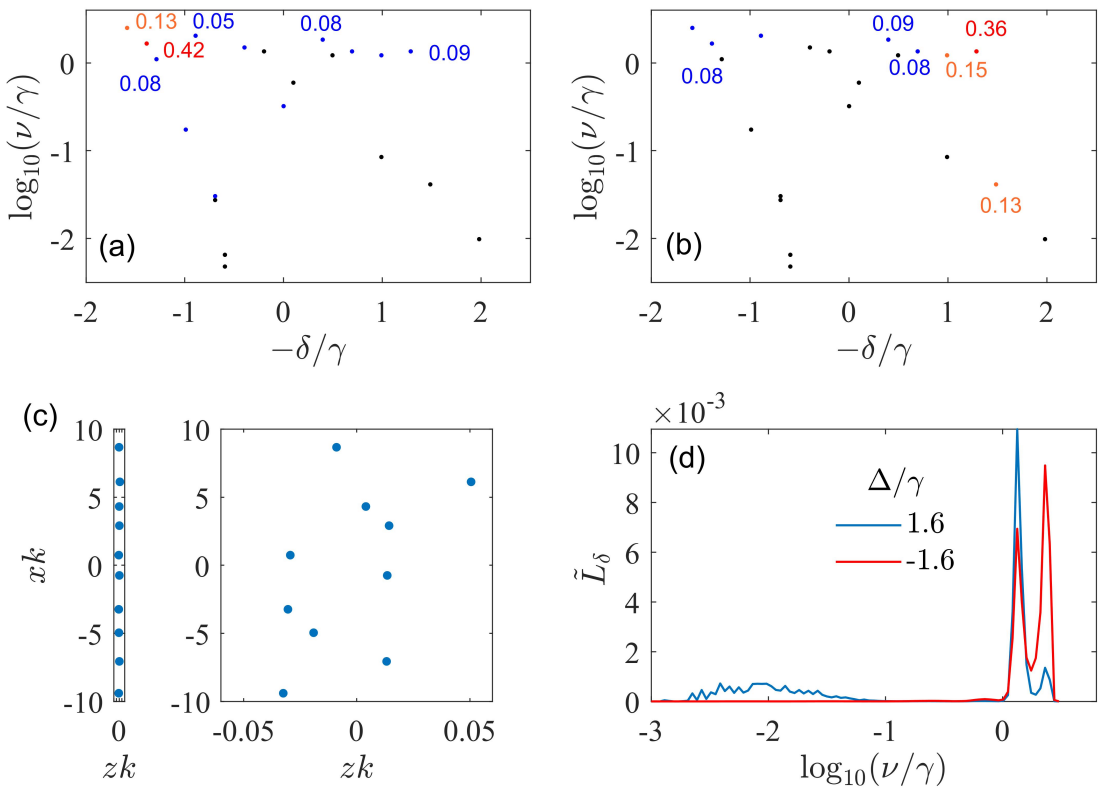

Figure 45: Eigenmode occupations of a single realisation of the 10 atoms 1D chain as in Fig. (43). (a) Eigenmode occupation for a single realisation of the 10-atom 1D chain where the beam detuning is (a) -1.6γ, (b) 1.6γ. (c) Scatter plots of the atom positions in the chain of the chosen realisation: left shows the chain where the x and y axes have the same scaling, and the right shows the same data, but the distance in the short direction is expanded. (d) Total occupation of modes for the linewidth $\log_{10}(\nu/\gamma)$ across all collective resonances δ. The modes shown have labelled occupations only if the occupation is greater than 0.01; these labels are red for the most occupied modes and orange when it would otherwise be hard to differentiate neighbouring modes.

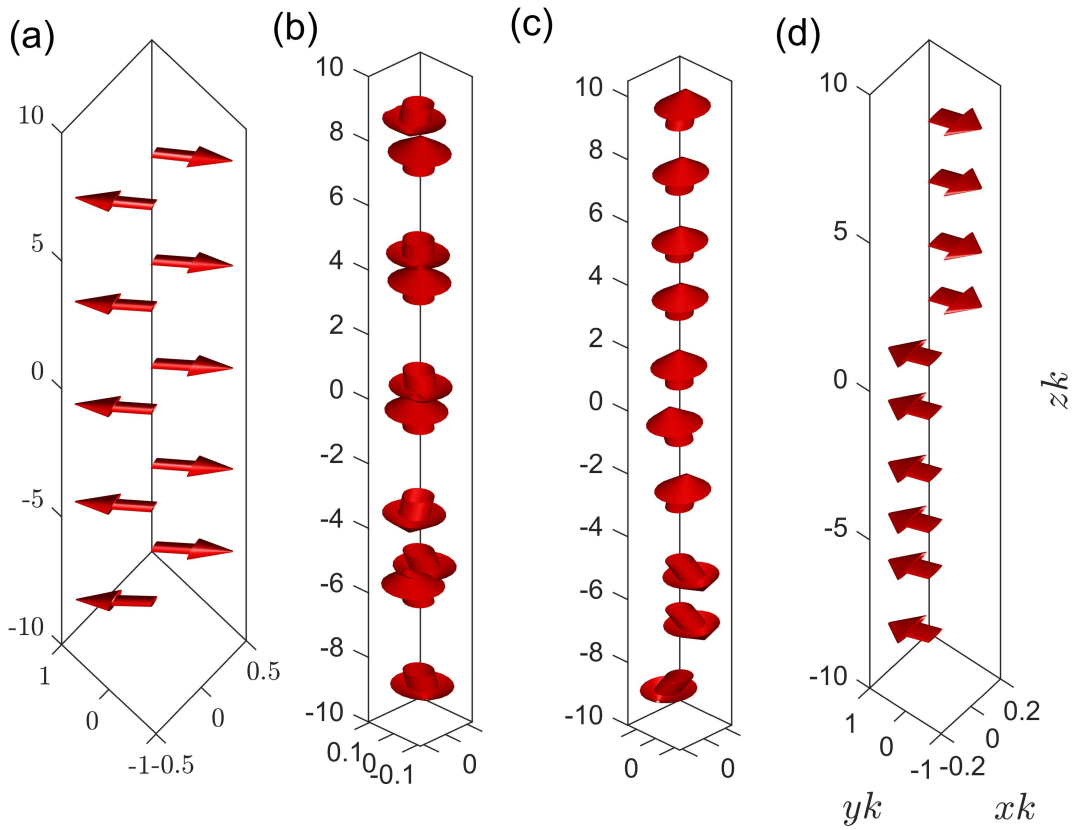

Figure 46: A selection of eigenmodes from the ensemble of the 1D chain as in Fig. (40, 43). The orientation of the trap is as in Fig. (27b). However, the available eigenmodes are independent of the orientation. Shown are eigenmodes with eigenvalues (a) $\log_{10}(\nu/\gamma) = -2.27$, $-\delta/\gamma = -0.55$, (b) $\log_{10}(\nu/\gamma) = -1.78$, $-\delta/\gamma = 1.20$, (c) $\log_{10}(\nu/\gamma) = 0.34$, $-\delta/\gamma = -0.78$, (d) $\log_{10}(\nu/\gamma) = 0.15$, $-\delta/\gamma = 1.18$.

4.6.2 2D Crystals

We now study the optical response of 2D crystallised systems at high density. We begin by studying the available eigenmodes of the system before exploring how these modes can be excited.

4.6.2.1 Eigenmodes of 2D crystals

The available eigenmodes of a 2D interacting system will depend both on the density of the sample, in terms of the wavenumber k, and the interaction length because both modulate the separations between atoms. As the interaction length increases, the atomic positions become more confined, eventually forming a crystal-like structure. This reduces the number of pairs of atoms with short separations in favour of more uniform separation distances. In Figs. (47 a,c,d) are examples of stochastic realisations of a 50-atom sample where the interaction strength varies from weak to strong enough to cause crystallisation. When the interactions are weak, the distribution of atoms is quite random, and there are clusters of atoms with very close spacings to each other. When the system has crystallised, the separation of atoms generally increases, but most atoms are also separated from their nearest neighbours by the same distance. Alongside these realisations are shown the available eigenmodes in each case. As the interaction length increases, the eigenmodes become restricted to a smaller region of collective resonance values nearer the single-atom resonance. The central region of the eigenmode distribution remains while the large collective resonance modes are removed, see Figs. (47 b,d,e). This indicates that pairs of atoms with very small separations result in collective modes with large resonance shifts. These highly shifted modes are then generally removed with increasing interaction strength. In the earlier 1D case, we see similar behaviour: the eigenmodes become restricted to a smaller range of collective resonances for larger interaction strength. The systems' high density $\bar{\rho}_{2\mathrm{D}} \simeq 0.5k^2$ naturally closely spaces the atoms despite the crystallisation. This means shifted super- and subradiant modes can remain present in the system even if some are removed compared to a weakly interacting analogue. These modes separate into multiple 'islands' across the distribution, each corresponding to a unique eigenmode (up to rotations and reflections of the eigenvectors). These islands result from large numbers of similar atom configurations in the ensemble due to the regular structure.

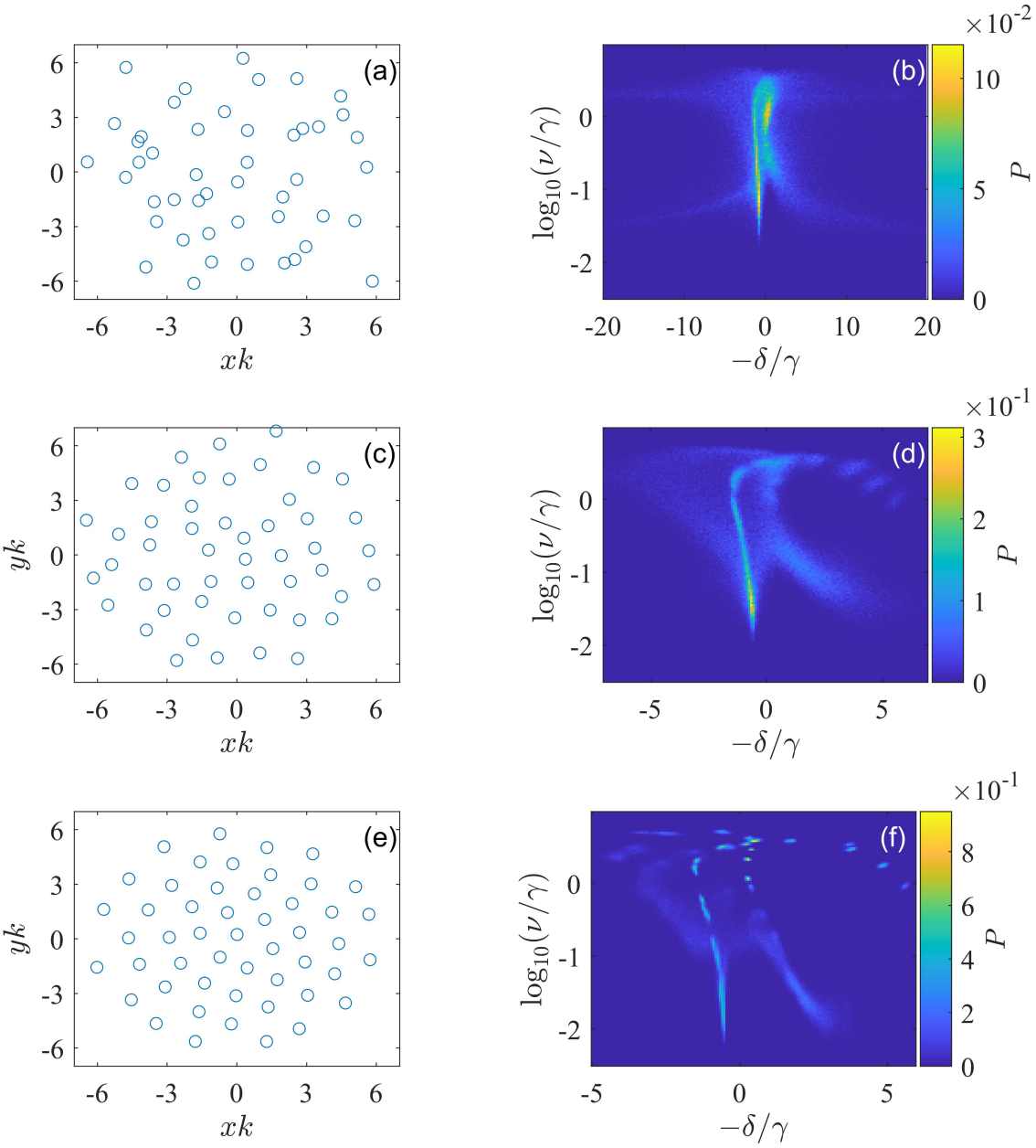

Figure 47: Distribution of eigenmodes in systems of 50 atoms held in a pancake-shaped trap ($\ell_x/\ell_z = 14, 6.4, 3$) for constant density $\bar{\rho}_{2D}/k^2 \simeq 0.5$. (b),(d),(f) The eigenmodes are plotted via the real and imaginary parts of their respective eigenvalues δ_n, ν_n, (a),(b),(c) with a representative atomic configuration shown beside each. The interaction strength in each case is $R_{\rm dip}\sqrt{\bar{\rho}_{2D}} = 0.1, 9.5, 653$.

4.6.2.2 Excitation of crystallised eigenmodes

The availability of highly ordered eigenmodes in the crystallised system is only useful if they can be excited. I examine how the eigenmode occupation changes between 2D crystallised and

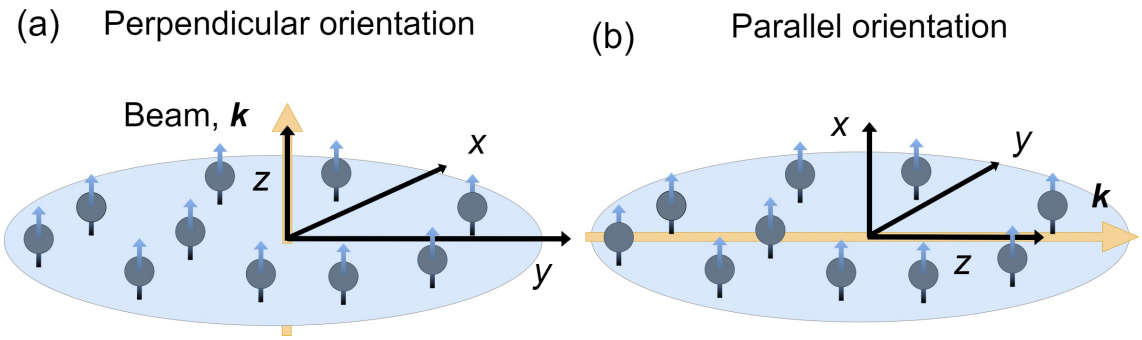

Figure 48: Schematic of pancake-shaped trap for (a) perpendicular and (b) parallel beam orientations. The beam propagation direction remains constant (along the z-axis) while the plane of the trap changes. In the perpendicular orientation, the trap plane is the (x, y) plane, while in the parallel orientation, it is the (z, y) plane.

non-interacting systems. Eigenmodes shown to have polarisation primarily out of the plane of the trap will be hard to excite with a beam that is propagating perpendicular to the trap plane. Therefore, I will also look at the case in which the beam propagates parallel to the plane direction. This is done by changing the plane of the trap from the (x,y) plane to the (y,z) plane rather than rotating the beam (Fig. 48). Fig. (49) compares the eigenmode occupation of interacting and non-interacting systems for different orientations and polarisations of the incident field, where there is no detuning from the single atom resonance. Figs. (49 a,b) show the case where the incident field propagates perpendicular to the trap plane with circular polarisation, $\hat{\mathbf{e}}_+$. When we try to excite modes with this orientation in the crystallised case, it is difficult to excite many modes. A few superradiant modes are excited almost exclusively, with very few other modes excited. This is contrasted against the non-interacting case, where it is easy to excite modes near the single atom resonance and linewidth. Modes away from this position are also occupied to a reasonable amount.

Once we change the beam propagation to be parallel to the trap plane (y, z), we can easily excite other modes in the system in the crystallised case. When the beam polarisation is $\hat{\mathbf{e}}_y$ (which is directed in the plane), most of the modes within the system become excited. There is little change in the occupation of the non-interacting system between the two orientations, showing the main mode being excited is in-plane and is excited well with either circular or linear in-plane polarisation. When the beam propagation is parallel but the polarisation is $\hat{\mathbf{e}}_x$

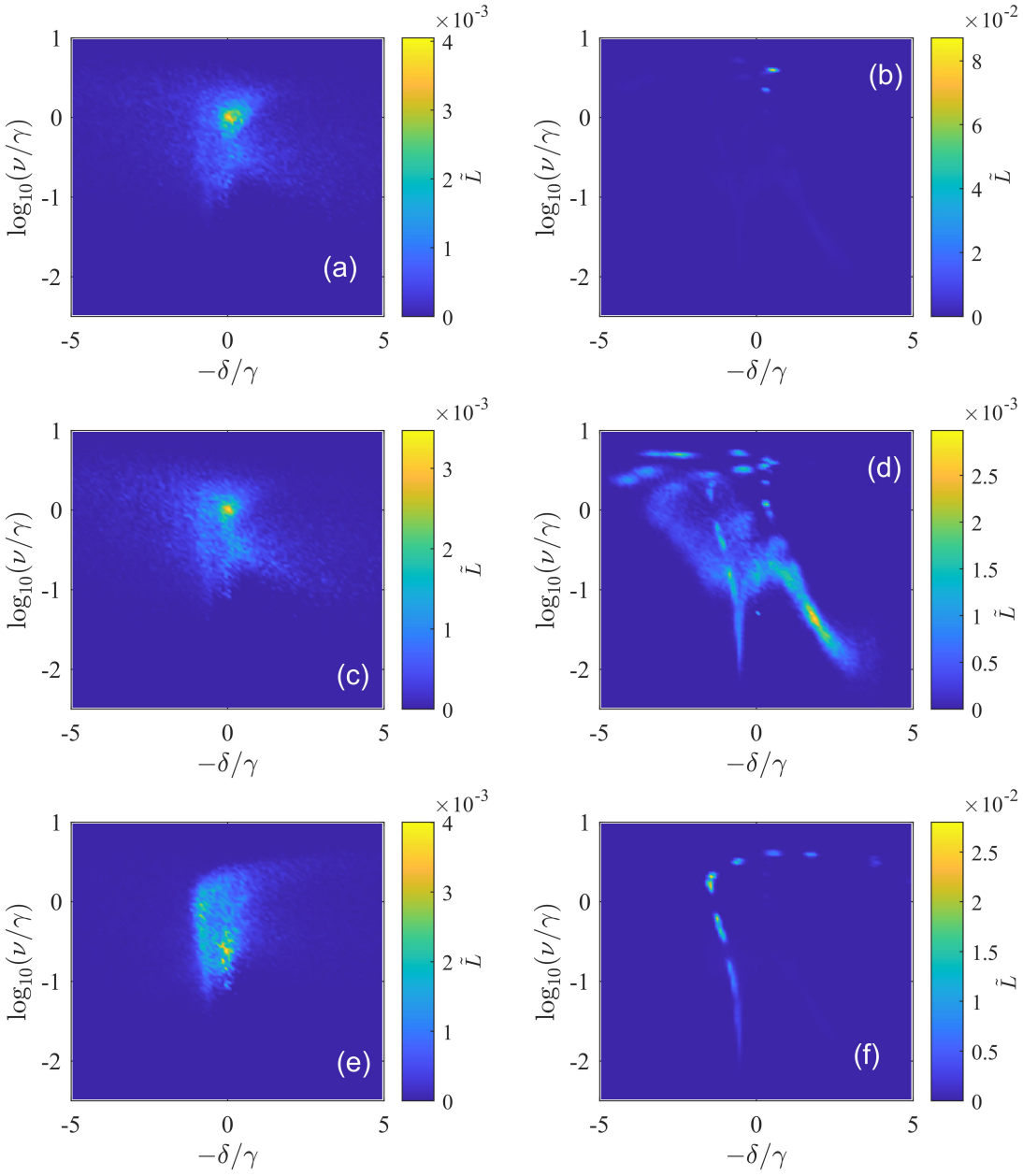

Figure 49: Eigenmode occupation in non-interacting and crystallised 2D systems of 50 atoms at high denity $\bar{\rho}_{2D}/k^2 \approx 0.5$. The interacting cases are as in Fig. (48), and the non-interacting cases are analogues at matched peak density. (a,b) The incident beam is Gaussian propagating perpendicular to the plane of the pancake-shaped trap (x, y) plane (Fig. (48 a)), with polarisation $\hat{\mathbf{e}}_+$. (c,d) The incident beam is propagating along the z-direction parallel to the plane of the pancake-shaped trap (z, y) (Fig. (48 b)), with polarisation $\hat{\mathbf{e}}_y$. (e,f) The incident beam is propagating along the z-direction parallel to the plane of the pancake-shaped trap (z, y) (Fig. (48 b)), with polarisation $\hat{\mathbf{e}}_x$. The non-interacting cases are in the left column, while the interacting cases are in the right column.

(out-of-plane) the occupation changes substantially with only a central line of the available modes becoming excited. We would expect these modes to be polarised primarily out-of-plane while the other modes from (d) are primarily in-plane. In section 4.6.2.5, we will see this is true.

4.6.2.3 Perpendicular transmission

The optical response of the 2D crystallised systems is now investigated for the same beam orientations and polarisation as above. Similar to the 1D case, it makes sense to consider using perpendicular and parallel propagating incident beams. We have seen from the eigenmode excitation that these orientations should produce differing responses in the system. For clarity, in this case, the beam will always travel along the z-axis, but the plane of the trap will change orientation, as before. The perpendicular orientation refers to when the trap plane is (x, y) while the parallel orientation refers to the trap plane being (y, z), Fig. (48).

We take a crystallised system of 50 crystallised at high density ($\bar{\rho}_{2\mathrm{D}}/k^2 \approx 0.5$) and have incident on it a Gaussian beam of polarisation $\hat{\mathbf{e}}_+$ and width $W_0 k = 6$ to match the width of the sample, Fig. (50). Similar to the 1D case, we see the optical response becoming more complex, with several peaks in the optical response. Notably, there is a very narrow peak in the incoherent scattering for detuning -0.5γ and several small peaks for blue detuning. This indicates we may have a similar subradiant mode as in the 1D case and several closely spaced eigenmodes for blue detuning. By looking at the occupation of eigenmodes of the system for detunings matching the peak resonances, we can see that each peak corresponds to the excitation of a set of eigenmodes. Usually, one prominent mode and then several less occupied modes, Fig. (51). This perpendicular orientation makes it hard to excite any modes other than a set of closely spaced superradiant modes. These modes are quite easy to excite in this orientation even when the beam detuning poorly matches the collective resonance of these modes. We can see that a subradiant mode exists that can be excited for a correctly chosen detuning, but similar to the 1D system, if the detuning is wrong, a different set of superradiant modes is excited instead. The peak in the scattering corresponding to this subradiant mode is again very narrow, showing how sensitive its excitation is to detuning.

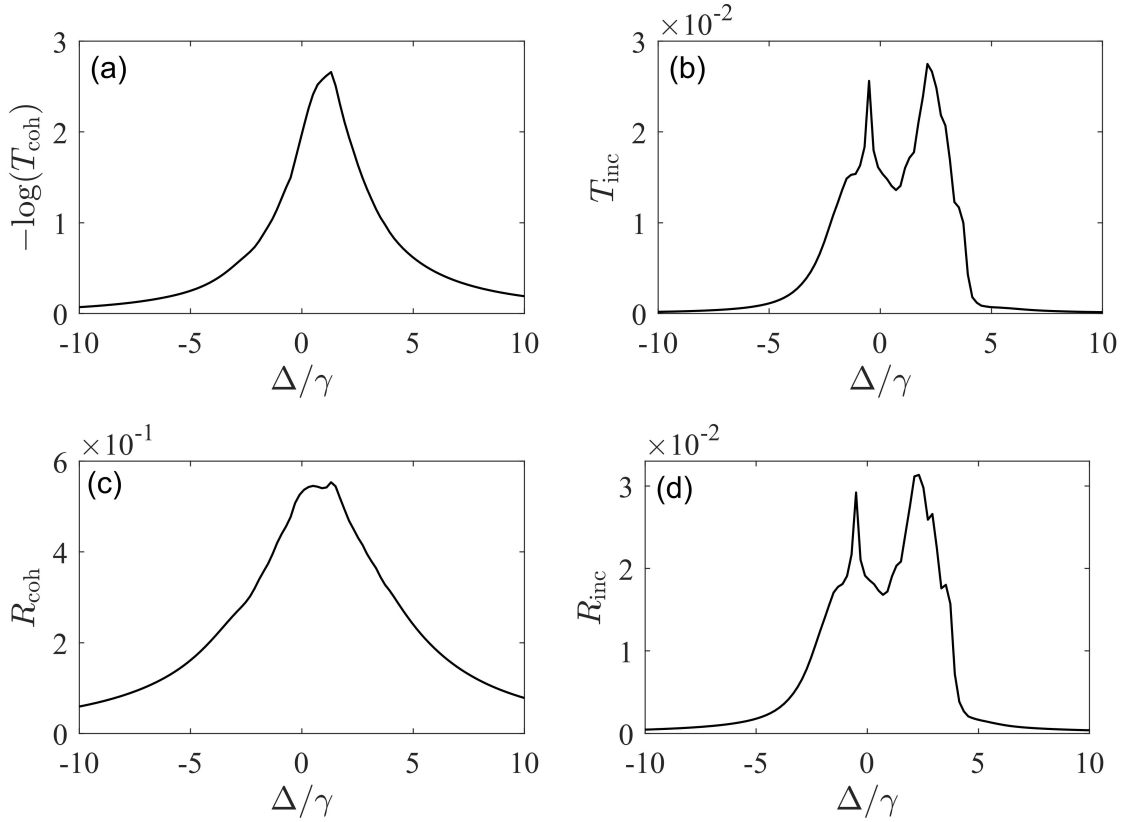

Figure 50: Optical response of the 2D crystallised system of 50 atoms as in Fig. (47 e,f) at peak density $\bar{\rho}_{\rm 2D}/k^2 \simeq 0.5$. The incident Gaussian beam has a perpendicular orientation, Fig. (48 a), width $W_0 k = 6$ and polarisation $\hat{\mathbf{e}}_+$.

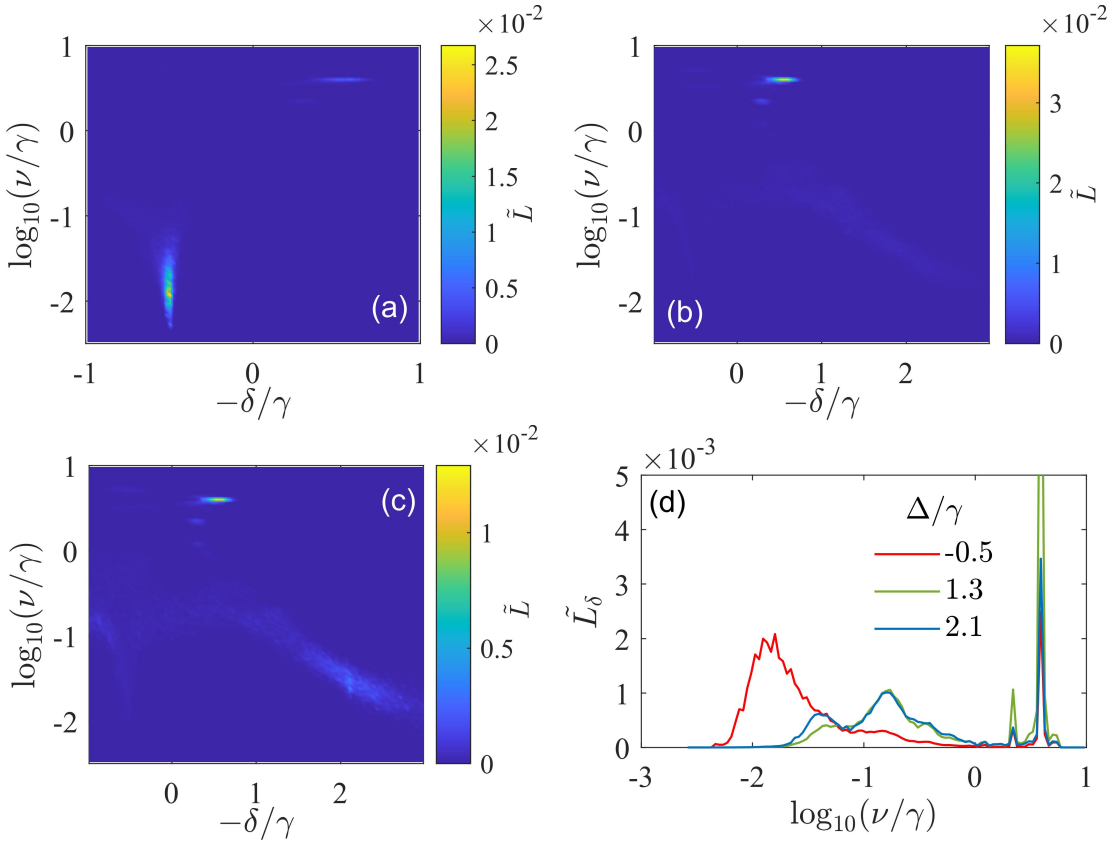

Figure 51: Eigenmode occupation of a crystallised system of 50 atoms as in Fig. (47 e,f) with perpendicular beam orientation, Fig. (48 a). The beam is polarised $\hat{\mathbf{e}}_+$ and has width $W_0 k = 6$. In each case, the beam has detuning (a) -0.5γ (b) 1.3γ (c) 2.1γ. (d) Total occupation of modes for the linewidth $\log_{10}(\nu/\gamma)$ across all collective resonances δ.

4.6.2.4 Parallel transmission

The parallel orientation of the beam allows for two different kinds of polarisation of the dipoles in the sample, out-of-plane and in-plane. To excite these modes separately, we can choose the beam polarisation to be either $\hat{\mathbf{e}}_x$ or $\hat{\mathbf{e}}_y$, respectively. The optical response of the crystallised system again has a complex line shape with many peaks, Fig. (52). The system's response to the two different orientations is substantial, with no discernible similarity between peaks in the two line shapes. We can again look at the occupation of eigenmodes near the peaks in each case to see how the excited eigenmodes change. We begin with the out-of-plane case ($\hat{\mathbf{e}}_x$) shown in black in Fig. (52). The optical response is reminiscent of the on-axis 1D case. This seems reasonable since the driven polarisation is out of the system's plane in both cases, even though in 1D, this is restricted to a line. In Fig. (53), the occupied eigenmodes of the 50 atoms system when the beam has polarisation $\hat{\mathbf{e}}_x$ is shown. The beam detuning is chosen for each case to match one of the coherent or incoherent scattering peaks. The response in terms of occupied eigenmodes is again similar to the 1D on-axis case. The leftmost peak corresponds to a mode of similar collective resonance (-1.5γ) and collective linewidth of approximately 1γ ($\log_{10}(\nu/\gamma) = 0$). Several other nearby modes are also partially excited in this case. For detuning -0.7γ, the excitation concentrates in a subradiant mode to the exclusion of most other modes in the system. For blue detuning 2.5γ, there are a set of superradiant modes excited as well as other modes, including a small excitation of a subradiant mode. The excitation of these modes is different to the 1D on-axis case, where instead, modes with very different collective resonance were occupied. This coincided with an extinction of the scattering that is much more dramatic than in this 2D system, showing these superradiant modes contribute to the response seen for blue detuning. Looking at the case where the incident field has polarisation $\hat{\mathbf{e}}_y$, many more modes are occupied for all detuning values. Like previously, the examples shown have detuning values that match the peaks in the optical response. The first example has red-detuning -4.5γ. In this case, there is a prominent superradiant mode excited, with a collection of other more superradiant modes also occupied but less so. The occupied modes change as the detuning changes to -2.3γ, which matches the first peak in the incoherent scattering. Firstly, there is a mode near the single atom linewidth that is excited but, interestingly, also a subradiant mode that is not near the detuning frequency. There seems to be no noticeable effect of this mode, though, on

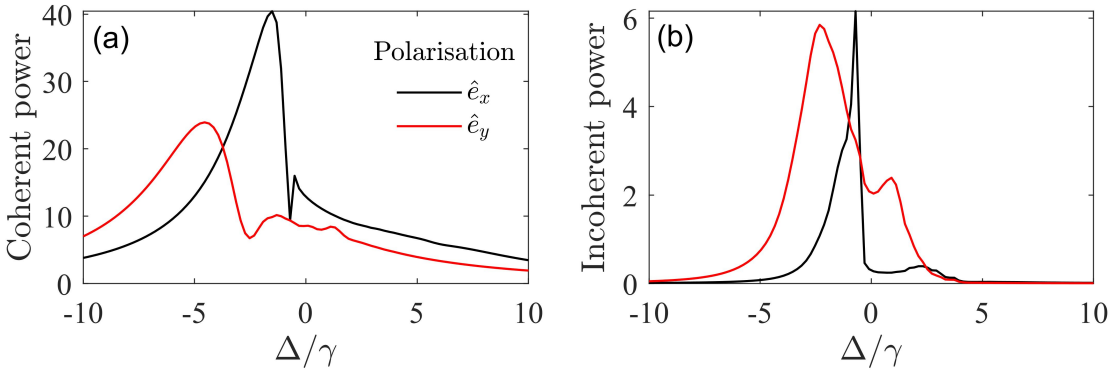

Figure 52: Optical response of the crystallised system of 50 atoms as in Fig. (47 e,f) with parallel beam orientation, Fig. (48 b). The sample has peak density $\bar{\rho}_{2D}/k^2 = 0.5$ and an incident Gaussian beam of width $W_0 k = 6$ and polarisation $\hat{\mathbf{e}}_x, \hat{\mathbf{e}}_y$ respectively. The beam propagates in the z-direction while the plane of the trap is in the y, z plane. The beam polarisation $\hat{\mathbf{e}}_x$ is therefore perpendicular to the trap plane while $\hat{\mathbf{e}}_y$ is along the trap plane.

the scattering intensity (particularly around its collective resonance), which indicates it either produces little scattering or scattering away from the lens direction.

Finally, for blue detuning, the primary excited mode becomes superradiant again. Another cluster of superradiant modes nearby is also excited, which likely is why we see many small peaks in the coherent scattering around this frequency. As the detuning scans around this range, the beam will gradually move through exciting different eigenmodes from this group; each time, a small increase in total scattering is seen.

In summary, using a parallel orientation, we can excite many different modes in a crystallised system, but importantly, with a change of polarisation, we can select between two distinct subsets of modes. The modes available are often super- and subradiant and can be occupied with the right incident field and detuning.

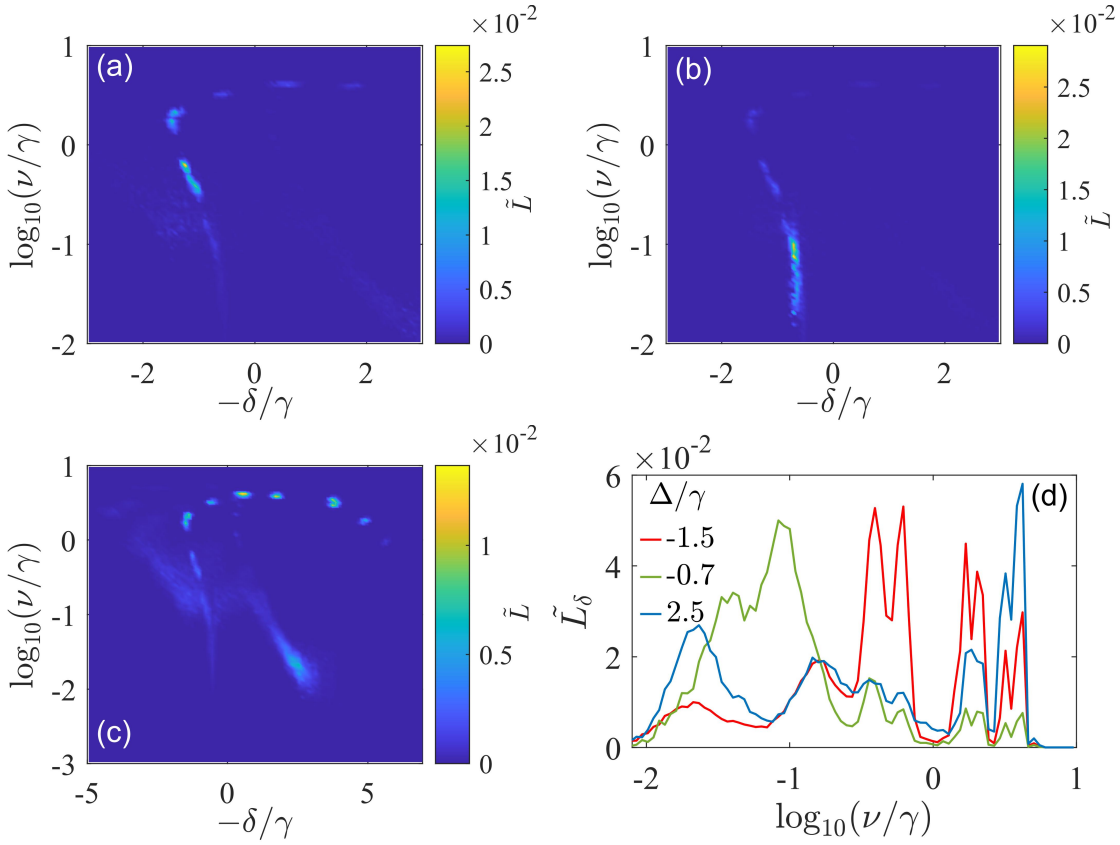

Figure 53: Eigenmode occupation of the crystallised system of 50 atoms as in Fig. (47 f) with parallel beam orientation, Fig. (48 b) for the beam polarisation $\hat{\mathbf{e}}_x$, which is out of the plane of the system. In each case, the beam detuning matches a key feature in the transmission: (a)-1.5γ, (b)-0.7γ, (c)2.5γ. (d) Occupation across all collective resonances $\tilde{L}_\delta$.

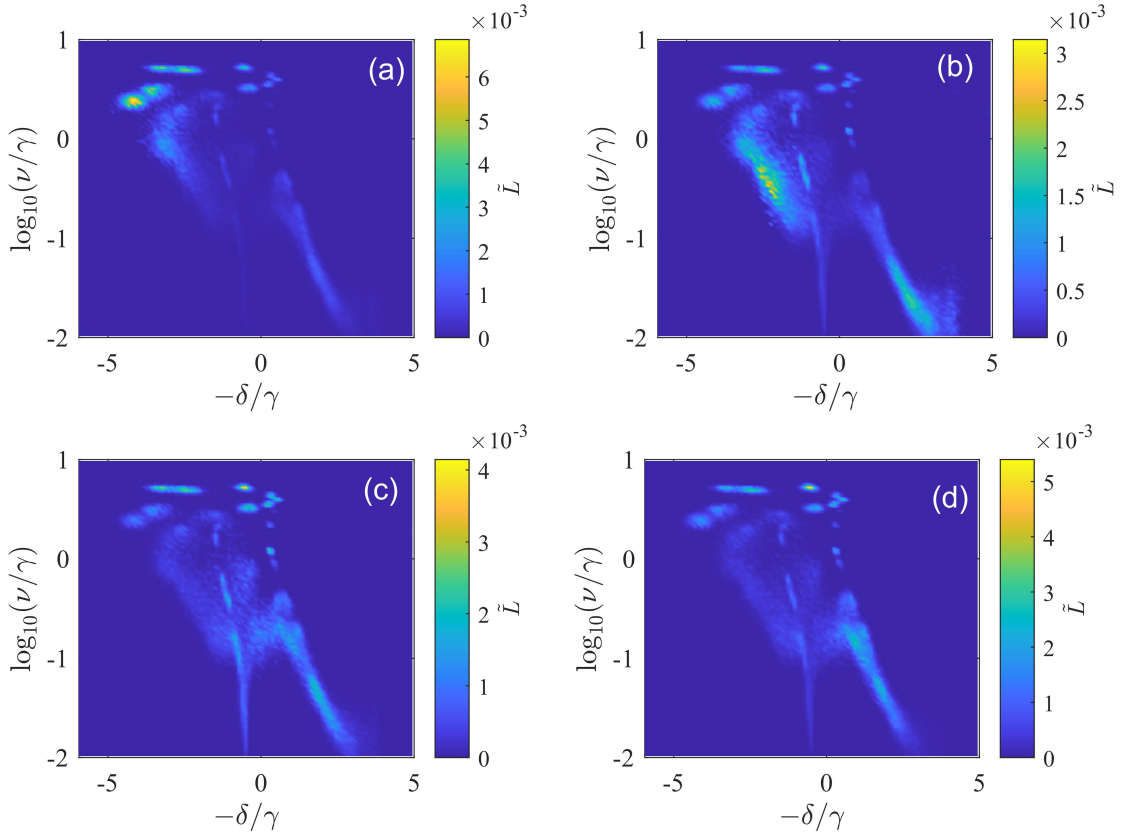

Figure 54: Eigenmode occupation of the crystallised system of 50 atoms as in Fig. (47 f) with parallel beam orientation, Fig. (48 b) for the beam polarisation $\hat{\mathbf{e}}_y$, which is in-plane of the system. In each case, the beam is detuned to match a key feature in the transmission: (a)-4.5γ, (b)-2.3γ, (c)0.9γ. (d) Occupation across all collective resonances $\tilde{L}_\delta$.

4.6.2.5 Eigenmode ellipses

To understand why the change in polarisation changes the modes we can occupy, it is worth trying to understand what these different modes look like in terms of the polarisation across the crystallised samples. Because of the more complex system to fully visualise the eigenmodes, we cannot simply show the atom polarisations. Instead, the polarisation of the system of atoms can be studied by drawing a 'polarisation ellipse' for each. This ellipse is defined by the ratio between its semi-minor and semi-major axis $\frac{b}{a}$, and an angle of rotation χ from the x-axis, see Fig. (55) [67]. The ratio of the ellipse semi-major and semi-minor axis is given by

$$\frac{b}{a} = \tan(\chi) \tag{68}$$

where χ is the ellipticity angle of the ellipse. The orientation of the ellipse is given by the angle

$$\psi = \frac{1}{2}\sin^{-1}\left(\frac{S_0}{S_3}\right), \tag{69}$$

where S_0, S_1, S_2, S_3 are the parameters

$$S_0 = P_x^+ P_x^- + P_y^+ P_y^- \tag{70}$$

$$S_1 = P_x^+ P_x^- - P_y^+ P_y^- \tag{71}$$

$$S_2 = P_x^+ P_y^- + P_y^+ P_x^- \tag{72}$$

$$S_3 = i\left(P_x^+ P_y^- - P_y^+ P_x^-\right) \tag{73}$$

which are modified from the standard stokes parameters, [67] using polarisation instead of electric field amplitudes. Finally, the sense of the rotation around the polarisation ellipse is defined by the sign of S_3, where if $S_3 > 0$, the rotation is clockwise and if $S_3 < 0$, the rotation is anticlockwise.

In Fig. (56) I show various eigenmodes represented as polarisation ellipses for the crystallised system of 50 atoms. Each ellipse is centred on the atom that it represents, plotted with the appropriate orientation and ellipticity. The sense of the ellipse is shown via an arrow on the ellipse, which is also coloured. If the arrow is red, the sense is clockwise, while if it is magenta, it is anticlockwise. The ellipse in each case also shows the total complex phases of the polarisation components by the colour of the ellipse.

$$\phi = \arg(P_x) + \arg(P_y) \tag{74}$$

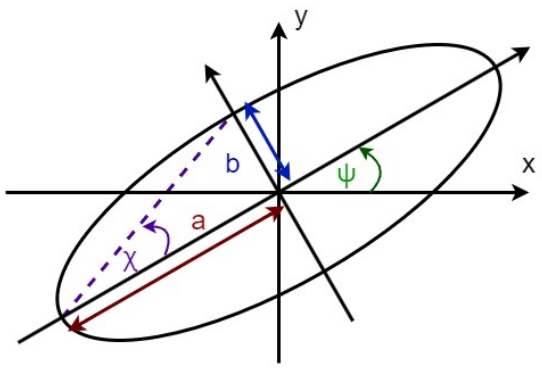

Figure 55: Schematic of the polarisation ellipse. The ellipse has an orientation angle ϕ and ellipticity angle χ.

The modes seen in each island are distinct from each other in their characteristics in terms of orientation, ellipticity and phase distribution while being consistent within an island. Eigenmodes have been selected for their clear features. Several of these modes seem to follow trends in their features in the islands. For example, (d),(e), and (f) appear to be based on a feature where the ellipses point away from a central point. In (d), there is only one central point, while in (e) and (f), there are 2 and 4, respectively. The island these modes correspond to also falls onto a sequence of islands near zero detuning but descending linewidth; see Fig. (57). Similar related features can be seen between (a) and (b) as well as between (g) and (h).

This current definition of the polarisation ellipse allows us to study the polarisation in the x-y plane but not in the out-of-plane direction. Since some eigenmodes are primarily out-of-plane, we can modify the definition to represent this kind of polarisation. To create a similar out-of-plane ellipse, the analogous construction is used, but where the substitutions

$$P_x \to P_+, P_y \to P_0 \tag{75}$$

are made.

The complex phase shown in this case is simply the argument of the z-component of the polarisation.,

$$\phi_z = \arg(P_z). \tag{76}$$

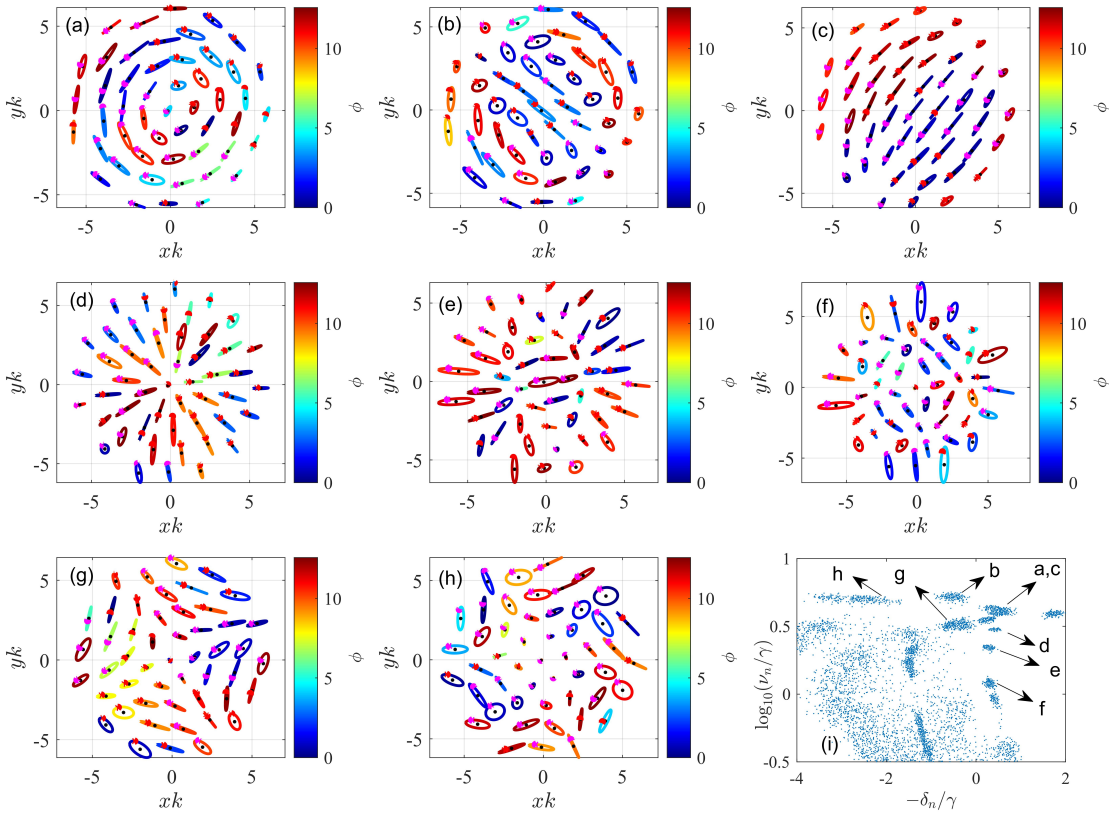

Figure 56: Polarisation ellipses of eigenmodes of the 2D crystallised system of 50 atoms from Fig. (47 f), where $\bar{\rho}_{2D}/k^2 = 0.5$. Each ellipse is centred at the position of the atom it represents. The colour of the ellipse signifies the total complex phase of the polarisation components as a value between 0 and 4π, ϕ Eq. (75). Each eigenmode maps to an island in the available eigenmodes, shown in (i).

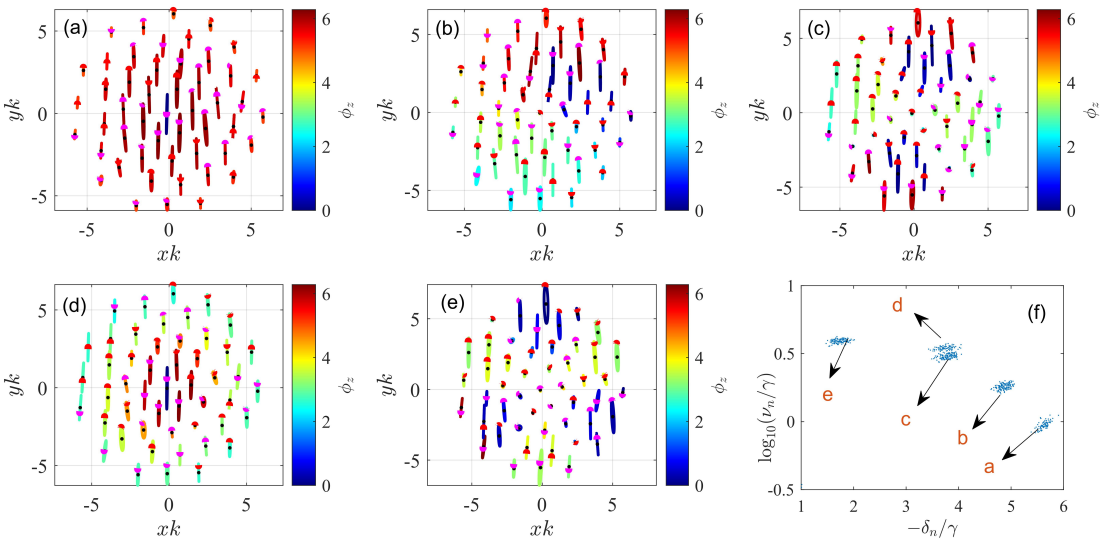

Figure 57: Polarisation ellipses of eigenmodes of the 2D crystallised system of 50 atoms from Fig. (47 f), where $\bar{\rho}_{2D}/k^2 = 0.5$. The polarisation ellipses for out-of-plane modes are shown. The colour of the ellipses represents the complex phase of the z-component of the polarisation, ϕ_z, Eq. (76). Each ellipse has a coloured arrow, which shows the sense of the ellipse: red arrows show clockwise sense, and magenta arrows show anticlockwise sense. (f) Shows the scatter plots of available eigenmodes from the crystallised system (from 50 realisations) and highlights how each mode corresponds to each island. Each eigenmode maps to an island in the available eigenmodes, shown in (f).

The out-of-plane modes show similar trends to the in-plane modes but are easier to identify. The mode islands follow a clear progression as detuning decreases and linewidth increases. As you move between these islands, the number of nodes in the complex phase increases of each eigenmode increases. In (a), the atoms are all of the same phase, while in (b), there are two regions where the phases are 180 degrees out of phase. In (c), there are now 4 of these regions, and finally, in (e), there are 6. (d) Shows a different phase structure where there are two regions but the distribution is radially symmetric. Similar structures have been observed in other work such as [68].

5 Conclusions

5.1 Weak dipole-dipole interactions

Introducing magnetic dipole-dipole interactions into dense systems of atoms modifies the cooperative optical response of these systems in interesting, predictable and controllable ways. We see first in weakly interacting systems that the magnetic dipole interactions altered the distribution of atoms in the collection. This atom distribution narrows, suppressing very short and large separations. This change in the atom separations reduces the available eigenmodes in the system, especially those with larger collective resonances. Consequently, other modes in the system become much more common as the atomic realisations become more similar to each other. This enhanced the optical response at low density, where only one mode was generally occupied. This mode became easier to excite because other modes near it were removed from the system with increased interaction strength, leaving only more similar modes behind. This increased excitation of modes could be seen in the enhancement of coherent and incoherent scattering with increasing interaction strength at low density. The linewidth of the optical response also generally decreased with increased interactions for the same reason.

At high density, collective eigenmodes begin to resolve themselves in frequency space, which can initially make it appear the optical response is being diminished. Instead, what is happening is the separate eigenmodes are most excited at separated frequencies rather than at the same frequency. Therefore, their individual response is no longer overlapped. As the interaction strength increases, it still becomes easier to excite different eigenmodes of the system, with

some becoming more prominent only at high density and high interaction strength. The change in atom correlations caused by increased interactions also allows eigenmodes with polarisations parallel to the beam polarisation (or out-of-plane) to be excited. This was seen when the incoherent and coherent scattering were compared to each other. The incoherent scattering is generally much more broadly scattered and, as such, requires a larger lens to collect it. This larger lens detected scattering not seen by a smaller lens, indicating some atoms were polarised such that they were scattering light away from the optical axis. We then saw that, indeed, there was significant out-of-plane polarisation (in the 2D case). This polarisation was most pronounced at a detuning away from where the coherent scattering was maximum, also indicating these polarisations were due to different eigenmodes being excited.

We also found that introducing magnetic interactions would produce local Zeeman splitting of the atoms. This had two effects on the optical response. Firstly, the line shape broadens since the optical transitions also broaden. Secondly, there is a shift of the peak resonance for two reasons. Firstly, due to the expected separation of atomic nearest neighbours in the sample, there is an expected Zeeman shift of the atoms. Secondly, there is a second smaller shift due to an atom's minimum expected level shift due to longer-range interactions.

5.2 Strong interactions

With stronger interactions, the systems of dipoles spontaneously crystallise into semi-regular structures. This changes the distribution of atomic separations so that most atoms have the same separation from their nearest neighbour. With this change, the available eigenmodes of the systems become differentiated and easily identifiable. We found that different eigenmodes could be selectively excited by carefully selecting the incident beam orientation and polarisation. In particular, it was possible in the 2D case to select between in-plane and out-of-plane modes. We were also able to excite super- or subradiant modes selectively.

In most cases, the excitation of superradiant modes is easier, with little need to match the detuning to the collective resonance. The subradiant modes are much harder to excite, needing a beam detuning that precisely matches the collective resonance. However, once these modes are excited, they are excited at the exclusion of most other nearby modes in the system. The

form of the eigenmodes in the 2D crystallised systems has a complex structure with many modes that seem related to others in their character.

5.3 Further work

In this work, relatively small collections of atoms were studied, ranging from $N = 10$ to $N = 200$, due to the difficulty of simulating them, especially in the crystallised regime. In future work, it would be interesting to look at simulating much larger numbers of atoms in both the non-crystallised and crystallised regimes. Larger amounts of atoms may allow for the excitation of more complex and interesting eigenmodes than we have seen in the 50-atom cases here. It would also be good to compare the optical response of these crystallised structures to regular arrays, particularly triangular arrays, to match the hexagonal structure of the crystals. Finally, the range of eigenmodes found in strongly interacting systems could be better excited with beams of light with more complex profiles and polarisations that better match the polarisations of particular eigenmodes.

A Parameter relations for Dysprosium

The interaction length R_{dip} [Eq. (37)] for dysprosium is $21\,\mathrm{nm}$. If looking at the $626\,\mathrm{nm}$ transition of Dysprosium [48, 49, 69], for example, then the length scale $1/k$ is approximately $100\,\mathrm{nm}$. Trapping lengths and other length scales quoted in terms of k are convertible by taking the quoted value $\times 100\,\mathrm{nm}$. For example, the trapping lengths ℓ_z in the Fig. (16) are $\approx 0.15 \times 100\,\mathrm{nm} = 15\,\mathrm{nm}$. The 2D density, $\bar{\rho}_{2\mathrm{D}}/k^2$ is convertible to more standard units by taking the value quoted and multiplying by $10^{10}\,\mathrm{cm}^{-2}$. For example, the low density case $0.1k^2 = 0.1 \times 10^{10}\,\mathrm{cm}^{-2} = 1 \times 10^{9}\,\mathrm{cm}^{-2}$.

B Paraxial Gaussian beam

The incident beam used is assumed to be Gaussian and paraxial. The beam will be assumed to have a propagation direction along the z-axis. [51, 70, 71]

$$\boldsymbol{\mathcal{E}}_0^+(\varrho, z) = \mathcal{E}_0 \frac{W_0}{W(z)} \exp\left(\frac{-\varrho^2}{W(z)^2} + i\left(kz - \phi_g + \frac{k\varrho^2}{2R(z)}\right)\right)\hat{\mathbf{e}} \tag{77}$$

$$\phi_g(z) = \tan^{-1}\left(\frac{z}{z_R}\right), \quad W(z) = W_0\sqrt{1 + \left(\frac{z}{z_R}\right)^2} \tag{78}$$

$$R(z) = z\left[1 + \left(\frac{z_R}{z}\right)^2\right], \quad z_R = \frac{W_0^2}{2k} \tag{79}$$

W_0 is the beam waist at the narrowest point, $\hat{\mathbf{e}}$ is the beam polarisation. $W(z)$ is the beam waist at z, $R(z)$ is the wavefront curvature at z and ϱ is the 2D radius as in Eq. (47). The total intensity of the incident beam collected over a lens with area A at distance z along the optical axis away is

$$\int\int \langle \boldsymbol{\mathcal{E}}_0^- \cdot \boldsymbol{\mathcal{E}}_0^+ \rangle \, dA = (W_0^2\pi^2)\left(1 - \exp\left(-\frac{2R(z)}{W(z)^2}\right)\right). \tag{80}$$

C Beam matching

In Fig. (58) the change in the density profile with interaction length is shown for 100 interacting atoms in a pancake-shaped trap. The blue dotted curve shows the density profile of the sample. As the interaction strength increases, the shape of the sample deviates from a Gaussian,

becoming more flat and broad near the top and steeper at the sides.

This leads to a second issue because the sample is illuminated by a Gaussian beam, which has a width chosen to match the width of the sample. In the non-interacting case, it is easy to choose the beam's width to match the trap's width since the density profile will also be Gaussian. However, now that the density profile is no longer Gaussian, we cannot simply choose the beam width to match the trap width. Instead, we can choose the beam width to match the HWHM of the sample. To calculate the HWHM of the sample, I fit the density of the sample to the modified 'flattened' Gaussian function.

$$f(r) = A \exp\left(-\left(\frac{r}{a}\right)^2 - \left(\frac{r}{b}\right)^4\right) \tag{81}$$

as in [72], where A, a and b are free parameters which are fitted to the density data (although the coefficients have been modified from [72] as $a \to 1/a$ etc. to better align with the form used for Gaussian beam profiles). The Gaussian beam profile is then chosen so that the HWHM of the beam matches that of the fitted function.

This method is preferable to finding the HWHM of the density profile directly because the peak density has to be calculated in a small region around the centre, which naturally introduces a larger uncertainty in peak density. Using the fitted function greatly reduces this error in the HWHM value. The peak density of samples can also be calculated similarly by finding the peak of the fitted flat Gaussian.

D Zeeman coupling

Non-dimensionalising Eq. (58) so that the shift is in units of the natural linewidth and the atom separations in units $\mathcal{L}_v$, we find the terms in front of the sum now act like a dimensionless coupling strength

$$C' = g\left(\frac{\mu_B}{\mu}\right)\left(\frac{\omega_i}{\gamma}\right)\left(\frac{\ell_i^2}{\mathcal{L}_v^2}\right)\left(\frac{R_{\text{dip}}}{\mathcal{L}_v}\right) \tag{82}$$

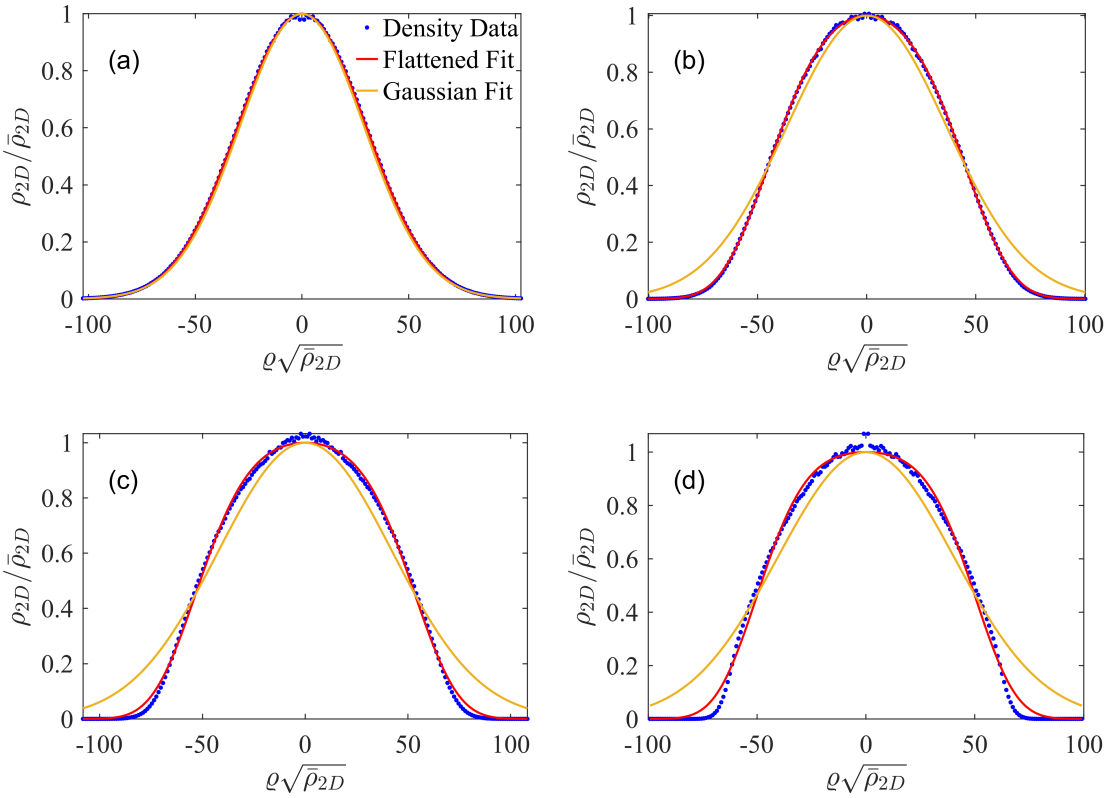

Figure 58: Density profile of a 100 atom system overlapped with a fitted flattened Gaussian distribution Eq. 81 as well as a Gaussian distribution with a width that matches the HWHM of the flattened Gaussian fit. The density shown is the normalised 2D density where $\varrho^2 = x^2 + y^2$. The Gaussian beam is fitted such that it has the same HWHM as the modified Gaussian, which is fitted to the density data. The fit is representative of the incident beam intensity from the Gaussian beam at $z = 0$. The trapping widths respectively are $\ell_x\sqrt{\bar{\rho}_{2D}} = 40.0, 31.0, 16.3, 9.96$ for $R_{\rm dip}\sqrt{\bar{\rho}_{2D}} = 0, 0.002, 0.017, 0.15$ respectively for (a) (b) (c) (d). The choice of width for the Gaussian beam reduces the deviation between the sample profile and the beam intensity profile.

where ℓ_i is an appropriate trap width and $\mathcal{L}_v$ is an appropriate length scale. This could be a length scale based on the sample density,

$$\mathcal{L}_\rho = \frac{1}{\sqrt{\bar{\rho}_{2D}}}, \tag{83}$$

for example, but could also be $1/k$ or another trap length. Writing the coupling strength this way allows it to be modified via various relevant ratios. In the results of 4.3 the specific choice is made that $\mathcal{L}_v = \mathcal{L}_\rho$, $\ell_i = \ell_x$; different choices will give different values for C'.

E Coupling strength for Dysprosium

Defining the dimensionless coupling strength as

$$C' = g\left(\frac{\mu_B}{\mu}\right)\left(\frac{\omega_z}{\gamma}\right)\left(\frac{\ell_z}{R_{\rm dip}}\right)^2 = 1.33 \tag{84}$$

where the value of the dipole moment of Dysprosium is assumed to be $10\mu_B$ then $R_{\rm dip} = 21\ \rm nm$, also using the linewidth of the $626\,\rm nm$ transition, which is 135 kHz we find the value for the coupling strength.

References

[1] J. D. Jackson, *Classical Electrodynamics*, 3rd (Wiley, New York, NY, 1999).

[2] J. Javanainen and J. Ruostekoski, "Light propagation beyond the mean-field theory of standard optics", Opt. Express **24**, 993–1001 (2016).

[3] Y.-X. Huang, M. Li, Z.-J. Chen, Y.-L. Zhang, X.-B. Zou, G.-C. Guo, and C.-L. Zou, "Residual Quantum Effects beyond Mean-Field Treatment in Quantum Optics Systems", Laser & Photonics Reviews **17**, 2200599 (2023).

[4] J. Pellegrino, R. Bourgain, S. Jennewein, Y. Sortais, A. Browaeys, S. Jenkins, and J. Ruostekoski, "Observation of suppression of light scattering induced by dipole-dipole interactions in a cold-atom ensemble", Physical Review Letters **113**, 133602 (2014).

[5] S. D. Jenkins, J. Ruostekoski, J. Javanainen, S. Jennewein, R. Bourgain, J. Pellegrino, Y. R. P. Sortais, and A. Browaeys, "Collective resonance fluorescence in small and dense atom clouds: Comparison between theory and experiment", Physical Review A **94**, 023842 (2016).

[6] J. Ruostekoski and J. Javanainen, "Quantum field theory of cooperative atom response: low light intensity", Phys. Rev. A **55**, 513–526 (1997).

[7] S. Jennewein, M. Besbes, N. Schilder, S. Jenkins, C. Sauvan, J. Ruostekoski, J.-J. Greffet, Y. Sortais, and A. Browaeys, "Coherent scattering of near-resonant light by a dense microscopic cold atomic cloud", Physical Review Letters **116**, 233601 (2016).

[8] J. Javanainen, J. Ruostekoski, Y. Li, and S.-M. Yoo, "Shifts of a resonance line in a dense atomic sample", Phys. Rev. Lett. **112**, 113603 (2014).

[9] R. H. Dicke, "Coherence in spontaneous radiation processes", Physical Review **93**, 99–110 (1954).

[10] A. Svidzinsky and J.-T. Chang, "Cooperative spontaneous emission as a many-body eigenvalue problem", Physical Review A **77**, 043833 (2008).

[11] E. Shahmoon, D. S. Wild, M. D. Lukin, and S. F. Yelin, "Cooperative Resonances in Light Scattering from Two-Dimensional Atomic Arrays", Phys. Rev. Lett. **118**, 113601 (2017).

[12] M. Gross and S. Haroche, "Superradiance: An essay on the theory of collective spontaneous emission", Physics Reports **93**, 301–396 (1982).

[13] G. Facchinetti, S. D. Jenkins, and J. Ruostekoski, "Storing Light with Subradiant Correlations in Arrays of Atoms", Physical Review Letters **117**, 243601 (2016).

[14] K. E. Ballantine and J. Ruostekoski, "Unidirectional absorption, storage, and emission of single photons in a collectively responding bilayer atomic array", Phys. Rev. Res. **4**, 033200 (2022).

[15]N. Fayard, I. Ferrier-Barbut, A. Browaeys, and J.-J. Greffet, "Optical control of collective states in one-dimensional ordered atomic chains beyond the linear regime", Phys. Rev. A **108**, 023116 (2023).

[16]K. E. Ballantine and J. Ruostekoski, "Quantum Single-Photon Control, Storage, and Entanglement Generation with Planar Atomic Arrays", PRX Quantum **2**, 040362 (2021).

[17]S. D. Jenkins and J. Ruostekoski, "Controlled manipulation of light by cooperative response of atoms in an optical lattice", Phys. Rev. A **86**, 031602 (2012).

[18]S. L. Bromley, B. Zhu, M. Bishof, X. Zhang, T. Bothwell, J. Schachenmayer, T. L. Nicholson, R. Kaiser, S. F. Yelin, M. D. Lukin, A. M. Rey, and J. Ye, "Collective atomic scattering and motional effects in a dense coherent medium", Nature Communications **7**, 11039 (2016).

[19]S. D. Jenkins, J. Ruostekoski, J. Javanainen, R. Bourgain, S. Jennewein, Y. R. P. Sortais, and A. Browaeys, "Optical resonance shifts in the fluorescence of thermal and cold atomic gases", Phys. Rev. Lett. **116**, 183601 (2016).

[20]G. J. Bean, N. D. Drummond, and J. Ruostekoski, "Propagation of light in cold emitter ensembles with quantum position correlations due to static long-range dipolar interactions", Phys. Rev. Res. **6**, 013078 (2024).

[21]N. S. Bassler, I. Varma, M. Proske, P. Windpassinger, K. P. Schmidt, and C. Genes, "Cooperative effects in dense cold atomic gases including magnetic dipole interactions", ArXiv e-prints, arXiv:2306.11486 [cond-mat.quant-gas] (2023).

[22]A. Griesmaier, J. Werner, S. Hensler, J. Stuhler, and T. Pfau, "Bose-einstein condensation of chromium", Phys. Rev. Lett. **94**, 160401 (2005).

[23]A. Griesmaier, J. Stuhler, and T. Pfau, "Production of a chromium bose–einstein condensate", Applied Physics B **82**, 211–216 (2005).

[24]M. Lu, N. Q. Burdick, S. H. Youn, and B. L. Lev, "Strongly Dipolar Bose-Einstein Condensate of Dysprosium", Phys. Rev. Lett. **107**, 190401 (2011).

[25]E. Lucioni, L. Tanzi, A. Fregosi, J. Catani, S. Gozzini, M. Inguscio, A. Fioretti, C. Gabbanini, and G. Modugno, "Dysprosium dipolar Bose-Einstein condensate with broad Feshbach resonances", Phys. Rev. A **97**, 060701 (2018).

[26]K. Aikawa, A. Frisch, M. Mark, S. Baier, A. Rietzler, R. Grimm, and F. Ferlaino, "Bose-einstein condensation of erbium", Phys. Rev. Lett. **108**, 210401 (2012).

[27]J. Ulitzsch, D. Babik, R. Roell, and M. Weitz, "Bose-Einstein condensation of erbium atoms in a quasielectrostatic optical dipole trap", Phys. Rev. A **95**, 043614 (2017).

[28]R. Song, S.-H. Zhang, W.-M. Liao, J. Wang, S.-J. Deng, and H.-B. Wu, "Dipolar Bose–Einstein condensation of ^{168}Er and anisotropic expansion dynamics", Results in Physics **52**, 106795 (2023).

[29]H. Li, J. F. Wyart, O. Dulieu, S. Nascimbene, and M. Lepers, "Optical trapping of ultracold dysprosium atoms: Transition probabilities, dynamic dipole polarizabilities and van der Waals c_6 coefficients", J. Phys. B: At. Mol. Opt. Phys. **50**, 014005 (2017).

[30]S. H. Youn, M. Lu, U. Ray, and B. L. Lev, "Dysprosium magneto-optical traps", Phys. Rev. A **82**, 043425 (2010).

[31]G. Nave and U. Griesmann, "New Energy Levels and Classifications of Spectral Lines from Neutral and Singly-Ionized Dysprosium (Dy I and Dy II)", Physica Scripta **62**, 463 (2000).

[32]W. Guerin, M. O. Araújo, and R. Kaiser, "Subradiance in a large cloud of cold atoms", Physical Review Letters **116**, 463 (2016).

[33]A. Frisch, M. Mark, K. Aikawa, S. Baier, R. Grimm, A. Petrov, S. Kotochigova, G. Quéméner, M. Lepers, O. Dulieu, and F. Ferlaino, "Ultracold Dipolar Molecules Composed of Strongly Magnetic Atoms", Phys. Rev. Lett. **115**, 203201 (2015).

[34]J. P. Shaffer, S. T. Rittenhouse, and H. R. Sadeghpour, "Ultracold Rydberg molecules", Nature Communications **9**, 1965 (2018).

[35]L. De Marco, G. Valtolina, K. Matsuda, W. G. Tobias, J. P. Covey, and J. Ye, "A degenerate Fermi gas of polar molecules", Science **363**, 853–856 (2019).

[36]G. Valtolina, K. Matsuda, W. G. Tobias, J.-R. Li, L. De Marco, and J. Ye, "Dipolar evaporation of reactive molecules to below the Fermi temperature", Nature **588**, 239–243 (2020).

[37]F. Böttcher, J.-N. Schmidt, M. Wenzel, J. Hertkorn, M. Guo, T. Langen, and T. Pfau, "Transient Supersolid Properties in an Array of Dipolar Quantum Droplets", Physical Review X **9**, 011051 (2019).

[38]R. N. Bisset and P. B. Blakie, "Crystallization of a dilute atomic dipolar condensate", Phys. Rev. A **92**, 061603 (2015).

[39]L. Tanzi, J. G. Maloberti, G. Biagioni, A. Fioretti, C. Gabbanini, and G. Modugno, "Evidence of superfluidity in a dipolar supersolid from nonclassical rotational inertia", Science **371**, 1162–1165 (2021).

[40]D. Baillie, R. M. Wilson, R. N. Bisset, and P. B. Blakie, "Self-bound dipolar droplet: A localized matter wave in free space", Phys. Rev. A **94**, 021602 (2016).

[41]M. Schmitt, M. Wenzel, F. Böttcher, I. Ferrier-Barbut, and T. Pfau, "Self-bound droplets of a dilute magnetic quantum liquid", Nature **539**, 259–262 (2016).

[42]F. Cinti, P. Jain, M. Boninsegni, A. Micheli, P. Zoller, and G. Pupillo, "Supersolid droplet crystal in a dipole-blockaded gas", Phys. Rev. Lett. **105**, 135301 (2010).

[43]M. A. Norcia, C. Politi, L. Klaus, E. Poli, M. Sohmen, M. J. Mark, R. N. Bisset, L. Santos, and F. Ferlaino, "Two-dimensional supersolidity in a dipolar quantum gas", Nature **596**, 357–361 (2021).

[44]L. Tanzi, E. Lucioni, F. Famà, J. Catani, A. Fioretti, C. Gabbanini, R. N. Bisset, L. Santos, and G. Modugno, "Observation of a Dipolar Quantum Gas with Metastable Supersolid Properties", Phys. Rev. Lett. **122**, 130405 (2019).

[45]F. Böttcher, M. Wenzel, J. Schmidt, M. Guo, T. Langen, I. Ferrier-Barbut, T. Pfau, R. Bombín, J. Sánchez-Baena, J. Boronat, and F. Mazzanti, "Dilute dipolar quantum droplets beyond the extended Gross-Pitaevskii equation", Physical Review Research **1**, 033088 (2019).

[46]G. Pupillo, A. Micheli, M. Boninsegni, I. Lesanovsky, and P. Zoller, "Strongly Correlated Gases of Rydberg-Dressed Atoms: Quantum and Classical Dynamics", Phys. Rev. Lett. **104**, 223002 (2010).

[47]J. C. Smith, D. Baillie, and P. B. Blakie, "Supersolidity and crystallization of a dipolar bose gas in an infinite tube", Phys. Rev. A **107**, 033301 (2023).

[48]S. Jin, J. Gao, K. Chandrashekara, C. Gölzhäuser, J. Schöner, and L. Chomaz, "Two-dimensional magneto-optical trap of dysprosium atoms as a compact source for efficient loading of a narrow-line three-dimensional magneto-optical trap", Phys. Rev. A **108**, 023719 (2023).

[49]T. Maier, H. Kadau, M. Schmitt, A. Griesmaier, and T. Pfau, "Narrow-line magneto-optical trap for dysprosium atoms", Opt. Lett. **39**, 3138–3141 (2014).

[50]M. Lu, S. H. Youn, and B. L. Lev, "Trapping ultracold dysprosium: a highly magnetic gas for dipolar physics", Phys. Rev. Lett. **104**, 063001 (2010).

[51]R. J. Bettles, M. D. Lee, S. A. Gardiner, and J. Ruostekoski, "Quantum and nonlinear effects in light transmitted through planar atomic arrays", Communications Physics **3**, 141 (2020).

[52]S. D. Jenkins and J. Ruostekoski, "Theoretical formalism for collective electromagnetic response of discrete metamaterial systems", Phys. Rev. B **86**, 085116 (2012).

[53]D. A. Steck, *Quantum and Atom Optics*, 0.8.3, 2012, http://steck.us/teaching (2007).

[54]M. D. Lee, S. D. Jenkins, and J. Ruostekoski, "Stochastic methods for light propagation and recurrent scattering in saturated and nonsaturated atomic ensembles", Phys. Rev. A **93**, 063803 (2016).

[55]K. E. Ballantine and J. Ruostekoski, "Subradiance-protected excitation spreading in the generation of collimated photon emission from an atomic array", Physical Review Research **2**, 023086 (2020).

[56]J. Ruostekoski and J. Javanainen, "Arrays of strongly coupled atoms in a one-dimensional waveguide", Physical Review A **96**, 033857 (2017).

[57]J. Ruostekoski, "Cooperative quantum-optical planar arrays of atoms", Phys. Rev. A **108**, 030101 (2023).

[58] J. Ruostekoski and J. Javanainen, "Emergence of correlated optics in one-dimensional waveguides for classical and quantum atomic gases", Phys. Rev. Lett. **117**, 143602 (2016).

[59] J. Javanainen, J. Ruostekoski, Y. Li, and S.-M. Yoo, "Exact electrodynamics versus standard optics for a slab of cold dense gas", Phys. Rev. A **96**, 033835 (2017).

[60] J. Javanainen, J. Ruostekoski, B. Vestergaard, and M. R. Francis, "One-dimensional modeling of light propagation in dense and degenerate samples", Phys. Rev. A **59**, 649–666 (1999).

[61] J Rogel-Salazar, "The Gross–Pitaevskii equation and Bose–Einstein condensates", European Journal of Physics **34**, 247–257 (2013).

[62] C. J. Umrigar, J. Toulouse, C. Filippi, S. Sorella, and R. G. Hennig, "Alleviation of the fermion-sign problem by optimization of many-body wave functions", Phys. Rev. Lett. **98**, 110201 (2007).

[63] T. Pang, *An Introduction to Quantum Monte Carlo Methods* (Morgan and Claypool, 2016).

[64] W. M. C. Foulkes, L. Mitas, R. J. Needs, and G. Rajagopal, "Quantum Monte Carlo simulations of solids", Reviews of Modern Physics **73**, 33–83 (2001).

[65] R. J. Needs, M. D. Towler, N. D. Drummond, P. López Ríos, and J. R. Trail, "Variational and Diffusion Quantum Monte Carlo calculations with the CASINO code", The Journal of Chemical Physics **152**, 154106 (2020).

[66] N. D. Drummond, M. D. Towler, and R. J. Needs, "Jastrow correlation factor for atoms, molecules, and solids", Phys. Rev. B **70**, 235119 (2004).

[67] E. Collett, *Field Guide to Polarized Light* (SPIE, 2005), 7–14.

[68] C. D. Parmee, M. R. Dennis, and J. Ruostekoski, "Optical excitations of skyrmions, knotted solitons, and defects in atoms", Communications Physics **5**, 54 (2022).

[69] D. Bloch, B. Hofer, S. R. Cohen, A. Browaeys, and I. Ferrier-Barbut, "Trapping and imaging single dysprosium atoms in optical tweezer arrays", Phys. Rev. Lett. **131**, 203401 (2023).

[70] O. Svelto, *Principles of lasers* (Springer US, Boston, MA, 1998), pp. 129–160.

[71] A. Yariv and P. Yeh, *Optical Waves in Crystals: Propagation and Control of Laser Radiation*, Wiley Classics Library Ed. (Wiley-Interscience, Hoboken, NJ, 2003).

[72] J. Blázquez, A García-Berrocal, C. Montalvo, and M Balbás, "The coverage factor in a Flat-ten–Gaussian distribution", Metrologia **45**, 503 (2008).

[73] D. Ennis, *Quiver3d*, (June 23, 2023) https://www.mathworks.com/matlabcentral/fileexchange/6066-quiver3d.